Eddy Viscosity Turbulence Models for Compressible Mixing

Adrian N. Mihaiescu

A thesis submited for the degree of Ph.D.

Department of Fluid Mechanics and Computational Science

School of Engineering

Cranfield University

Cranfield, UK

Abstract

The $K - L$ and $K - \epsilon$ turbulence models are used to simulate the turbulent mixing induced by the Rayleigh-Taylor and Richtmyer-Meshkov instabilities. The models contain additional source terms for the turbulence kinetic energy which depend on the type of the instability. A new criterion based on ratio of the averaged flow and turbulence time scales is introduced for differentiating between the two types of instabilities. The original formulation of the turbulence kinetic energy source present in the $K - \epsilon$ model is modified in order to accurately capture the evolution of the Richtmyer-Meshkov instability in both heavy/light and light/heavy configurations. Additional constraints are imposed to the models in order to prevent non-physical solutions when strong gradients are present in the flow.

Three test problems are considered and the performance of the turbulence models is assessed by comparing their solutions with the results obtained by high resolution Implicit Large Eddy Simulations (ILES). First, the classical Rayleigh-Taylor and Richtmyer-Meshkov problems are solved. A new approach for initializing the turbulence models in proposed for the Rayleigh-Taylor problem. It is found that both turbulence models describe successfully the self similar growth of the Rayleigh-Taylor and Richtmyer-Meshkov instabilities and can predict accurately the spatial distribution of the fluid concentrations and of the turbulent kinetic energy. The last problem involves the mixing induced at two planar interfaces by multiple shock reflections and refractions. The turbulence models estimate correctly the evolution of the mixing and of the total kinetic energy in the mixing zones.

The transport equations of the turbulence models are solved numerically and the influence of the numerical schemes on the results is investigated. It is concluded that the numerical schemes do not have an important influence on the results in the case of the classical Rayleigh-Taylor problem (provided that grid convergence has been achieved and the turbulence models have been initialized using the method proposed here). However, in the presence of shocks (such as in the case of the Richtmyer-Meshkov instability), the HLLC Riemann solver should be used together with a reconstruction scheme of third or higher order of accuracy.

Acknowledgements

First I would like to express my gratitude to Prof. Dimitris Drikakis for his guidance and support during the years of research for my PhD degree.
Special thanks to David L. Youngs and Robin J.R. Williams at AWE for their very useful comments and advices regarding the physics of turbulent mixing, and also for the numerical data they have provided.
I would like also to thank Drs. Ben Thornber, Evgeniy Shapiro and Marco Hahn for their help and useful dicussions.

Adrian N. Mihaiescu

Contents

List of Figures

List of Tables

Nomenclature

Latin Symbols

a	the speed of sound
A_0	initial Atwood number
A_L	local Atwood number
A_SS	self similar Atwood number
$\mathbf{A} = (A_x, A_y, A_z)$	Jacobian of the Euler equations in conservative formulation
$\mathcal{A}$	area
$\mathbf{B} = (B_x, B_y, B_z)$	Jacobian of the Euler equations in primitive variable formulation
c	molar concentration
c_p	specific heat at constant pressure
c_v	specific heat at constant volume
C_A	local Atwood number coefficient
C_B	buoyancy number coefficient
C_C	compression number coefficient
C_L	eddy size production coefficient
C_P	turbulence pressure coefficient
C_μ	eddy viscosity coefficient
C_S	constant in Sutherland's formula for viscosity

d_{s}	standard deviation of the initial interface perturbation
D_e	diffusion coefficient for the internal energy
D_F	diffusion coefficient for the mass fraction
D_K	diffusion coefficient for the turbulence kinetic energy
D_L	diffusion coefficient for the eddy the size
D_ϵ	diffusion coefficient for the dissipation rate
e	internal energy per unit mass
E	total energy per unit mass
$\mathcal{E}_{\mathrm{k}}$	total kinetic energy of the mean flow in a control volume
$\mathcal{E}_{\mathrm{p}}$	total potential energy of the mean flow in a control volume
f	volume fraction
F	mass fraction
$\mathbf{g} = (g_x, g_y, g_z)$	external force per unit mass (gravity)
h	internal enthalpy per unit mass
H	total enthalpy per unit mass
J_{e}	diffusive energy flux in multicomponent flows
J_{h}	diffusive enthalpy flux in multicomponent flows
J_{m}	diffusive mass flux in multicomponent flows
k_{c}	thermal conductivity
K	turbulence kinetic energy
$\mathcal{K}$	total kinetic energy
$l(r)$	limiter function for MUSCL schemes
L	eddy size (turbulence length scale)
$\mathcal{L}$	length
$\mathcal{L}_x, \mathcal{L}_y, \mathcal{L}_z$	dimensions of the computational domain
M	molecular mass
$\mathcal{M}$	total mixing
N_{Spec}	number of species
N_{FV}	number of finite volumes
N_{S}	number of faces of a finite volume
p	pressure
P	eigenvectors of the Euler equation in conservative formulation

Q	eigenvectors of the Euler equation in primitive variable formulation
$\mathbf{q} = (q_x, q_y, q_z)$	diffusive heat flux
R	specific gas constant
$\mathcal{R}$	universal gas constant
$\overline{\overline{S}}$	rate of deformation tensor
t	time
T	temperature
$\mathbf{u} = (u, v, w)$	Cartesian components of the velocity (mass-weighted for multicomponent flows)
u_{t}	turbulence velocity
U	conservative variables
V	primitive variables
$\hat{V}$	characteristic variables
$\mathcal{V}$	volume
W	mechanical work per unit mass and per unit time
$\mathcal{W}$	integral length of the mixing zone
$\mathbf{x} = (x, y, z)$	Cartesian coordinates
Y	the right-hand side of the transport equations

Greek Symbols

α	parameter characterizing the self similar RTI growth rate
β	parameter in MUSCL schemes
γ	adiabatic exponent of the fluid
δ_{ij}	Kronecker operator
ΔU	velocity change of the interface produced by a shock
ϵ	dissipation rate of the turbulence kinetic energy
η	amplitude of the perturbation
θ	parameter characterizing the self similar RMI growth rate
Θ	time scale of the mean flow
Θ_t	turbulence time scale
κ	wave number of the perturbation
λ	eigenvalue of a matrix; wavelength of the perturbation
Λ_ρ	limiter for the turbulent mass diffusion
$\Lambda_{\text{min}}, \Lambda_{\text{min}}$	limiters for the turbulent stresses
Λ_Θ	limiter for determining the acceleration type
μ	viscosity
μ'	bulk viscosity
μ_t	eddy (turbulent) viscosity
ϖ	deviation of the species from the mass averaged velocity
ρ	density
σ_e	energy diffusion coefficient (constant)
σ_F	mass fraction diffusion coefficient (constant)
σ_K	turbulence kinetic energy diffusion coefficient (constant)
σ_L	eddy size diffusion coefficient (constant)
σ_ϵ	dissipation rate diffusion coefficient (constant)

$\overline{\overline{\tau}}$	viscous stresses
$\overline{\overline{\tau}}_{\mathrm{t}}$	turbulent stresses
$\upsilon = (\upsilon_1, \upsilon_2, \upsilon_3)$	volume-weighted velocity in multicomponent flows
ϕ, ψ	generic quantities
$\Phi = (\Phi_x, \Phi_y, \Phi_z)$	flux vector in the transport (Euler) equations
Φ	forces acting between species in multicomponent flows
Ψ	energy transfer between species in multicomponent flows
$\Psi(\psi_1, \psi_2)$	function characterizing the RMI nonlinear growth rate at late times
χ	molar fraction

Acronyms

CFD	Computational Fluid Dynamics
ILES	Implicit Large Eddy Simulations
ILMZ	Integral Length of the Mixing Zone
MUSCL	Monotonic Up-wind Schemes for Conservation Laws
MinMod	Minimum Module
RM (I)	Richtmyer-Meshkov (Instability)
RT (I)	Rayleigh-Taylor (Instability)
TKE	Turbulent Kinetic Energy
TVD	Total Variation Diminishing
WENO	Weighted Essentially Non-Oscillatory

Chapter 1

Introduction

The turbulent mixing of different fluids is of great importance in fluid mechanics as it occurs in a wide range of natural processes and engineering applications. Turbulence is still a poorly understood phenomenon and there is no complete theoretical model based on the fundamental laws of classical mechanics that could fully describe the turbulent flows. Therefore, the prediction of turbulent mixing is based on semi-empirical models, based on experimental and numerical data.

Considering the case of different fluids initially separated by an interface of some arbitrary shape, there are three fundamental mechanisms associated with the amplification of the geometrical perturbations of the interface and the initiation of the mixing process: the Kelvin-Helmholtz (KM), Rayleigh-Taylor (RT) and Richtmyer-Meshkov (RM) instabilities. The first instability is related to the difference between the tangential components of the velocities of the fluids at the interface. The last two instabilities are related to the acceleration of the fluids against each other on the direction perpendicular to the interface. The acceleration is usually gravitational in the case of the Rayleigh-Taylor instability (depicted in Figure 1.1) and it is the result of a shock wave passing through the interface in the case of the Richtmyer-Meshkov instability (as shown in Figure 1.2). The presence of these instabilities is responsible for the enhancement of the mixing processes in various type of compressible multi-component flows, at a large range of length and time scales. Their accurate simulation is important for many theoretical and practical

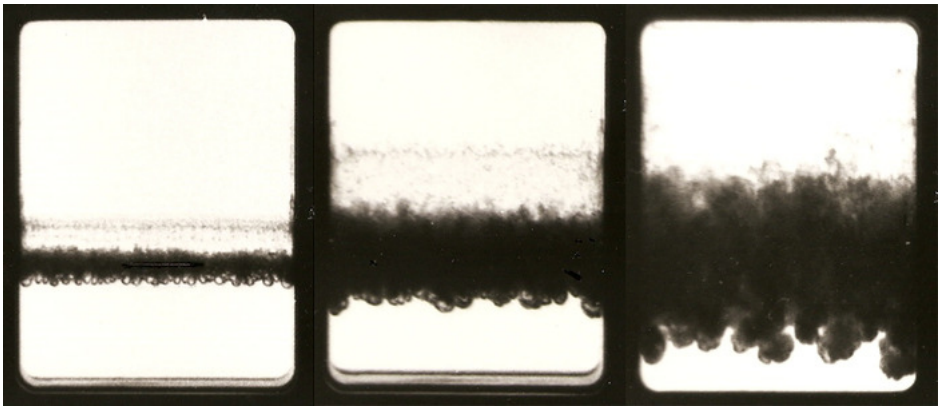

Figure 1.1: The development of the Rayleigh-Taylor instability - experimental study of Youngs (1989).

applications, such as the study of supernovae explosions Arnett (2000), Almgren et al. (2000)), ICF implosions (Lindl et al. (1992), Holmes et al. (1999), Amendt et al. (2002)) or supersonic combustions (Yang et al. (1993)).

In general, both RM and RT instabilities have initially a linear growth regime, but they can become non-linear later. In the non-linear regime the flow becomes turbulent and self-similar to the turbulent eddy size. There are two main types of methods for simulating the RM and RT instabilities: models based on the description of the self-similar evolution of the instability, and numerical simulations based on transport equations derived from the Navier-Stokes or Euler models. The former methods are usually limited to one-dimensional problems and cannot offer informations regarding the flow field, such as the density or the concentration of the fluids. The later methods can be used for simulating two- and three-dimensional flows and they usually require turbulence models for high Reynolds numbers, especially when other associated physical and chemical processes are considered. There are two main approaches for turbulence modelling. The most complex are the multi-fluid models, where each fluid has its own fluctuation velocity and its distribution in space is characterized by the mass or volume fraction. The second approach is based on a single fluctuation velocity, and individual mass or volume fractions. They are simpler and more stable the the former models but they can-

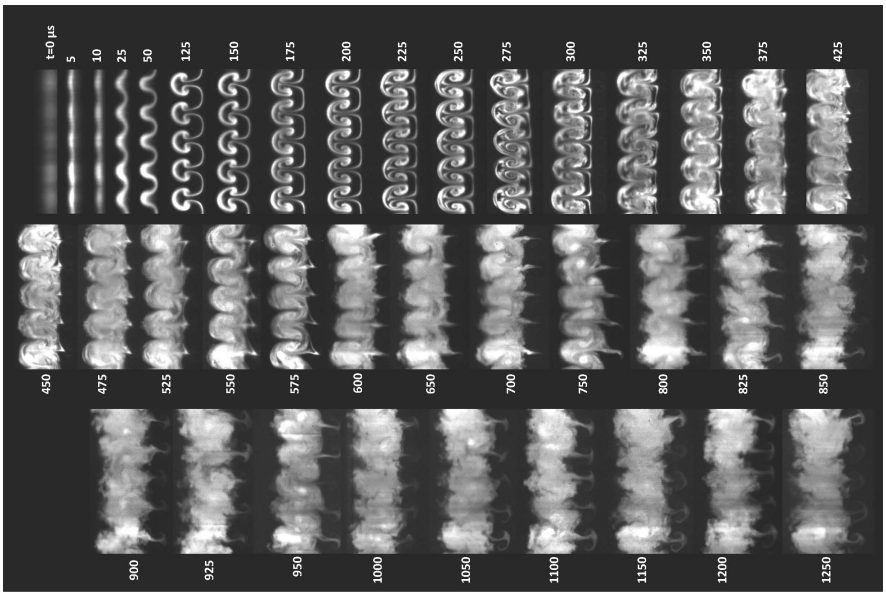

Figure 1.2: The development of the Richtmyer-Meshkov instability in a shock tube experiment conducted at the Los Alamos National Laboratory by Orlicz (2012).

not simulate the de-mixing. A major difficulty arising when the turbulence models are used for simulating the Rayleigh-Taylor and Richtmyer-Meshkov instabilities comes from the unsteadiness of the averaged flow which causes the dependency of the solution on the initial conditions applied to the turbulence quantities. A second problem is related to the presence of shocks in the case of the RM problems. Careful considerations must be taken for the the numerical treatment of the discontinuities. Diffusive numerical methods can underestimate the turbulence enhancement while very strong numerical gradients can produce non-physical results.

The aim of the present work is to implement the turbulence models of Dimonte and Tipton (2006) and Gauthier and Bonnet (2000) and to investigate their capability of accurately predicting the turbulent compressible mixing by the RT and RM instabilities. The turbulence kinetic source present in the original $K-\epsilon$ models have been modified in order to be dependent on the type of instability. A new criterion based on the time scales of the mean flow and of the turbulence fluctuations is introduced and applied for both turbulence models in order to determine the type of instability. The turbulence models are initialized using a new procedure based

on the prediction of the mixing zone extent and of the turbulence kinetic energy at early times. The width of the mixing zone, the distribution and the magnitude of the turbulence kinetic energy at early times are assessed using theoretical models and experimental results. The two models are applied to the classical Rayleigh-Taylor and Richtmyer-Meshkov problems, but also to a more complex test case featuring multiple shock reflections from one solid walls and two interfaces. For all test problems it is assumed that the physical viscosity of the fluids is much smaller than the turbulent viscosity. Therefore the Reynolds stresses are much higher than the viscous stresses and the latter can be neglected.

The structure of the thesis is as follows. The ending sections of this chapter describe the mechanisms of the Rayleigh-Taylor and Richtmyer-Meshkov instabilities and presents the main theoretical, experimental and numerical results regarding the mixing by RTI and RMI.

The second chapter is dedicated to the main models in fluid mechanics. The first sections present the classical Navier-Stokes and Euler models for compressible flows, and the thermodynamic equations for perfect gases. In the section 2.5 the conservation principles are applied to the multicomponent flows and the transport equations are derived for the species and for the mixture. The basics of turbulence modelling of compressible flows are discussed in section 2.6. The two turbulence models investigated in the present work are described in the last sections of the chapter.

The numerical methods used for solving the transport equations of the turbulence model are presented in 3. The focus is the numerical schemes used for solving the transport equations for compressible flows.

The performance of the two turbulence models is investigated in Chapter 4. Three test problems are considered and the performance of the turbulence models is assessed by comparing their solutions with the results obtained by high resolution Implicit Large Eddy Simulations (ILES). The transport equations of the turbulence models are solved numerically and the influence of the numerical schemes on the results is discussed.

A summary of the results of the present work is presented in the last chapter,

together with some recommendations regarding the future work.

1.1 The Rayleigh-Taylor instability

The basic configuration of the Rayleigh-Taylor instability is presented in Figure 1.3. Two fluids of different densities ρ_1, ρ_2 are separated by a planar interface and accelerated against each other by the gravity acting perpendicular to the interface. The amplitude of the initial interface perturbation varies in one direction if the geometrical configuration is two-dimensional and in two orthogonal directions in the case of a three-dimensional configuration. The initial perturbation amplitude can have the shape of a sine function of one single wavelength and amplitude (single mode perturbation) or can be a superposition of a multitude of single mode perturbations of different amplitudes and wavelengths (multi mode perturbation). Figure 1.3 depicts the case of a two-dimensional, single-mode perturbation. The initial interface perturbation grows in time and the heavy fluid penetrates into the lighter fluid as bubbles. At early times, when the amplitude of the perturbation η is smaller than the wave length of the perturbation λ, the linear stability theory can be applied for estimating the growth rate of the perturbation, as shown in Section 1.1.1. As the amplitude grows, the instability becomes non-linear and asymmetric (i.e. the amplitude of the spikes η_S is larger than the amplitude of the bubbles η_B), as shown in Section 1.1.2.

1.1.1 Linear theory

Considering the initial densities of the two fluids ρ_1 and ρ_2, the inviscid linear stability analysis gives the growth in time of an initial perturbation of wave number k and initial amplitude η_0 (Rayleigh (1883), Taylor (1950)):

$$\eta(t) = \eta_0 \, exp\,(nt) \tag{1.1}$$

with:

$$n^2 = \kappa A_0 g \tag{1.2}$$

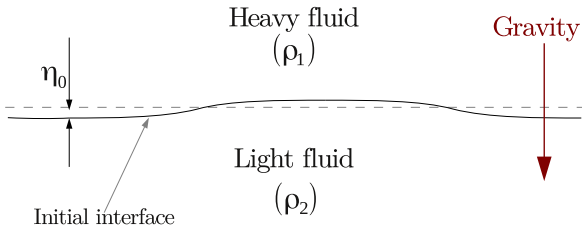

(a)

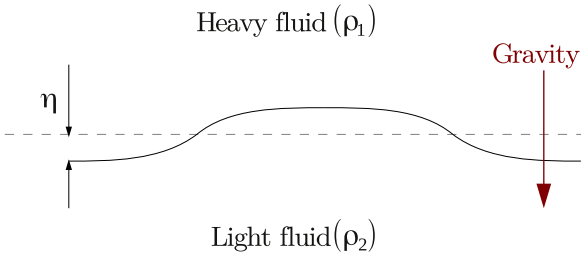

(b)

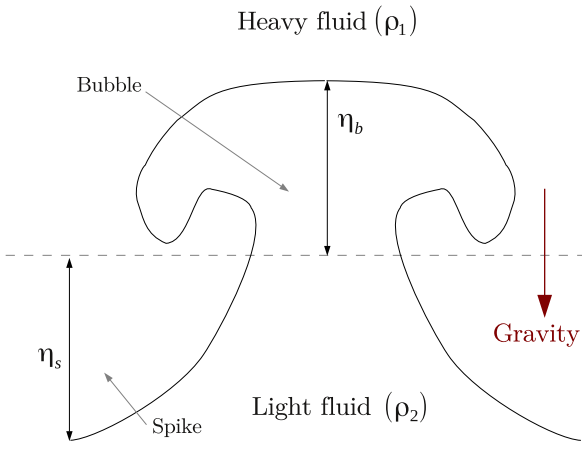

(c)

Figure 1.3: Schematic of the Rayleigh-Taylor instability: (a) initial configuration; (b) linear regime; (c) non-linear regime.

where g is the acceleration acting from fluid 1 towards fluid 2 and $A_0 = (\rho_1 - \rho_2)/(\rho_1 + \rho_2)$ is the initial Atwood number. The configuration is unstable if $A_0 g > 0$, i.e. the heavy fluid is accelerated against the lighter fluid. The linear theory is valid at the early stages of the instability evolution, while the perturbation amplitude is relatively small ($\eta < \lambda = 2\pi/\kappa$).

1.1.2 Non-linear regime

The non-linear regime occurs at later time, as the the perturbation grows and the flow becomes turbulent and self-similar. In this case the growth rate is found to be (Fermi and von Neumann (1953)):

$$\frac{\partial \eta}{\partial t} = 2\sqrt{(\alpha A_0 g \eta)} \tag{1.3}$$

where α is a constant parameter. Considering the initial time ($t = 0$) the moment when the flow becomes self-similar and η_0 the perturbation amplitude at that moment, equation 1.4 gives by integration:

$$\eta(t) = \alpha A_0 g t^2 + 2\sqrt{\alpha A_0 g \eta_0} t + \eta_0 \tag{1.4}$$

The first term in equation 1.4 is dominant at very late times and the perturbation amplitude grows as:

$$\eta(t) \simeq \alpha A_0 g t^2 \tag{1.5}$$

The experimental and numerical results (Read (1984), Youngs (1989), Youngs (1994), Dimonte and Schneider (1996)) suggest that the growth rate of the bubbles is given by $\alpha_{\mathrm{B}} = 0.05 \pm 0.02$. The growth rate of the spikes is found at low Atwood numbers:

$$\alpha_{\mathrm{S}} \simeq \alpha_{\mathrm{B}} \left(\frac{\rho_2}{\rho_1}\right)^{1/3} \tag{1.6}$$

and $\alpha_{\mathrm{S}} \simeq 1/2$ as the initial Atwood number tends to 1 (Dimonte and Schneider (2000)).

From energetic point of view, it is found experimentally (Youngs (1994), Ramaprabhu

and Andrews (2004)) and numerically that half of the potential energy released during the RT mixing process is transformed into turbulence kinetic energy, and half is dissipated.

1.2 The Richtmyer-Meshkov instability

The Richtmyer-Meshkov instability occurs when the interface of two fluids is impulsively accelerated by a shock wave. A schematic of the classical RMI problem is presented in Figure 1.4. The planar interface separating two different fluids is impulsively accelerated by a planar shock wave propagating into the first fluid on a direction perpendicular to the interface. After the interaction shock-interface, a refracted shock is transmitted into the second fluid and a shock or an expansion wave is reflected back into the first fluid. As in the case of the RTI problem, the initial interface perturbations can be two or three-dimensional, single or multi-mode, as explained in the previous section. The perturbations of the interface are amplified by the shock wave, and the fluid of higher density penetrates in the fluid of low density as spikes, while the light fluid penetrates the heavy fluid as bubbles. The instability mechanism is based on the misalignment of the pressure gradient caused by the shock and the density gradient at the perturbed interface. The development of the instability changes from an early linear regime, when the amplitude of the perturbation is small, to a non-linear regime, when the amplitude of the perturbation is comparable to the dominant wavelength. The first rigorous investigations of this problem was conducted first theoretically by Richtmyer (1960) and then experimentally by Meshkov (1969).

1.2.1 The incompressible linear theory

The theoretical model proposed by Richtmyer (1960) is based on the hypothesis that the flow can be considered incompressible in the vicinity of the interface once the shocks have passed through the interface. As a result, the Taylor linear theory for the growth of single mode perturbations of interfaces between fluids in gravitational field Taylor (1950) is adapted for impulsively accelerated interfaces

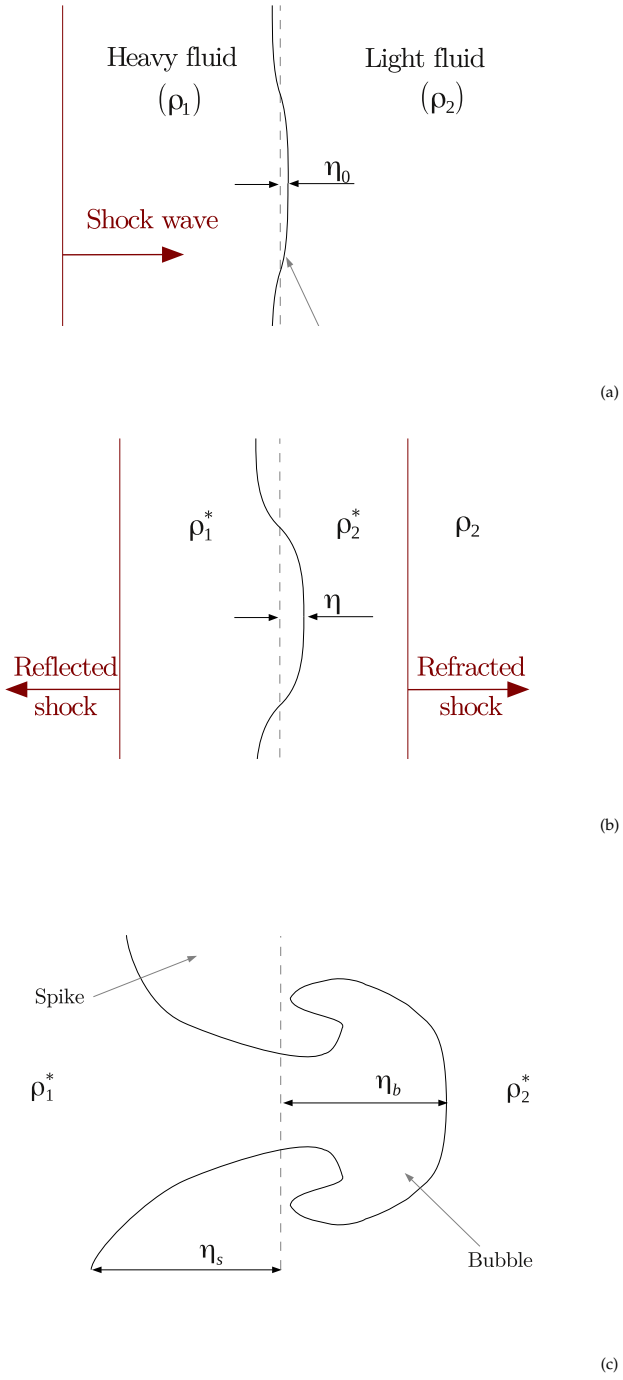

Figure 1.4: Schematic of the Richtmyer-Meshkov instability (heavy/light configuration): (a) initial configuration; (b) linear regime; (c) non-linear regime.

by replacing the constant gravitation acceleration by an impulsive acceleration of the form:

$$g = \triangle U \delta t \tag{1.7}$$

where $\triangle U$ is the change in the interface velocity produced by the shock, δ is the Dirac delta function and t is the time. The resulting model gives a linear expression for the growth of the amplitude η in time:

$$\frac{\partial \eta}{\partial t} = \kappa \triangle U \eta_0 A_0 \tag{1.8}$$

where κ is the wave number of the perturbation, η_0 is the initial amplitude and A_0 is the initial (pre-shock) Atwood number, based on the initial densities of the two fluids ρ_1 and ρ_2 (considering the shock passing from the fluid 1 into the fluid 2):

$$A_0 = \frac{\rho_2 - \rho_1}{\rho_2 + \rho_1} \tag{1.9}$$

The equation 1.8 describes the linear regime of the RM instability and it is valid as long as the amplitude η is much smaller than the wave length of the initial perturbation $\lambda = 2\pi/\kappa$. The growth rate of the perturbation given by the formula 1.8 is constant in time and positive ($\triangle U$ and A_0 have the same sign), resulting that both configurations, heavy/light (as depicted in Figure 1.4) and light/heavy are unstable. The computational study of Richtmyer (1960) showed that good results for the light/heavy configurations are obtained if the post-shock values for the densities (ρ_1^* and ${\rho_2}^*$) and perturbation amplitude (${\eta_0}^*$) are used in the equation 1.8 instead of the pre-shock values:

$$\frac{\partial \eta}{\partial t} = \kappa \triangle U {\eta_0}^* {A_0}^* \tag{1.10}$$

$${A_0}^* = \frac{{\rho_2}^* - {\rho_1}^*}{{\rho_2}^* + {\rho_1}^*} \tag{1.11}$$

The pre- and post-shock interface amplitudes are related by a compression factor Richtmyer (1960):

$$\frac{{\eta_0}^*}{\eta_0} = 1 - \frac{\triangle U}{V_S} \tag{1.12}$$

where V_S is the velocity of the shock.
The numerical results of Meyer and Blewett (1972) showed that while this model gives satisfactory results for positive Atwood numbers, the average of the pre- and post-shock amplitudes should be employed in the formula 1.10 for the heavy/light case:

$$\frac{\partial \eta}{\partial t} = \kappa \triangle U(\eta_0 + {\eta_0}^*){A_0}^* \tag{1.13}$$

A general formula suitable for both cases (heavy/light and light/heavy) was proposed by Vandenboomgaerde et al. (1998), using both pre-shock and post-shock quantities:

$$\frac{\partial \eta}{\partial t} = \kappa \triangle U(\eta_0 A_0 + {\eta_0}^* {A_0}^*)/2 \tag{1.14}$$

While economical from computational point of view, the incompressible impulsive models given by the equations 1.10,1.13 and 1.14 have the disadvantage of describing the evolution of the Richtmyer-Meshkov instability only in the linear regime ($\eta \ll \lambda$) and only in the case of weak shocks, when the compressible effects can be neglected.

1.2.2 The compressible linear theory

The incompressible models presented in the previous section are based on the assumption of an instantaneous acceleration of the interface between fluids of different densities, in the incompressible limit. Even though they have been successfully applied for various test-cases involving shock-interface interaction, it was found that they fail for some configurations Mikaelian (1993). A prominent example is given by some cases involving a light/heavy configuration and a null post-shock Atwood number (${A_0}^* = 0$) when the amplitude of the perturbation η increases in time, contradicting the impulsive model equation 1.10. The transient character of the compressible flows involving shock waves can explain the failure of the impulsive models (Mikaelian (1993), Velikovich (1996)).
The linearised equations describing the perturbation growth caused by a weak shock were derived and solved numerically by Richtmyer (1960). It was found that the growth rate increases asymptotically from zero (at the initial time when

the shock reaches the interface) to a finite positive value at large times. Analytical solutions for the linearised perturbation equations were found first by Fraley (1986) and then Mikaelian (1993) and Yang et al. (1994). The asymptotic linear growth rate of the perturbation found to have the form:

$$\left[\frac{\partial \eta}{\partial t}\right]_{t\to\infty} = \kappa \triangle U \eta_0 \left[A_0 + \epsilon \frac{\Psi(\psi_1, \psi_2)}{\gamma_1}\right] \tag{1.15}$$

where: $\epsilon = p''/(p''-p')$, $\psi_1 = \rho_2/\rho_1$, $\psi_2 = \sqrt{\gamma_2\rho_2/\gamma_1\rho_1}$, γ_2 and γ_2 are the adiabatic exponents of the two fluids, p' and p'' are the pressure values ahead and behind the shock, and the function Ψ is in the case of the analysis of Fraley (1986):

$$\Psi(\psi_1, \psi_2) = \frac{1}{(\psi_1+1)(\psi_2+1)}\left[(\psi_2-1)^2 + 4\frac{{\psi_1}^2 + {\psi_2}^2}{\psi_2(\psi_1+1)} - 2(\psi_1+\psi_2)\right] \tag{1.16}$$

In the case of identical densities ($A_0 = 0$ and $\psi_1 = 1$), the function Ψ is non-zero unless $\psi_2 = 1$ or $\psi_2 = 2$ (the adiabatic exponents ratio is 1 or 4, respectively). As a result, the interaction between a shock and an interface separating two fluids will generally produce a linear growth of the small perturbation even if there is no initial density variation at the interface. This suggests that the instability mechanism of a shocked interface is not caused just by the resulting impulsive acceleration of the interface, but also by the change in the density produced by the transmitted shock. The case $A_0 = 0$ and $\psi_2 = 2$ is one of the so-called "freeze-out" cases, when the growth rate of the perturbation is zero, even if the two fluids have different thermodynamic properties.

1.2.3 Non-linear theory

The incompressible and compressible linear models are valid only at early time, when the perturbation of the interface is relatively small. One family of methods for estimating the instability development at late times are bubble/spike asymptotic evolution models (Alon et al. (1995), Mikaelian (1996), Chen et al. (1996), Ramshaw (1998), Dimonte (2000)), based on potential flow models. They are not valid for the early and intermediate stages of the Richtmyer-Meshkov instability. A com-

pressible non-linear model valid at early and late times was developed by Zhang and Sohn (1996), based on the idea that the RM instability can be treated linearly at early stages (when the compressible effects are dominant), while the non-linear effects are important at intermediate and late times, causing the decay of the perturbation growth rate. The potential model is used for inviscid, incompressible and irrotational flows and the flow quantities are expanded as Taylors series of the initial amplitude. The Padé approximation is applied to the truncated series. The resulting equations are integrated analytically and the result approximates the perturbation growth rate as a function of the solution of the linear compressible theory $\dot{\eta}_{Lin}$:

$$\frac{\partial \eta}{\partial t} = \frac{\dot{\eta}_{Lin}}{1 + \dot{\eta}_{Lin}\eta_0\kappa^2 t + max\left(0,\ {\eta_0}^2\kappa^2 - {A_0}^2 + 1/2\right)(\dot{\eta}_{Lin}\kappa)^2 t^2} \tag{1.17}$$

A simplification of this model was proposed by Vandenboomgaerde et al. (1998). In the analytical solution of Zhang and Sohn (1996) only the terms containing the highest power in time are retained, making the model easily extendable to higher order of approximation and to the case of multi-mode perturbations.

1.2.4 The case of re-shocks

Most of the theoretical models for the RM instability under re-shock conditions are based on the impulsive theory. A simple approach proposed by Andronov et al. (1982) is to apply the linear impulsive model (equation 1.10) to each shock-interface interaction, giving the growth rate produced by the nth interaction of the form:

$$\left[\frac{\partial \eta}{\partial t}\right]_n = \kappa \sum\nolimits_{i=0}^{n} \triangle U_i {\eta_{0i}}^* {A_{0i}}^* \tag{1.18}$$

where $\triangle U_i, {\eta_{0i}}^*$ and ${A_{0i}}^*$ are the velocity jump of the interface caused by the ith wave, the perturbation amplitude and the post-shock Atwood number (corresponding to the ith wave), respectively.

A simpler model was proposed by Mikaelian (1989), assuming no dependence on the initial conditions:

$$\frac{\partial \eta}{\partial t} = C\ \triangle U_1 A_1^* \tag{1.19}$$

where $\triangle U_1$ is the change of the interface produced by the re-shock, A_1^* is the post-re-shock Atwood number and $C = 0.28$ is an empirical coefficient based on the experimental results of Read (1984) and Youngs (1984).
Assuming that the reflected wave interacts with the mixing zone during the non-linear regime of the perturbation growth and that is much weaker than the original shock wave, Charakhch'yan (2001) proposed a model based on the impulsive rate of growth $\dot{\eta}_{Imp}$ and the post-shock Atwood number corresponding to the initial shock (A_0^*):

$$\frac{\partial \eta}{\partial t} = \dot{\eta}_{Imp} - C \triangle U_1 A_0^* \tag{1.20}$$

where $C = 2.5$ is an empirical coefficient based on two-dimension numerical simulations.

1.2.5 Multi-mode perturbations

In most of the applications, the initial perturbation of the interfaces can be expressed as a superimposition of multiple single-mode perturbations of different amplitudes and wavelengths. In this case it was found that in the non-linear regime the perturbations growth has the form (Youngs (1994), Alon et al. (1995), Dimonte et al. (1955)):

$$\eta \sim (\triangle U t)^{\theta} \tag{1.21}$$

with the growth exponent θ between 0 and 1. Considering that the evolution of the stability represented by the growth rates of the individual modes is dominated by the just saturated mode, Dimonte et al. (1955) show that the overall growth exponent should be $\theta = 1/2$. However, the evolution of the multi-mode RM instability is strongly dependent on the initial amplitude and the spectrum of the perturbation.
A theoretical and computational study of the influence of the initial conditions on the growth exponent was conducted by Youngs (2004). Considering the initial power spectrum of the perturbation of the form $P(\kappa) \sim k^m$, the dependency of the growth exponent on the power spectrum is:

$$\theta = max \left(0.24, \frac{2}{m+5}\right) \tag{1.22}$$

with the value $\theta = 0.24$ corresponding to the growth rate of the small wave length modes ($m = 3.3$). A linear growth should be expected in the case of an initial spectrum given by $m = -3$.

A recent numerical study of Thornber et al. (2010) suggests values for the growth exponent between 0.26 and 0.3 for the narrow-band initial perturbations and $\theta = 2/3$ for the broad-band case ($m = -2$). The experimental studies of Dimonte and Schneider (2000) and Oron et al. (2001) found that the growth rate of the bubbles is given by $\theta_B = 0.25 \pm 0.05$ and that the growth rate of the spikes is $\theta_S \simeq \theta_B$ for $A_0 < 0.8$ and increases to $\theta_S \approx 1$ as the initial Atwood number tends to 1.

The linear electric motor experiments of Dimonte and Schneider (2000) found:

$$\frac{\theta_S}{\theta_B} = \left(\frac{1 + A_0}{1 - A_0}\right)^{0.21 \pm 0.05}. \tag{1.23}$$

More complex models have been developed for the late non-linear regime of the Richtmyer-Meshkov instability, such as potential models (Oron et al. (2001), Goncharov (2002)) and drag-buoyancy models (Youngs (1991), Shvarts et al. (1995)).

Chapter 2

Governing Equations

The state of a fluid is considered to be completely defined if its density, pressure and velocity are known in each point of the flow domain and at each time. The evolution of these quantities are described by models based on the conservation principles in classical mechanics. These models are usually represented by a set of differential equations describing the variation of the conservative quantities as the combined result the production, convection and diffusion terms. The most complete description of a single fluid flow is given by the Navier-Stokes model, presented in the first section of this chapter. A good approximation of the Navier-Stokes model in the case of high Reynolds numbers (high velocities and low viscosities) is the Euler model described in the second section.

Regarding the multicomponent flows, a complete description would be given by the density, pressure and velocity fields for each of the component fluids, requiring thus transport equations foe each of the species. A simpler solution would be considering only the physical quantities characterizing the mixture, and some additional quantities describing the concentrations of the component fluids in each point. The two approaches will be discussed in section 2.5.

The last sections of this chapter are dedicated to the fundamentals of turbulence modeling. Turbulence models represent an approximation of the Navier-Stokes or Euler models obtained by considering only the time or spatial averages of the flow quantities and modeling the influence of the random fluctuations characteristic to

turbulent flows. The two turbulence models investigated in this work will be presented in detail in sections 2.7 and 2.8.

2.1 The Navier-Stokes model

The Navier-Stokes model is the most general fluid dynamics model based on the conservation principles for mass, momentum and energy in classical mechanics. Thus, for the general case of three-dimensional compressible flows, the mathematical formulation of this model in a Cartesian system of reference is represented by the differential equations:

$$\frac{\partial \rho}{\partial t} + \frac{\partial}{\partial x_i}(\rho u_i) = 0 \tag{2.1}$$

$$\frac{\partial}{\partial t}(\rho u_i) + \frac{\partial}{\partial x_j}(\rho u_i u_j) = \rho g_i - \frac{\partial p}{\partial x_i} + \frac{\partial \tau_{ij}}{\partial x_j}, \quad i = 1, 2, 3 \tag{2.2}$$

$$\frac{\partial}{\partial t}(\rho E) + \frac{\partial}{\partial x_i}(\rho E u_i) = -\frac{\partial q_i}{\partial x_i} + \rho g_i u_i - \frac{\partial}{\partial x_i}(p u_i) + \frac{\partial}{\partial x_i}(\tau_{ij} u_j) \tag{2.3}$$

The right hand side of equation 2.2 contains the sources for the three Cartesian momentum components, represented by the external forces per unit mass g, the pressure p and the viscous stresses t. For Newtonian fluids, the viscous stresses are usually modeled as:

$$\tau_{i,j} = 2\mu S_{ij} + \left(\mu' - \frac{2}{3}\mu\right)\frac{\partial u_k}{\partial x_k}\delta_{i,j}, \quad i, j = 1, 2, 3 \tag{2.4}$$

where μ is the dynamic viscosity, μ' is the bulk viscosity, δ is the Kronecker operator and S is the strain rate tensor:

$$S_{ij} = \frac{1}{2}\left(\frac{\partial u_i}{\partial x_j} + \frac{\partial u_j}{\partial x_i}\right), \quad i, j = 1, 2, 3 \tag{2.5}$$

The viscosity μ depends in general on the pressure and temperature. The Sutherland's formula gives the dependency of the viscosity of a gas on the temperature:

$$\mu(T) = \mu(T_0)\frac{T_0 + C_S}{T + C_S}\left(\frac{T}{T_0}\right)^{3/2} \tag{2.6}$$

where T_0 is a reference temperature and C_S is a constant. In the case of liquids, the viscosity decreases with the temperature. However, in many theoretical and practical applications, the viscosity can be considered constant.
The bulk viscosity (or the second viscosity coefficient) is important only when high pressure and density gradients are present in the flow. It is neglected in most of the practical applications.
The equation 2.3 describes the variation of the total energy E, defined as the sum of the internal energy per unit mass e and the kinetic energy per unit mass:

$$E = e + \frac{1}{2}u_k u_k \tag{2.7}$$

The first term in the total energy equation 2.3 represents the diffusive heat flux, usually modeled according to Fourier's law:

$$q_i = -k_c \frac{\partial T}{\partial x_i}, \quad i = 1, 2, 3 \tag{2.8}$$

where k_c is the thermal conductivity of the fluid. The last terms in the right hand side of the equation 2.7 are the mechanical works of the external forces, pressure and viscous stresses, representing the source for the total energy. For more generality, additional energy sources (such as chemical reactions) can be added on the right-hand side of the equation. Moving the pressure term in the left-hand side, the energy equation can be written as:

$$\frac{\partial}{\partial t}(\rho E) + \frac{\partial}{\partial x_i}(\rho H u_i) = -\frac{\partial q_i}{\partial x_i} + \rho g_i u_i + \frac{\partial}{\partial x_i}(\tau_{ij} u_j) \tag{2.9}$$

where $H = h + u_k u_k/2$ is the total enthalpy per unit mass and $h = e + p/\rho$ is the internal enthalpy per unit mass. It is useful to derive a transport equation for the internal energy e which can replace the equation 2.3. First, from the continuity and momentum equations 2.1, 2.2 the equation for the kinetic energy per unit mass $u_k u_k/2$ is obtained:

$$\frac{\partial}{\partial t}\left(\rho \frac{u_k u_k}{2}\right) + \frac{\partial}{\partial x_i}\left(\rho \frac{u_k u_k}{2} u_i\right) = u_i g_i - u_i \frac{\partial p}{\partial x_i} + u_j \frac{\partial \tau_{ij}}{\partial x_i} \tag{2.10}$$

The internal energy equation is obtained by subtracting the kinetic energy equation 2.10 from the total energy equation 2.3:

$$\frac{\partial}{\partial t}(\rho e) + \frac{\partial}{\partial x_i}(\rho e u_i) = -\frac{\partial q_i}{\partial x_i} - p\frac{\partial u_i}{\partial x_i} + \tau_{ij}\frac{\partial u_j}{\partial x_i} \tag{2.11}$$

An important observation is the fact that the external forces g_i do not have a direct influence on the internal energy. The last term in the equation 2.11 is the viscous dissipation, representing the rate of conversion of the kinetic energy into heat due to the viscous stresses.

2.2 The Euler model

The Euler model can be regarded as the simplification of the Navier-Stokes model for the case when the viscous and diffusive effects can be neglected. The Euler transport equations can by simply obtained by substituting $\mu = \mu' = 0$ and $k_c = 0$ into the Navier-Stokes equations 2.1-2.3:

$$\frac{\partial \rho}{\partial t} + \frac{\partial}{\partial x_i}(\rho u_i) = 0 \tag{2.12}$$

$$\frac{\partial}{\partial t}(\rho u_i) + \frac{\partial}{\partial x_j}(\rho u_i u_j) = \rho g_i - \frac{\partial p}{\partial x_i}, \quad i = 1, 2, 3 \tag{2.13}$$

$$\frac{\partial}{\partial t}(\rho E) + \frac{\partial}{\partial x_i}(\rho E u_i) = \rho g_i u_i - \frac{\partial}{\partial x_i}(p u_i) \tag{2.14}$$

The energy equation 2.14 can be written in terms of the total enthalpy per unit mass:

$$\frac{\partial}{\partial t}(\rho E) + \frac{\partial}{\partial x_i}(\rho H u_i) = \rho g_i u_i \tag{2.15}$$

The corresponding transport equation for the internal energy is:

$$\frac{\partial}{\partial t}(\rho e) + \frac{\partial}{\partial x_i}(\rho e u_i) = -p\frac{\partial u_i}{\partial x_i} \tag{2.16}$$

As the Navier-Stokes transport equations, the Euler system of equations 2.12-2.14(2.16) must be closed by some thermodynamic relations which will be presented in the

next section. Note that the Euler model is valid when the convective transport terms are much more important than the viscous production terms and the diffusive fluxes.

2.3 Thermodynamic relations

The Navier-Stokes and the Euler models represented by the transport equations 2.1-2.3 and 2.12-2.14 must be closed by a series of thermodynamic equations describing the relation between temperature, pressure, density and internal energy. The equation of state for perfect gases reads:

$$p = c\mathcal{R}T \tag{2.17}$$

where T is the temperature, c is the molar concentration of the fluid and $\mathcal{R} = 8.314J/(mol\ K)$ is the universal gas constant. If the molar mass of the fluid is M, then $M = \rho c$ and the equation 2.17 can be written:

$$p = \rho RT \tag{2.18}$$

where $R = \mathcal{R}/M$ is the specific gas constant. As a consequence of the first principle of thermodynamics, the specific gas constant satisfies the relation:

$$R = c_{\mathrm{p}} - c_{\mathrm{v}} \tag{2.19}$$

where c_{p} ans c_{v} are the specific caloric capacities at constant pressure and constant volume, respectively. It is important to mention that if γ is the adiabatic exponent of the fluid, satisfying:

$$p/\rho^{\gamma} = constant \tag{2.20}$$

for an adiabatic thermodynamic process, then:

$$\gamma = \frac{c_{\mathrm{p}}}{c_{\mathrm{v}}} \tag{2.21}$$

The internal energy per unit mass e is:

$$e = c_{\mathrm{v}} T \tag{2.22}$$

According to the equations 2.18, 2.19 and 2.22, the internal enthalpy $h = e + p/\rho$ can be expressed as:

$$h = e + \frac{p}{\rho} = c_{\mathrm{p}} T = \gamma e \tag{2.23}$$

The thermodynamic relations 2.18, 2.19 and 2.22 are enough to close the Navier-Stokes and Euler systems of equations 2.1-2.3 and 2.12-2.14. Note that the kinetic theory of gases used for the derivation of the basic thermodynamic equations is based on the assumption that there is no (or very small) interaction between the molecules of the fluid.

2.4 The pressure equation

An evolutive equation for the pressure can be obtained by manipulating the Euler equations for the case of isentropic flows. The second principle of thermodynamics can be written in this case:

$$dh - \frac{dp}{\rho} = de + pd\left(\frac{1}{\rho}\right) = 0 \tag{2.24}$$

For an isentropic flow the following relation is satisfied:

$$\frac{\partial p}{\partial \rho} = a^2 \tag{2.25}$$

where $a = \gamma p/\rho$ is the speed of sound. Combining the equations 2.24 and 2.25:

$$\frac{de}{dp} = \frac{p}{\rho^2 a^2} \tag{2.26}$$

and thus the pressure equation can be obtained from the internal energy equation 2.16:

$$\frac{\partial p}{\partial t} + u_i \frac{\partial p}{\partial x_i} + \rho a^2 \frac{\partial u_i}{\partial x_i} = 0 \tag{2.27}$$

The pressure equation 2.27 replaces the energy equation when the Euler system is written in primitive variables formulation, as it will be discussed in the next chapter, section 3.1.

2.5 Multi-component flows

The basic principles of mass, momentum and energy conservation in continuum classical mechanics can be applied also for the case of multi-component flows. Thus, transport equations describing the flow of fluid mixtures can be derived similarly to the usual Navier-Stokes or Euler models presented previously.This section will present how the conservation principles can be applied to each individual species present in the flow and also to the mixture of fluids.

2.5.1 Thermodynamic considerations

In the following analysis the fluid mixture will be considered composed of N_{Spec} different species, which can occupy together the same point in the flow domain at any time. Thus, the density of the mixture ρ is the sum of the densities of the components ρ_r $(r = 1, ..N_{\text{Spec}})$:

$$\rho = \sum_{r=1}^{N_{\text{Spec}}} \rho_r \tag{2.28}$$

and the mass fractions of the components are:

$$F_r = \frac{\rho_r}{\rho}, \quad r = 1, ..N_{\text{Spec}} \tag{2.29}$$

Similarly, the molar concentration of the mixture c is the sum of the molar concentrations of the components:

$$c = \sum_{r=1}^{N_{\text{Spec}}} c_r \tag{2.30}$$

and the molar fractions of the species are:

$$\chi_r = \frac{c_r}{c}, \quad r = 1, ..N_{\text{Spec}} \tag{2.31}$$

An obvious but important property of the mass and molar fractions is:

$$\sum_{r=1}^{N_{\text{Spec}}} F_r = \sum_{r=1}^{N_{\text{Spec}}} \chi_r = 1 \tag{2.32}$$

In order to understand the significance of the individual pressures and temperatures of the components, it is useful to consider an arbitrary point in flow domain as the centre of a small three-dimensional domain of volume $\mathcal{V}$ (small but non-zero), in which the mixture can be considered homogeneous. The pressure of the mixture acting on the boundary surface of the domain is the sum of the partial pressures of the components:

$$p = \sum_{r=1}^{N_{\text{Spec}}} p_r \tag{2.33}$$

and, according to the universal law for ideal gases (equation 2.17), the individual temperatures of the species are:

$$T_r = \frac{p_r}{c_r \mathcal{R}}, \quad r = 1, ..N_{\text{Spec}} \tag{2.34}$$

The mixture temperature can be easily determined from the equation of state 2.17 applied to the mixture, together with the equations 2.33 and 2.34:

$$T = \sum_{r=1}^{N_{\text{Spec}}} \chi_r T_r \tag{2.35}$$

Considering now that the species are separated into sub-domains of volumes $\mathcal{V}_r$ $(r = 1, N_{\text{Spec}})$ and that this configuration is in hydrostatic equilibrium at the mixture pressure p, the equation of state 2.17 gives for each sub-domain:

$$p = \left(c_r \frac{\mathcal{V}}{\mathcal{V}_r} \right) \mathcal{R} T_r, \quad r = 1, ..N_{\text{Spec}} \tag{2.36}$$

The quantity $f_r = \mathcal{V}_r/\mathcal{V}$ is the volume fraction of the species r and, according to the equations 2.33 and 2.36, it satisfies the relations:

$$f_r = \frac{p_r}{p}, \quad r = 1, ..N_{\text{Spec}} \tag{2.37}$$

$$\sum_{r=1}^{N_{\text{Spec}}} f_R = 1 \tag{2.38}$$

The relations between mass, molar and volume fractions are given by the following equations (easy to demonstrate):

$$F_r = \frac{M_r \chi_r}{\sum_{s=1}^{N_{\text{Spec}}} M_s \chi_s}, \quad r = 1, ..N_{\text{Spec}} \tag{2.39}$$

$$f_r = \frac{T_r \chi_r}{T}, \quad r = 1, ..N_{\text{Spec}} \tag{2.40}$$

Note that the volume fraction is identical with the molar fraction if the component fluids have the same temperature T.
The internal energy per unit volume of the mixture is, in terms of the mixture temperature T and the mixture specific heat c_{v}:

$$\rho e = \rho c_{\text{v}} T \tag{2.41}$$

but it is given also by the sum of the internal energies of the species:

$$\rho e = \sum_{r=1}^{N_{\text{Spec}}} \rho_r e_r \tag{2.42}$$

where e_r is the internal per unit mass of the species r:

$$e_r = c_{\text{v}r} T_r, \quad r = 1, ..N_{\text{Spec}} \tag{2.43}$$

and $c_{\text{v}r}$ is the specific heat at constant volume of the fluid r.
Remarks

1. In many applications, the mixture components are considered to have the

same temperature $T_r = T$ $(r = 1, N_{\text{Spec}})$. In this case, the molar fraction is identical to the volume fraction (equation 2.40) and the specific heat capacities of the mixture are:

$$c_{\text{v}} = \sum_{r=1}^{N_{\text{Spec}}} F_r c_{\text{v}r} \tag{2.44}$$

$$c_{\text{p}} = \sum_{r=1}^{N_{\text{Spec}}} F_r c_{\text{p}r} \tag{2.45}$$

Applying the equation of state to the mixture and to the components having the same temperature T, the following energetic relations are found:

$$e_r = \frac{c_{\text{v}r}}{c_{\text{v}}} e, \quad r = 1, ..N_{\text{Spec}} \tag{2.46}$$

$$h_r = \frac{c_{\text{p}r}}{c_{\text{p}}} h, \quad r = 1, ..N_{\text{Spec}} \tag{2.47}$$

2. The above analysis is based on the assumption that effects of the interaction between the molecules present in the mixture (of the same or different species) are negligible. However, the basic thermodynamic results, such as the relations between fractions and the expression for the mixture specific capacities, are usually considered valid also when viscous and diffusive effects are included in the transport equations.

2.5.2 Transport equations for the species

If $u_{r,i}$ $(i = 1, 2, 3)$ represent the three Cartesian components of the velocity of the fluid r, the corresponding total energy is $E_r = e_r + u_{r,k}u_{r,k}/2$. Then, the mass, momentum and energy equations can be written for each of the species:

$$\frac{\partial \rho_r}{\partial t} + \frac{\partial}{\partial x_i}(\rho_r u_{r,i}) = 0, \quad r = 1, ..N_{\text{Spec}} \tag{2.48}$$

$$\frac{\partial}{\partial t}(\rho_r u_{r,i}) + \frac{\partial}{\partial x_j}(\rho_r u_{r,i} u_j) = \rho_r g_{r,i} - \frac{\partial p_r}{\partial x_i} + \frac{\partial \tau_{r,ij}}{\partial x_j} + \sum_{s=1}^{N_{\text{Spec}}} \Phi_{sr,i},$$
$$r = 1, ..N_{\text{Spec}}, \quad i = 1, 2, 3 \quad (2.49)$$

$$\frac{\partial}{\partial t}(\rho_r E_r) + \frac{\partial}{\partial x_i}(\rho_r E_r u_{r,i}) = -\frac{\partial q_{r,i}}{\partial x_i} + \rho_r g_{r,i} u_{r,i} - \frac{\partial}{\partial x_i}(p_r u_{r,i}) + \frac{\partial}{\partial x_i}(\tau_{r,ij} u_{r,j}) +$$
$$+ \sum_{s=1,s}^{N_{\text{Spec}}} \Psi_{sr}, , \quad r = 1, ..N_{\text{Spec}} \quad (2.50)$$

where $g_{r,i}$ is the external force acting in the i-direction on the fluid r, $\tau_{r,}$ and $q_{r,i}$ are the viscous stress components and the diffusive heat flux associated with the fluid r, $\Phi_{sr,i}$ is the force in the i direction exerted by the fluid s on the fluid r and $\Psi_{sr,i}$ is the total energy transfer from the fluid s to the fluid r. It is obvious that the diagonal components of the tensors Φ and Ψ are zero and that $\Phi_{sr,i} = -\Phi_{rs,i}$, $\Psi_{sr} = -\Psi_{rs}$, for all $r, s = 1, ..N_{Spec},\ i = 1, 2, 3$.

2.5.3 Transport equations for the mixture

The mass equation for the mixture can be obtained by simply adding the equations 2.48 with respect to r:

$$\frac{\partial \rho}{\partial t} + \frac{\partial}{\partial x_i}(\rho u_i) = 0 \quad (2.51)$$

where in this case u_i is the mass-averaged velocity of the mixture:

$$u_i = \sum_{r=1}^{N_{\text{Spec}}} F_r u_{r,i}, \quad i = 1, 2, 3 \quad (2.52)$$

Before deriving the equations for the mixture momentum and energy equations, it is useful to define the volume weighted velocity:

$$v_i = \sum_{r=1}^{N_{\text{Spec}}} f_r u_{r,i}, \quad i = 1, 2, 3 \quad (2.53)$$

Adding the individual momentum equations 2.29, the transport equations for the momentum of the mixture is:

$$\frac{\partial}{\partial t}(\rho u_i) + \frac{\partial}{\partial x_j}(\rho u_i u_j) = \rho g_i - \frac{\partial p}{\partial x_i} + \frac{\partial \tau_{ij}}{\partial x_j} + \frac{\partial \Upsilon_{ij}}{\partial x_j}, \qquad i = 1,2,3 \quad (2.54)$$

where $\varpi_{r,i} = u_{r,i} - u_i$ represents the deviation of the species r from the mass-averaged velocity of the mixture and and the additional tensor Υ_{ij} arises from the nonlinear convective terms in the momentum equations and has the form:

$$\Upsilon_{i,j} = -\sum_{r=1}^{N_{\text{Spec}}} \rho_r \varpi_{r,i} \varpi_{r,j}, \quad i,j = 1,2,3 \quad (2.55)$$

The external and viscous forces acting on the mixture are represented by the sum of the forces acting on the individual fluids:

$$\rho g_i = \sum_{r=1}^{N_{\text{Spec}}} \rho_r g_{r,i}, \quad i,j = 1,2,3 \quad (2.56)$$

$$\tau_{ij} = \sum_{r=1}^{N_{\text{Spec}}} \tau_{r,ij}, \quad i,j = 1,2,3 \quad (2.57)$$

Following the same procedure, the energy transport equation for the mixture can be written:

$$\frac{\partial}{\partial t}(\rho E) + \frac{\partial}{\partial x_i}(\rho E u_i) = -\frac{\partial q_i}{\partial x_i} - \frac{\partial}{\partial x_i}(p\upsilon_i) + \\ + \sum_{r=1}^{N_{\text{Spec}}} \left(\rho_r g_{r,i} u_{r,i} + \frac{\partial}{\partial x_i}(\tau_{r,ij} u_{r,j}) - \frac{\partial}{\partial x_i}\left(\rho_r \varpi_{r,i} E_r\right) \right) \quad (2.58)$$

where the total energy per unit volume is defined as:

$$\rho E = \sum_{r=1}^{N_{\text{Spec}}} \rho_r \left(e_r + \frac{u_{r,k} u_{r,k}}{2} \right) \quad (2.59)$$

The volume-averaged velocity can be expressed in terms of the mass-averaged velocity as:

$$\upsilon_i = u_i + \sum_{r=1}^{N_{\text{Spec}}} f_r \varpi_{r,i},, \quad i,j = 1,2,3 \tag{2.60}$$

and substituting 2.60 into 2.58, the total energy equation can be expressed as:

$$\frac{\partial}{\partial t}(\rho E) + \frac{\partial}{\partial x_i}(\rho E u_i) = -\frac{\partial q_i}{\partial x_i} - \frac{\partial}{\partial x_i}(p u_i) + W_g + W_\tau + \\ + \frac{\partial}{\partial x_i}(\Upsilon_{ij} u_j) - \frac{\partial}{\partial x_i}\left(J_{\text{e}i} + J_{\text{h}i}\right) \tag{2.61}$$

where W_g and W_τ are the mechanical works of the external forces and viscous stresses, respectively, and $J_{\text{e}i}$ and $J_{\text{h}i}$ are additional energy and enthalpy fluxes due to the difference between the velocities of the component fluids (Ramshaw (1993), Ramshaw (2002)). They are defined as:

$$J_{\text{e}i} = \sum_{r=1}^{N_{\text{Spec}}} \rho_r \frac{\varpi_{r,k}\varpi_{r,k}}{2}\varpi_{r,i} \tag{2.62}$$

$$J_{\text{h}i} = \sum_{r=1}^{N_{\text{Spec}}} \rho_r \varpi_{r,i} h_r \tag{2.63}$$

Remarks

1. In the usual case when the external force g is the same for all the species (e.g. the gravitational force), its mechanical work takes the simple form:

$$W_g = \rho g_i u_i \tag{2.64}$$

2. The viscous stresses of the mixture (in 2.54, 2.58 and 2.61) are by definition equal to the sum of the viscous forces of the components. Usually it expressed in the classical form for Newtonian fluids:

$$\tau_{i,j} = \mu\left(\frac{\partial u_i}{\partial x_j} + \frac{\partial u_j}{\partial x_i}\right) - \frac{2}{3}\mu\frac{\partial u_k}{\partial x_k}\delta_{i,j}, \quad i,j = 1,2,3 \tag{2.65}$$

In this case the mechanical work of the viscous forces present in the energy equation is simply:

$$W_\tau = \frac{\partial}{\partial x_i}\left(\tau_{i,j} u_j\right) \tag{2.66}$$

However, some closure assumptions must be made regarding the mixture viscosity μ. A reasonable assumption would be:

$$\mu = \sum_{r=1}^{N_{\text{Spec}}} F_r \mu_r \tag{2.67}$$

3. The diffusive heat flux for the mixture is by definition the sum of the individual fluxes of the component fluids. If the individual diffusive fluxes are expressed according to Fourier's law (equation 2.8), then the mixture flux can be written:

$$q_i = k_{\text{c}} \frac{\partial T}{\partial x_i}, \quad i = 1, 2, 3 \tag{2.68}$$

where k_{c} is the thermal conductivity of the mixture.

4. If the velocities of the species are close to the mass averaged velocity, the transport equations can be simplified by neglecting the tensor Υ and the additional heat flux J_{e} which are proportional to $\varpi_k \varpi_k$. The additional enthalpy tensor J_{h} depends is a linearly on ϖ and must not be neglected (Ramshaw (2002), Cook (2009)).

2.5.4 A simplified mixture model

A simple model for multi-component flows based on the transport equations for the mixture can be obtained starting from the theoretical analysis presented in the previous sections and introducing some simplifying assumptions. First, the component fluids are considered to have the same temperature and small deviations from the mass-averaged velocity of the mixture. The external forces are considered to act equally on the components of the mixture. The mass, momentum and energy

equations are in this case similar to the usual Navier-Stokes equations:

$$\frac{\partial \rho}{\partial t} + \frac{\partial}{\partial x_i}(\rho u_i) = 0 \tag{2.69}$$

$$\frac{\partial}{\partial t}(\rho u_i) + \frac{\partial}{\partial x_j}(\rho u_i u_j) = \rho g_i - \frac{\partial p}{\partial x_i} + \frac{\partial \tau_{ij}}{\partial x_j}, \quad i = 1, 2, 3 \tag{2.70}$$

$$\frac{\partial}{\partial t}(\rho E) + \frac{\partial}{\partial x_i}(\rho E u_i) = -\frac{\partial q_i + J_{\mathrm{h}i}}{\partial x_i} + \rho g_i u_i - \frac{\partial}{\partial x_i}(p u_i) + \frac{\partial}{\partial x_i}(\tau_{ij} u_j) \tag{2.71}$$

The viscous stresses are given by the equation 2.65, where μ is the dynamic viscosity of the mixture. Generally, some assumptions should be made regarding the mixture viscosity, as already mentioned in the previous subsection. The diffusive energy flux q can be modeled by Fourier's law (equation 2.68). The total energy equation contains the additional enthalpy flux J_{h} which can be modeled as a function of the molecular diffusion of the component fluids, as it will be shown later.
The system of equations 2.69-2.71 is supplemented by the transport equations for the mass fractions of the species:

$$\frac{\partial}{\partial t}(\rho F_r) + \frac{\partial}{\partial x_i}(\rho F_r u_i) = -\frac{\partial J_{\mathrm{m}r,i}}{\partial x_i} \quad r = 1, ..N_{\mathrm{Spec}} - 1 \tag{2.72}$$

The property 2.32 substitutes the transport equation for the mass fraction of one of the species. The diffusive mass fluxes $J_{\mathrm{m}r}$ are modeled according to Fick's law:

$$J_{\mathrm{m}r,i} = -\rho \left[D_r \frac{\partial F_r}{\partial x_i} - F_r \sum_{s=1}^{N_{\mathrm{Spec}}} \left(D_s \frac{\partial F_s}{\partial x_i} \right) \right] \tag{2.73}$$

where D_r are diffusion coefficients.
The additional enthalpy flux in the energy equation 2.71 can be modeled as (Cook (2009)):

$$J_{\mathrm{h}i} = \sum_{r=1}^{N_{\mathrm{Spec}}} h_r J_{\mathrm{m}r,i} \tag{2.74}$$

The assumption that the component species have the same temperature makes possible the use of the equations 2.46 and 2.47 for the calculation of the individual internal energies and enthalpies per unit mass h_r from the mixture quantities. The

system of equations 2.69-2.72 is closed by the thermodynamic relations for mixtures of fluids derived in the subsection 2.5.1.

2.6 Turbulence modeling of compressible flows

The concept of turbulence modeling is based on the decomposition of the flow into an averaged part, considered to be deterministic and reproducible, and the relative fluctuating part. The mean part must be considered as a statistical average taken over a large number of experiments, that are assumed identical at a macroscopical level, but are influenced by small and uncontrollable perturbations of the initial and boundary conditions. The averaging procedure depends on the properties of the flow to which it is applied. If a flow is considered to be statistically steady in every point, then a time-averaging operator must be used. In the case of a flow considered to be statistically two-dimensional at each moment, i.e. the flow properties are constant along one spatial direction, then the statical average should be taken over that spatial direction. The choice of the averaging operator implicitly defines the fluctuating part. The mean flow is then simulated numerically and the influence of the fluctuations is taken into account by introducing some closure models. This procedure requires less spatial and time resolution for the discretization of the partial differential equations.

2.6.1 Statistical and Favre averages

The turbulence models are based in general on the Navier-Stokes or Euler model, in which the flow quantities (density, velocity, pressure, etc.) are decomposed into their averages and the corresponding fluctuations. The statistical (Reynolds) average of any quantity ϕ will be noted $\overline{\phi}$ and its corresponding fluctuation ϕ'. In the case of compressible flows, due to the presence of the density in most of the terms of the transport equations, it is useful to define also the Favre (mass) average, which will be noted $\tilde{\phi}$ and it is defined as:

$$\tilde{\phi} = \frac{\overline{\rho\phi}}{\overline{\rho}} \tag{2.75}$$

Even though it is called also the "mass average“, here it will be referred to as the Favre average only, in order to avoid confusion with the mass-averaging procedure for the velocity in the multicomponent flows, presented in section 2.5 (equation MComp14). The fluctuation corresponding to the Favre average for the quantity ϕ will be noted ϕ''

The flow quantities are decomposed into their statistical or Favre averages and the corresponding fluctuations as follows:

$$\begin{aligned}
&\rho = \overline{\rho} + \rho' \\
&p = \overline{p} + p' \\
&u_i = \overline{u}_i + u_i', \quad i = 1,2,3 \\
&u_i = \tilde{u}_i + u_i'', \quad i = 1,2,3 \\
&e = \tilde{e} + e'' \\
&h = \tilde{h} + h'' \\
&T = \tilde{T} + T''
\end{aligned} \tag{2.76}$$

The thermodynamic relations presented in subsection 2.3 are for the mean flow:

$$\overline{p} = \overline{\rho} R \tilde{T} \tag{2.77}$$

$$\tilde{e} = c_{\mathrm{c}} \tilde{T} \tag{2.78}$$

$$\tilde{h} = \tilde{e} + \frac{\overline{p}}{\overline{\rho}} = c_{\mathrm{p}} \tilde{T} \tag{2.79}$$

The following properties of the statistical and Favre averages will be used for the derivation of the mean flow transport equations:

$$\begin{aligned}
&\overline{\phi'} = \overline{\rho \phi''} = 0 \\
&\overline{\phi''} = \overline{\phi} - \tilde{\phi} = -\frac{\overline{\rho' \phi'}}{\overline{\rho}} \\
&\overline{\phi \psi} = \overline{\phi}\,\overline{\psi} + \overline{\phi' \psi'} \\
&\overline{\rho \phi \psi} = \overline{\rho} \tilde{\phi} \tilde{\psi} + \overline{\rho \phi'' \psi''} \\
&\overline{\phi' \psi} = \overline{\phi' \psi'} = \overline{\phi' \psi''}
\end{aligned} \tag{2.80}$$

where ϕ and ψ are two generic quantities.

2.6.2 The Favre-averaged Navier-Stokes equations

First, the decompositions 2.76 are substituted into the Navier-Stokes equations 2.1, 2.2 and 2.9 and then the Favre averaging operator is applied to all the terms [Wilcox1993]. Using the averages properties 2.80, the following transport equations for the mean flow are obtained:

$$\frac{\partial \overline{\rho}}{\partial t} + \frac{\partial \overline{\rho}\tilde{u}_i}{\partial x_i} = 0 \tag{2.81}$$

$$\frac{\partial \overline{\rho}\tilde{u}_i}{\partial t} + \frac{\partial \overline{\rho}\tilde{u}_i\tilde{u}_j}{\partial x_j} = -\frac{\partial \overline{p}}{\partial x_i} + \frac{\partial \bar{\tau}_{ij}}{\partial x_j} - \frac{\partial}{\partial x_j}\left(\overline{\rho u''_i u_j''}\right), \quad i = 1,2,3 \tag{2.82}$$

$$\begin{aligned}\frac{\partial}{\partial t}\left(\bar{\rho}\tilde{e} + \bar{\rho}\frac{\tilde{u}_k\tilde{u}_k}{2} + \frac{\overline{\rho u_k'' u_k''}}{2}\right) + \frac{\partial}{\partial x_i}\left[\tilde{u}_i\left(\bar{\rho}\tilde{h} + \bar{\rho}\frac{\tilde{u}_k\tilde{u}_k}{2} + \frac{\overline{\rho u_k'' u_k''}}{2}\right)\right] = \\ = \frac{\partial}{\partial x_i}\left[-\bar{q}_i - \overline{\rho u''_j h''} + \overline{\tau_{ij}u''_i} - \overline{u''_j\frac{\rho u''_k u''_k}{2}}\right] + \frac{\partial}{\partial x_i}\left[\tilde{u}_j\left(\bar{\tau}_{ij} - \overline{\rho u''_i u''_j}\right)\right]\end{aligned} \tag{2.83}$$

The turbulent stress tensor τ_t and the turbulence kinetic energy K are defined as:

$$\tau_{tij} = -\overline{\rho u_i'' u_j''}, \quad i,j = 1,2,3 \tag{2.84}$$

$$K = \frac{\overline{\rho u_k'' u_k''}}{2\overline{\rho}} \tag{2.85}$$

and the total energy of the mean flow is conventionally defined:

$$E^* = \tilde{e} + \bar{\rho}\frac{\tilde{u}_k\tilde{u}_k}{2} + K \tag{2.86}$$

Note that E^* is not equal to the Favre average of E. The definitions 2.84 and 2.85 imply that the trace of the turbulent stress tensor is:

$$\tau_{tkk} = 2\overline{\rho}K \tag{2.87}$$

and this property must be considered when the turbulence stresses are modeled. There are three remaining correlations in the right-hand side of the averaged energy equation 2.83 First, the turbulent heat transport, modeled as the diffusion of the

mean internal enthalpy/energy:

$$-\frac{\partial}{\partial x_i}\left(\overline{\rho h'' u_i''}\right) = \frac{\partial}{\partial x_i}\left(D_h \frac{\partial \tilde{h}}{\partial x_i}\right) = \frac{\partial}{\partial x_i}\left(D_e \frac{\partial \tilde{e}}{\partial x_i}\right) \tag{2.88}$$

The last two correlations are the molecular diffusion and the turbulent transport of K, usually modeled together as the diffusion of the turbulence kinetic energy:

$$\frac{\partial}{\partial x_i}\left(\overline{\tau_{ij} u''_i}\right) - \frac{\partial}{\partial x_i}\left(\overline{\rho \frac{u''_k u''_k}{2} u_i''}\right) = \frac{\partial}{\partial x_i}\left(D_K \frac{\partial K}{\partial x_i}\right) \tag{2.89}$$

where D_h,D_e and D_K are diffusive coefficients, with $D_h = \gamma D_e$. Now the averaged energy equation can be written:

$$\begin{aligned}\frac{\partial}{\partial t}\left(\bar{\rho} E^*\right) + \frac{\partial}{\partial x_i}\left(\bar{\rho} H^* \tilde{u}_i\right) = \\ = \frac{\partial}{\partial x_i}\left(D_e \frac{\partial \tilde{e}}{\partial x_i}\right) + \frac{\partial}{\partial x_i}\left(D_K \frac{\partial K}{\partial x_i}\right) + \frac{\partial}{\partial x_i}\left[\left(\tau_{ij} + \tau_{\mathrm{t}ij}\right)\tilde{u}_j\right] - \frac{\partial \bar{q}_i}{\partial x_i}\end{aligned} \tag{2.90}$$

where $H^* = E^* + \bar{p}$ is the total enthalpy of the mean flow.
The viscous stresses of the mean flow are usually expressed as a function of the Favre-averaged strain tensor:

$$\bar{\tau}_{i,j} = 2\nu\bar{\rho}\bar{S}_{ij} + \left(-\frac{2}{3}\nu\bar{\rho}\right)\frac{\partial \tilde{u}_k}{\partial x_k}\delta_{i,j}, \quad i,j = 1,2,3 \tag{2.91}$$

where ν is the kinematic viscosity of the fluid and the average strain rate tensor is:

$$\tilde{S}_{ij} = \frac{1}{2}\left(\frac{\partial \tilde{u}_i}{\partial x_j} + \frac{\partial \tilde{u}_j}{\partial x_i}\right), \quad i,j = 1,2,3 \tag{2.92}$$

Similarly, the conductive flux can be also expressed based on the Fourier's law applied to the mean flow:

$$\bar{q}_i = -k_{\mathrm{c}}\frac{\partial \tilde{T}}{\partial x_i}, \quad i = 1,2,3 \tag{2.93}$$

An alternative mean flow energy equation can be obtained if the averaging procedure presented above is applied to the energy equation 2.3 without moving the

pressure terms in the left-hand side:

$$\frac{\partial}{\partial t}\left(\overline{\rho}E^{*}\right)+\frac{\partial}{\partial x_i}\left(\overline{\rho}H^{*}\tilde{u}_i\right)= \\ =\frac{\partial}{\partial x_i}\left(D_e\frac{\partial\tilde{e}}{\partial x_i}\right)+\frac{\partial}{\partial x_i}\left(D_K\frac{\partial K}{\partial x_i}\right)+\frac{\partial}{\partial x_i}\left[\left(\tau_{ij}+\tau_{\mathrm{t}ij}\right)\tilde{u}_j\right]-\frac{\partial\bar{q}_i}{\partial x_i}-\frac{\partial}{\partial x_i}\left(\overline{p}\bar{u}_i\right) \quad (2.94)$$

where the turbulent heat transport is modeled together with the pressure-velocity correlation:

$$-\frac{\partial\overline{\rho e''u_i''}}{\partial x_i}-\frac{\partial}{\partial x_i}\left(\overline{p'u'_i}\right)=\frac{\partial}{\partial x_i}\left(D_e\frac{\partial\tilde{e}}{\partial x_i}\right) \quad (2.95)$$

The mechanical work of the pressure in new energy equation 2.94 contains the statistical averaged velocity $\bar{u}_i$, while the momentum, the kinetic energy and the convection velocity of the mean flow are defined in terms of the Favre average $\tilde{u}_i$. Therefore, the turbulence models employing the mean energy equation in this form must contain a transport equation or other closure relations for the quantity $\tilde{u}_i-\bar{u}_i$.

2.6.3 The Favre-averaged Euler equations

The decompositions 2.76 and the Favre average operator can be applied in the same way on the Euler equations 2.12, 2.13 and 2.14 (2.16). Thus, the mean flow equations for the inviscid and non-diffusive case are:

$$\frac{\partial\overline{\rho}}{\partial t}+\frac{\partial}{\partial x_i}\left(\overline{\rho}\tilde{u}_i\right)=0 \quad (2.96)$$

$$\frac{\partial}{\partial t}\left(\overline{\rho}\tilde{u}_i\right)+\frac{\partial}{\partial x_j}\left(\overline{\rho}\tilde{u}_i\tilde{u}_j\right)=-\frac{\partial\overline{p}}{\partial x_i}+\frac{\partial\tau_{\mathrm{t}ij}}{\partial x_j}, \quad i=1,2,3 \quad (2.97)$$

$$\frac{\partial}{\partial t}\left(\overline{\rho}E^{*}\right)+\frac{\partial}{\partial x_i}\left(\overline{\rho}H^{*}\tilde{u}_i\right)= \\ =\frac{\partial}{\partial x_i}\left(D_e\frac{\partial\tilde{e}}{\partial x_i}\right)+\frac{\partial}{\partial x_i}\left(D_K\frac{\partial K}{\partial x_i}\right)+\frac{\partial}{\partial x_i}\left(\tau_{ij}\tilde{u}_j\right) \quad (2.98)$$

The alternative averaged energy equation 2.94 is in this case:

$$\frac{\partial}{\partial t}\left(\overline{\rho}E^{*}\right)+\frac{\partial}{\partial x_i}\left(\overline{\rho}E^{*}\tilde{u}_i\right)= \\ =\frac{\partial}{\partial x_i}\left(D_e\frac{\partial\tilde{e}}{\partial x_i}\right)+\frac{\partial}{\partial x_i}\left(D_K\frac{\partial K}{\partial x_i}\right)-\frac{\partial}{\partial x_i}\left(\bar{p}\bar{u}_i\right)+\frac{\partial}{\partial x_i}\left(\tau_{\mathrm{t}ij}\tilde{u}_j\right) \quad (2.99)$$

The turbulent diffusion terms in the energy equations 2.98 and 2.99 model the same correlations as given in the relations 2.88, 2.89 (2.95).

2.6.4 The Favre-averaged transport equations for multi-component flows

In the case of multi-component flows, the averaging procedure presented in the two previous subsections can be applied either on the transport equations written for each of the species (equations 2.48-2.50), either to the transport equations of the mixture (equations 2.51, 2.54, 2.58). For simplicity, the simple mixture model presented in 2.5.4 will be considered next.

The averaged mass, momentum and energy equations for the mixture have the same form as the averaged Navier-Stokes equations 2.81-2.83. The Boussinesq approximation can be used for calculating the turbulent stresses and the turbulent diffusion of the mixture internal energy and turbulence kinetic energy are modeled by the equations 2.88, 2.89 applied for the mixture quantities. The averaged transport equation for the mass fractions of the fluids has the form:

$$\frac{\partial}{\partial t}(\bar{\rho}\tilde{F}_r)+\frac{\partial}{\partial x_i}(\bar{\rho}\tilde{F}_r\tilde{u}_i)=-\frac{\partial\tilde{J}_{\mathrm{m}r,i}}{\partial x_i}-\frac{\partial}{\partial x_i}\left(\overline{\rho F''_r u''_i}\right) \quad r=1,..N_{Spec}-1 \quad (2.100)$$

The turbulent diffusion of the mass fraction can be modeled as:

$$-\frac{\partial}{\partial x_i}\left(\overline{\rho F''_r u''_i}\right)=\frac{\partial}{\partial x_i}\left(D_F\frac{\partial\tilde{F}_r}{\partial x_i}\right)x_i \quad r=1,..N_{Spec}-1 \quad (2.101)$$

and the mass fluxes $\tilde{J}_{\mathrm{m}r,i}$ can be modeled using the Fick's law applied to the mean flow of the mixture.

2.6.5 The turbulence kinetic energy equation

The exact equation for the turbulence kinetic energy K can be derived starting with the momentum equations 2.2 written in non-conservative form:

$$\rho\frac{\partial u_i}{\partial t} + \rho u_j\frac{\partial u_i}{\partial x_j} = -\frac{\partial p}{\partial x_i} + \frac{\partial \tau_{ij}}{\partial x_j}, \quad i = 1, 2, 3 \tag{2.102}$$

The equations 2.102 are first multiplied by the fluctuation ${u_i}''$ and then the statistical average operator is applied to all the terms. Summing over the spatial direction index i, the following equation is obtained:

$$\overline{\rho {u_i}''\frac{\partial u_i}{\partial t}} + \overline{\rho u_i u_j\frac{\partial u_i}{\partial x_j}} = -\overline{u_i\frac{\partial p}{\partial x_i}} + \overline{u_i\frac{\partial \tau_{ij}}{\partial x_j}} \tag{2.103}$$

Introducing the decompositions 2.76 and using the properties 2.80, the following transport equation for K can be written in conservative form:

$$\begin{aligned}\frac{\partial}{\partial t}\left(\rho K\right) + \frac{\partial}{\partial x_i}\left(\rho K\tilde{u}_i\right) = \tau_{\mathrm{t},ij}\frac{\tilde{u}_j}{x_i} - \overline{\tau_{ij}\frac{\partial {u''}_j}{\partial x_i}} + \frac{\partial}{\partial x_i}\left(\overline{\tau_{ij}{u''}_i} - \overline{\rho {u''}_i\frac{{u''}_i{u''}_i}{2}}\right) \\ - \frac{\partial}{\partial x_i}\left(\overline{p'{u''}_i}\right) + \overline{p'\frac{\partial {u''}_i}{\partial x_i}} - \overline{{u''}_i}\frac{\partial \bar{p}}{\partial x_i}\end{aligned} \tag{2.104}$$

The first term in the right-hand side is the rate of energy transfer from the mean flow to the fluctuations, thus representing the turbulence kinetic energy production. The dissipation rate of the turbulent kinetic energy ϵ is given by the second term and can can be regarded as the work of the viscous forces produced with the fluctuating velocity u''.

$$\bar{\rho}\epsilon = \overline{\tau_{ij}\frac{\partial {u''}_j}{\partial x_i}} \tag{2.105}$$

The following two correlations are the molecular diffusion and the turbulent transport of the turbulence kinetic energy, modeled according to the equation 2.89. The first pressure-velocity correlation are the turbulent pressure diffusion and dilatation. There are no generally validated models for these terms and they are usually neglected. The last correlation is the pressure work, and, according to the second

property in 2.80, can be written as:

$$-\overline{u''}_i \frac{\partial \bar{p}}{\partial x_i} = (\tilde{u}_i - \bar{u}_i) \frac{\partial \bar{p}}{\partial x_i} \tag{2.106}$$

The difference between the statistical and Favre-averaged velocities is relatively large in the presence of important density fluctuations. Thus, the pressure work represents a significant source for the turbulence kinetic energy in the case of highly compressible or multi-component flows.

2.6.6 Turbulence models

The averaging procedures applied to the Navier-Stokes or Euler equations produce additional unknowns in the governing equations, such as the turbulent stresses and the turbulent diffusion terms. The concept of turbulence modeling is based on solving the averaged transport equations together with some additional algebraic or differential equations necessary for closing the system. According to the number and type of the closure equations, the turbulence models can be classified in the following main categories:

1. Eddy viscosity turbulence models: the turbulent stresses are calculated from the mean flow using Boussinesq's approximation:

$$\tau_{\mathrm{t},ij} = \frac{1}{2}\mu_{\mathrm{t}} \left(\frac{\partial \tilde{u}_i}{\partial x_j} + \frac{\partial \tilde{u}_j}{\partial x_i} \right) - \frac{2}{3}\delta_{i,j} \left(\mu_{\mathrm{t}} \frac{\partial \tilde{u}_k}{\partial x_k} + \bar{\rho} K \right) \quad i,j = 1,2,3 \tag{2.107}$$

   where μ_{t} is the eddy (or turbulent) viscosity and represents an additional unknown. Depending on the approach for calculating the eddy viscosity, there are:

   Zero-equations models: the eddy viscosity is calculated from the mean flow quantities by an algebraic expression. In the case of simple boundary layer flows, where it was first applied, the eddy viscosity is proportional to the gradient of the averaged velocity.

   One-equation models: a differential transport equation involving convec-

tion, diffusion, and production is solved usually for the eddy viscosity. The most used is the the one-equation turbulence model of Spalart and Allmaras (1992).

Two-equations models: two transport equations are solved, usually one for the turbulence kinetic energy K and the second for another turbulence quantity, such as: the dissipation rate of the turbulence kinetic energy ϵ, the specific dissipation rate $\omega = \epsilon/K$ or the eddy size L. The eddy viscosity is calculated then as an algebraic function of the turbulence kinetic energy and the second turbulence quantity. From dimensional considerations: $\mu_t \sim K^2/\epsilon \sim K^{3/2}/\omega \sim K^{1/2}L$. The most used two-equations models are the $K-\epsilon$ model first introduced by Launder and Sharma (1974) and various versions of the $K-\omega$ model (Wilcox (1993), Menter (1994), Wilcox (2000)).

2. Turbulence stress models (or second order closure models): transport equations are solved for all the components of the turbulence stress tensor and sometimes for additional correlations. The original turbulence model was introduced by Launder et al. (1974).

Regarding the multi-component flows, the turbulence models can be based on the averaged transport of the species, such as the multi-component turbulence model of Youngs (1984), or on the averaged equations for the mixture quantities, such as the second-order closure model of Besnard et al. (1992) and the two-equations eddy viscosity models of Gauthier and Bonnet (2000) and Dimonte and Tipton (2006). The last two models are main subject of the present work and are presented in the following two sections.

2.7 The $K-L$ turbulence model

The first turbulence model employed in the present study is a single fluid, two equation eddy viscosity model ($K-L$) proposed by Dimonte and Tipton (2006). It was developed for the turbulent self-similar regime of the the Rayleigh-Taylor and Richtmyer-Meshkov mixing. The starting point for deriving the model equations are the drag-buoyancy models for the self-similar growth of the RT and RM

instabilities (Alon et al. (1995), Dimonte (2000)). The model was design to correctly simulate growth of the bubbles and spikes, assumed to be self similar to the size of the large turbulent structures, L. Additional constraints imposed to the model are to be independent of the reference system and realizable in presence of shock waves.

2.7.1 The mean flow transport equations

The mean flow is described by the Favre-averaged conservation equations for the mass, momentum and energy of the mixture, and for the mass fractions of the components:

$$\frac{\partial \bar{\rho}}{\partial t} + \frac{\partial}{\partial x_i}(\bar{\rho}\tilde{u}_i) = 0 \tag{2.108}$$

$$\frac{\partial}{\partial t}(\bar{\rho}\tilde{u}_i) + \frac{\partial}{\partial x_j}(\bar{\rho}\tilde{u}_i\tilde{u}_j) = -\frac{\partial \bar{p}}{\partial x_i} + \frac{\partial \tau_{\mathrm{t},ij}}{\partial x_j}, \quad i = 1,2,3 \tag{2.109}$$

$$\frac{\partial}{\partial t}(\bar{\rho}\tilde{e}) + \frac{\partial}{\partial x_i}(\bar{\rho}\tilde{e}\tilde{u}_i) = \frac{\partial}{\partial x_i}\frac{\mu_{\mathrm{t}}}{\sigma_e}\frac{\partial \tilde{e}}{\partial x_i} - p\frac{\partial \tilde{u}_i}{\partial x_i} - S_K + \bar{\rho}\epsilon \tag{2.110}$$

$$\frac{\partial}{\partial t}(\bar{\rho}\tilde{F}) + \frac{\partial}{\partial x_i}(\bar{\rho}\tilde{F}\tilde{u}_i) = \frac{\partial}{\partial x_i}\frac{\mu_{\mathrm{t}}}{\sigma_F}\frac{\partial \tilde{F}}{\partial x_i}, \quad r = 1,..N_{Spec} \tag{2.111}$$

The viscous stresses and the heat conduction were neglected. The turbulent stresses $\tau_{\mathrm{t},ij}$ and the turbulence kinetic K energy are defined by the equations 2.84 and 2.85, respectively. The transport equation for the internal energy e contains a source term for the turbulence kinetic energy S_K and the dissipation ϵ, which be defined later. The diffusion coefficients σ_e and σ_F are, respectively, the turbulent Prandtl and Schmidt numbers (model constants).

2.7.2 The equations for the turbulence quantities

The transport equation for the turbulence kinetic energy proposed by Dimonte and Tipton (2006) is:

$$\frac{\partial}{\partial t}(\bar{\rho}K) + \frac{\partial}{\partial x_i}(\bar{\rho}K\tilde{u}_i) = \frac{\partial}{\partial x_i}\frac{\mu_{\mathrm{t}}}{\sigma_K}\frac{\partial K}{\partial x_i} + \tau_{\mathrm{t},ij}\frac{\partial \tilde{u}_i}{\partial x_j} + S_K - \bar{\rho}\epsilon \tag{2.112}$$

The turbulence kinetic energy source S_K models the pressure work mentioned in section 2.6.5 and represents turbulence enhancement due to the interaction between density and pressure gradients. In the case of a impulsive (RM) instability it is always a positive quantity:

$$S_K = C_B \bar{\rho} u_{\mathrm{t}} \left| A_{\mathrm{L}i} g_i \right| \tag{2.113}$$

where $g_i = -(1/\bar{\rho})\partial\bar{p}/\partial x_i$ is the acceleration, $u_{\mathrm{t}} = \sqrt{2K}$ is the turbulence velocity, **A** is a local Atwood number (defined later in this section) and C_B is a model coefficient. If the instability is RT-like, the turbulence source is set to zero if the pressure and density gradients have the same signs:

$$S_K = C_B \bar{\rho} u_{\mathrm{t}} \mathrm{max}\left(0,\ A_{\mathrm{L}i} g_i\right) \tag{2.114}$$

The choice of the instability type is based on the acceleration of the fluid particles. Thus, the instability is considered to be impulsive (RM-like) if the velocity variation of the particle over a time step is higher than the turbulence velocity u_{t}, and gradual (RT-like) otherwise. This procedure is suitable for a Lagrangian framework of the CFD solver and it is dependent on the size of the time step (or the CFL number).
The local Atwood number **A** is defined as:

$$A_{\mathrm{L}i} = A_{0i} + A_{\mathrm{SS}i}, \quad i = 1, 2, 3 \tag{2.115}$$

where A_{0i} recovers the initial Atwood number at the interfaces between fluids, where the density is discontinuous, and $A_{\mathrm{SS}i}$ represents the local Atwood number in the self-similar regime, when the density variation is gradual. The initial Atwood number can be expressed in terms of the reconstructed values of the densities at the faces bordering the computational cells:

$$A_{0i} = \frac{\bar{\rho}_{\mathrm{R}} - \bar{\rho}_{\mathrm{L}}}{\bar{\rho}_{\mathrm{R}} + \bar{\rho}_{\mathrm{L}}}, \quad i = 1, 2, 3 \tag{2.116}$$

where the subscripts R and L stand for the left side and right side of the face, respectively. The computational cells are assumed hexahedral with the faces perpendicular to the spatial directions i. The "MinMod" reconstruction procedure (described

in 3.5) ensures the correct estimation of the local Atwood at the initial interface discontinuity. The self-similar Atwood number has the form:

$$A_{SSi} = C_A \frac{L}{\bar{\rho} + L\,|\partial\bar{\rho}/\partial x_i|} \frac{\partial\bar{\rho}}{\partial x_i}, \quad i = 1, 2, 3 \tag{2.117}$$

where $C_A = 2$ is a model constant. Further details regarding the computation of the local Atwood number can be found in Dimonte and Tipton (2006). A simplified formula for calculating the self similar Atwood number was employed by Chiravalle (2006):

$$A_{SSi} = \frac{L}{\bar{\rho}} \frac{\partial\bar{\rho}}{\partial x_i} \tag{2.118}$$

The dissipation of the turbulence kinetic energy, ϵ, is represented here by the mechanical work of the drag forces acting on the turbulent structures (bubbles and spikes):

$$\epsilon = C_D \frac{{u_t}^{3/2}}{L} \tag{2.119}$$

where C_D is the drag coefficient (model constant).
The last transport equation is written for the eddy size L:

$$\frac{\partial}{\partial t}(\bar{\rho}L) + \frac{\partial}{\partial x_i}(\bar{\rho}L\tilde{u}_i) = \frac{\partial}{\partial x_i}\frac{\mu_t}{\sigma_L}\frac{\partial L}{\partial x_i} + C_L\rho u_t + C_C\rho L\frac{\partial\tilde{u}_i}{\partial x_i} \tag{2.120}$$

where the production is given by $C_L\rho u_t$, the last term models the compressibility effects and C_L, C_C and σ_L are model constants.

2.7.3 Turbulence stresses and eddy viscosity

The turbulence stresses are modeled according to the Boussinesq approximation:

$$\tau_{t,ij} = \frac{1}{2}\mu_t\left(\frac{\partial\tilde{u}_i}{\partial x_j} + \frac{\partial\tilde{u}_j}{\partial x_i}\right) - \frac{2}{3}\delta_{i,j}\left(\mu_t\frac{\partial\tilde{u}_k}{\partial x_k} + \bar{\rho}K\right) \quad i, j = 1, 2, 3 \tag{2.121}$$

It is recommended that in the presence of strong shocks the deviatoric part of this tensor should be omitted and the turbulence stresses should be approximated by the turbulence pressure (Sinha, Mahesh, and Candler (Sinha et al.), Dimonte and

Tipton (2006)):

$$\tau_{t,ij} = -C_P \delta_{i,j} \bar{\rho} K \quad i,j = 1,2,3 \tag{2.122}$$

where C_P is a constant. The eddy viscosity is calculated using the usual relation for the two equations eddy viscosity models:

$$\mu_t = C_\mu \bar{\rho} L \sqrt{u_t} \tag{2.123}$$

where C_μ is a model constant.

2.7.4 Model coefficients

The $K - L$ model presented above contains a set of coefficients which determined from experimental, numerical and theoretical results.

First, the drag coefficient C_D and the buoyancy coefficient C_B influence the balance between the production and the dissipation of the turbulence kinetic energy, and must ensure the growth rates of the RT and RM instabilities found experimentally and numerically. Thus, they are functions of the α and θ parameters mentioned in sections 1.1 and 1.2. The influence of the drag and buoyancy coefficients on the RMI and RTI growth rates are investigated by Dimonte and Tipton (2006) and Chiravalle (2006). The local Atwood number coefficient has the value $C_A = 2$ in order to recover the initial Atwood number at the interface. The compression coefficient in the transport equation for L (2.120) is $C_C = 1/3$, determined from the condition that the large eddies preserve their mass under compression (the diffusive effects are considered negligible).

The eddy size diffusion coefficient σ_L is determined from the condition that approximatively half of the initial potential energy in an RT configuration will be transformed into turbulence kinetic energy, and the rest into heat, as found experimentally. The diffusive coefficients must satisfy the relation: $\sigma_e = \sigma_F = \sigma_K = 2\sigma_L$ in order to preserve the self-similarity of the flow.

If the turbulent stresses are approximated by the turbulent pressure, as in equation 2.122, then the pressure coefficient C_P must ensure the turbulence kinetic energy enhancement produced by RM instability, as observed experimentally and numer-

Coefficient	Expression	Value
Eddy viscosity (C_μ)	N/A	1.0
Turbulent pressure (C_P)	N/A	$2/3$
Eddy size production (C_L)	N/A	1
Eddy compression (C_C)	N/A	$1/3$
Local Atwood number (C_A)	N/A	2
Drag (TKE dissipation) (C_D)	$\frac{1-1.5\theta}{2\theta}$	1.25 ± 0.4
Buoyancy (TKE source) (C_B)	$4\alpha_b(1+2C_D)$	0.84 ± 0.11
Diffusion eddy size (σ_L)	$\frac{C_\mu}{32\alpha_b}$	0.5 ± 0.1
Diffusion internal energy (σ_e)	$2\sigma_L$	1.0 ± 0.2
Diffusion mass fraction (σ_F)	$2\sigma_L$	1.0 ± 0.2
Diffusion TKE (σ_K)	$2\sigma_L$	1.0 ± 0.2

Table 2.1: The $K-L$ model coefficients

ically. In this case, the eddy viscosity coefficient C_μ appears only in the turbulent diffusion terms which are scaled by the turbulent diffusion coefficients σ_e, σ_F,σ_K and σ_L. Thus, the eddy viscosity coefficient can be conveniently set $C_\mu = 1$. The expressions and the values of all the model coefficients proposed by Dimonte and Tipton (2006) are summarized in table 2.7.4.

2.7.5 Modifications of the model

In the present work, a few modifications of the original $K-L$ model have been made in order to improve the performance of the model and to ensure the compatibility with the numerical framework employed. The modifications concern the energy of the mean flow, the turbulent kinetic energy source term and the turbulent stresses:

1. The transport equation for the internal energy 2.110 is replaced by the equation for the total energy E^* variation which can be obtain directly by combining the Favre averaged equations 2.108-2.110 and the turbulence kinetic energy 2.112:

$$\frac{\partial}{\partial t}(\bar{\rho}E^*)+\frac{\partial}{\partial x_i}(\bar{\rho}E^*\tilde{u}_i) = \frac{\partial}{\partial x_i}\frac{\mu_\mathrm{t}}{\sigma_e}\frac{\partial \tilde{e}}{\partial x_i}+\frac{\partial}{\partial x_i}\frac{\mu_\mathrm{t}}{\sigma_K}\frac{\partial K}{\partial x_i}-\frac{\partial}{\partial x_i}(p\tilde{u}_i)+\frac{\partial \tau_{\mathrm{t},ij}\tilde{u}_j}{\partial x_i} \quad (2.124)$$

where the mean flow total energy per unit mass E^* was already defined in the section 2.6 by the equation 2.86.

2. The choice of the expression for calculating the turbulence kinetic energy source S_K (equation 2.113 or 2.114) is based on the time scales of the mean flow Θ and of the turbulent structures Θ_t, defined as:

$$\Theta = \bar{\rho}\left(\gamma\frac{\bar{p}}{\bar{\rho}}\right)^{1/2}\left(\frac{\partial\bar{p}}{\partial x_k}\frac{\partial\bar{p}}{\partial x_k}\right)^{-1/2} \tag{2.125}$$

$$\Theta_t = \frac{L}{K^{1/2}} \tag{2.126}$$

The instability will be considered impulsive if the time scale of the mean flow is much smaller than the turbulent time scale, and gradual otherwise:

$$S_K = \begin{cases} C_B\bar{\rho}u_t\left|A_{Li}g_i\right| & \text{if } \Theta < \Lambda_\Theta\Theta_t \\ \\ C_B\bar{\rho}u_t\max\left(0,\ A_{Li}g_i\right) & \text{otherwise} \end{cases} \tag{2.127}$$

where $\Lambda_\Theta < 1$ is a coefficient.This criterion is based on the sudden acceleration of a fluid particle (estimated by the pressure gradient) and it is not directly dependent on the CFL number.

3. As already mentioned, the simplifying approach of modelling the turbulent stresses as the turbulence pressure prevents the turbulence model from being applicable to the cases when the shear turbulent stresses are important (such as the Kelvin-Helmholtz instability). Therefore, in addition to the formula 2.122, the classical approach based on Boussinesq's approximation will be considered, but with the realizability condition:

$$-2\bar{\rho}K \leq \tau_{tii} \leq 0 \tag{2.128}$$

In this case the eddy viscosity coefficient should take the usual value for the $K-L$ models $C_\mu \simeq 0.1$. The condition 2.128 is a direct consequence of the turbulence stresses definition 2.84 and it was employed more restrictively in

the $K-\epsilon$ model presented in the next section.

2.8 The $k-\epsilon$ model for the RT instability

The second turbulence model investigated here is a one-dimensional two-equation eddy viscosity turbulence model proposed by Gauthier and Bonnet (2000) for the simulation of the turbulent mixing induced by the Rayleigh-Taylor and Richtmyer-Meshkov instabilities. It was derived from the classical $K-\epsilon$ model (Launder and Spalding (1974)), with additional algebraic constraints imposed in order to ensure the realizability of the model in the presence of strong shocks. The validations of the model were conducted based on the shock-tube experimental studies of Andronov et al. (1976) and Houas (1985).

2.8.1 The mean flow transport equations

The mean flow is considered inviscid and one-dimensional. The velocity and the turbulent stress tensor have only one component, u and τ_{t}, respectively. The conservation equations for the mass, momentum, energy of the mixture are:

$$\frac{\partial \bar{\rho}}{\partial t}+\frac{\partial}{\partial x}(\bar{\rho}\tilde{u})=0 \tag{2.129}$$

$$\frac{\partial}{\partial t}(\bar{\rho}\tilde{u})+\frac{\partial}{\partial x}(\bar{\rho}\tilde{u}\tilde{u})=-\frac{\partial \bar{p}}{\partial x}+\frac{\partial \tau_{\mathrm{t}}}{\partial x} \tag{2.130}$$

$$\frac{\partial}{\partial t}(\bar{\rho}\tilde{e})+\frac{\partial}{\partial x}(\bar{\rho}\tilde{e}\tilde{u})=\frac{\partial}{\partial x}\left(D_e\frac{\partial \tilde{e}}{\partial x}\right)-p\frac{\partial \tilde{u}}{\partial x}-S_K+\bar{\rho}\epsilon \tag{2.131}$$

and the transport equations for the mass fractions of the components are:

$$\frac{\partial}{\partial t}(\bar{\rho}\tilde{F})+\frac{\partial}{\partial x}(\bar{\rho}\tilde{F}\tilde{u})=\frac{\partial}{\partial x}\left(D_e\frac{\partial \tilde{F}}{\partial x}\right),\quad r=1,..N_{Spec} \tag{2.132}$$

The diffusive coefficients are defined as:

$$D_e=\bar{\rho}\frac{C_\mu}{\sigma_e}\frac{K^2}{\epsilon} \tag{2.133}$$

$$D_F = \bar{\rho}\frac{C_\mu}{\sigma_F}\frac{K^2}{\epsilon} \tag{2.134}$$

where C_μ, σ_e and σ_F are model constants. The internal energy contains the dissipation rate ϵ and the additional turbulence kinetic energy source S_K, which will be defined later.

2.8.2 The equations for the turbulence quantities

The model contains two additional transport equations for the turbulent kinetic energy K and the dissipation rate ϵ:

$$\frac{\partial}{\partial t}(\bar{\rho}K) + \frac{\partial}{\partial x}(\bar{\rho}K\tilde{u}) = \frac{\partial}{\partial x}\left(D_K\frac{\partial K}{\partial x}\right) + \tau_{\mathrm{t}}\frac{\partial \tilde{u}}{\partial x} + S_K - \bar{\rho}\epsilon \tag{2.135}$$

$$\frac{\partial}{\partial t}(\bar{\rho}\epsilon) + \frac{\partial}{\partial x}(\bar{\rho}\epsilon\tilde{u}) = \frac{\partial}{\partial x}\left(D_\epsilon\frac{\partial \epsilon}{\partial x}\right) + C_{\epsilon 1}\frac{\epsilon}{K}\tau_{\mathrm{t}}\frac{\partial \tilde{u}}{\partial x} + C_{\epsilon 0}\frac{\epsilon}{K}S_K - C_{\epsilon 2}\bar{\rho}\frac{\epsilon^2}{K} - C_{\epsilon 3}\bar{\rho}\epsilon\frac{\partial \tilde{u}}{\partial x} \tag{2.136}$$

The additional turbulence source S_K is the result of the turbulent pressure work (section 2.6.5, equation 2.104) and it is modeled as:

$$S_K = \begin{cases} -\mathrm{sign}\left(\dfrac{\partial \bar{\rho}}{\partial x}\right)\ \min\left(|J_{\mathrm{m}}|, |J_{\mathrm{m}Max}|\right)\dfrac{1}{\bar{\rho}}\dfrac{\partial \bar{p}}{\partial x} & \text{if } \dfrac{D\tilde{u}}{Dt}\dfrac{\partial \bar{\rho}}{\partial x} > 0 \\ 0 & \text{if } \dfrac{D\tilde{u}}{Dt}\dfrac{\partial \bar{\rho}}{\partial x} < 0 \end{cases} \tag{2.137}$$

where $J_{\mathrm{m}} = \overline{\rho' u''}$ is the turbulent diffusive mass flux, modeled as:

$$J_{\mathrm{m}} = -D_\rho\frac{\partial \bar{\rho}}{\partial x} \tag{2.138}$$

The high density and pressure gradients present in the RM flows could lead to unphysically large values, so the mass flux calculated with the relation 2.138 is limited by the maximum value:

$$J_{\mathrm{m}Max} = \Lambda_\rho\left(\bar{\rho}\tau_{\mathrm{t}}\right)^{1/2} \tag{2.139}$$

where $\Lambda_\rho = 0.67$ is a model constant. The diffusion coefficients for the turbulence kinetic energy, dissipation rate and mass are:

$$D_K = \bar{\rho}\frac{C_\mu}{\sigma_K}\frac{K^2}{\epsilon} \tag{2.140}$$

$$D_\epsilon = \bar{\rho}\frac{C_\mu}{\sigma_\epsilon}\frac{K^2}{\epsilon} \tag{2.141}$$

$$D_\rho = \frac{C_\mu}{\sigma_\rho}\frac{K^2}{\epsilon} \tag{2.142}$$

where σ_K, σ_ϵ and σ_ρ are additional model constants.

2.8.3 Turbulence stresses and eddy viscosity

The turbulence stress is modeled according to Boussinesq's approximation applied for one-dimensional flows:

$$\tau_{\mathrm{t}} = -\frac{4}{3}\mu_{\mathrm{t}}\frac{\partial \tilde{u}}{\partial x} + \frac{2}{3}\bar{\rho}K \tag{2.143}$$

with the realizability condition:

$$-\Lambda_{max}\bar{\rho}K < \tau_{\mathrm{t}} < -\Lambda_{min}\bar{\rho}K \tag{2.144}$$

imposed in order to prevent unphysically values produced by the high gradients present in the flows with strong shocks. The eddy viscosity has the standard form:

$$\mu_{\mathrm{t}} = C_\mu\bar{\rho}\frac{K^2}{\epsilon} \tag{2.145}$$

2.8.4 Model coefficients

The model equations presented in the previous subsections contain the standard coefficients of the $K-\epsilon$ (Launder and Spalding (1974), Wilcox 2003), but also some additional constants which scale the additional terms present in the case RM and RT turbulent flows, such as the turbulent pressure work, the mass fraction diffusion, the turbulent mass diffusion and the limiters for the turbulent stresses. All

Coefficient	Value
Eddy viscosity (C_μ)	0.09
Production of ϵ ($C_{\epsilon 1}$)	1.47
Additional source for ϵ ($C_{\epsilon 0}$)	N/A
Dissipation of ϵ ($C_{\epsilon 2}$)	1.9
Compressibility ($C_{\epsilon 3}$)	0
Diffusion internal energy (σ_e)	0.9
Diffusion mass fraction (σ_F)	1.0
Diffusion TKE (σ_K)	0.87
Diffusion dissipation (σ_ϵ)	1.3
Diffusion mass (σ_ρ)	N/A
Limiter for mass flux (Λ_ρ)	0.67
Limiters for turb. stresses (Λ_{min} and Λ_{max})	0.1 and 1.25

Table 2.2: The $K-\epsilon$ model coefficients

of these coefficients are presented in table 2.8.4, as given by Gauthier and Bonnet (2000). Note that the compressibility effects in the dissipation transport equation 2.136 was neglected, as the mean flow is considered divergence-free. The coefficients $C_{\epsilon 0}$ and σ_ρ, scaling the additional source for ϵ and the turbulent mass diffusion, respectively, are problem dependent. The decaying rate of the turbulence kinetic energy in the incompressible Rayleigh-Taylor problem gives $C_{\epsilon 0} = 1 + 0.2 * \sigma_\rho$.

2.8.5 Modifications of the model

The relation 2.137 modelling the RM/RT turbulence source S_K cannot capture the amplification of the turbulence kinetic energy by an impulsive acceleration when the pressure and density gradients have the same sign. Therefore, the expression for S_K was modified in present work in a similar way as for the $K-L$ model, the distinction between the impulsive and gradual acceleration being made again by

the ratio between the average flow and turbulent time scales:

$$S_K = \begin{cases} \min\left(|J_{\mathrm{m}}|, |J_{\mathrm{m}Max}|\right) \dfrac{1}{\bar{\rho}} \left|\dfrac{\partial \bar{p}}{\partial x}\right| & \text{if } \Theta < \Lambda_\Theta \Theta_t \\ -\text{sign}\left(\dfrac{\partial \bar{\rho}}{\partial x}\right) \min\left(|J_{\mathrm{m}}|, |J_{\mathrm{m}Max}|\right) \dfrac{1}{\bar{\rho}} \dfrac{\partial \bar{p}}{\partial x} & \text{if } \Theta \geq \Lambda_\Theta \Theta_t \text{ and } \dfrac{\partial \bar{p}}{\partial x}\dfrac{\partial \bar{\rho}}{\partial x} < 0 \\ 0 & \text{otherwise} \end{cases} \tag{2.146}$$

where the time scales Θ and Θ_t are defined in the previous section (equations 2.125 and 2.126, respectively).

The internal energy equation is replaced again by the transport equation for the total energy E^*:

$$\frac{\partial}{\partial t}(\bar{\rho} E^*) + \frac{\partial}{\partial x_i}(\bar{\rho} E^* \tilde{u}_i) = \frac{\partial}{\partial x_i} D_e \frac{\partial \tilde{e}}{\partial x_i} + \frac{\partial}{\partial x_i} D_K \frac{\partial K}{\partial x_i} - \frac{\partial}{\partial x_i}(p \tilde{u}_i) + \frac{\partial \tau_{\mathrm{t},ij} \tilde{u}_j}{\partial x_i} \tag{2.147}$$

with the diffusion coefficients D_e and D_K given by the relations 2.133 and 2.140.

2.9 Concluding remarks

The $K - L$ and $K - \epsilon$ turbulence models will be used in this work for simulating the turbulent mixing by the Rayleigh-Taylor and Richtmyer-Meshkov instabilities for different test cases. The transport equations presented in the sections 2.7 and 2.8 are closed by the thermodynamic relations for multicomponent flows given in section 2.5. The absence of the viscous stresses in the model equations is based on the assumption that the turbulence viscosity μ_{t} is much larger than the molecular viscosity μ.

Chapter 3

Numerical methods

The transport equations of the eddy viscosity turbulence models applied to inviscid compressible flows are usually derived from the Euler model presented in section 2.2. Therefore they retain the main mathematical properties of the Euler equations, such as the non-linearity of the convective and pressure terms. The Euler system of equations can be considered the representative non-linear convection model in fluid mechanics. Therefore, the numerical methods developed for the integration of the Euler equations are used for many other models in fluid mechanics when the convective terms are considered to be dominant. This chapter will present first the basic numerical approaches for solving the Euler equations, insisting on the finite volume method which involves numerical schemes for time and spatial integration. The discretization of the turbulence terms and the implementation of the numerical schemes will be discussed in the last section of the chapter.

3.1 Formulations and mathematical properties of the Euler equations

The aim of this section is to discuss the main mathematical formulations of and properties of the Euler equations presented in section 2.2. For simplicity, no external forces acting on the fluid will be considered. There are three possible representations of the Euler model: *i)* conservative, when the unknowns of the equations

are considered to be the mass, momentum and energy per unit volume, *i)* non-conservative, when the unknowns of the equations are the density, the components of the velocity and the pressure, and *i)* characteristic, based on the hyperbolic character of the equations. The transport equations 2.12-2.14 are closed by the thermodynamic relations given in section 2.3.

3.1.1 The conservative formulation

The Euler system of equations 2.12-2.14 presented in section 2.2 can be written in the compact matrix form:

$$\frac{\partial U}{\partial t} + \frac{\partial \Phi_x}{\partial x} + \frac{\partial \Phi_y}{\partial y} + \frac{\partial \Phi_z}{\partial z} = 0 \tag{3.1}$$

where U is the column matrix containing the conservative variables:

$$U = \begin{bmatrix} \rho \\ \rho u \\ \rho v \\ \rho w \\ \rho E \end{bmatrix} \tag{3.2}$$

and $\Phi = (\Phi_x, \Phi_y, \Phi_z)$ represents the flux vector:

$$\Phi_x = \begin{bmatrix} \rho u \\ \rho u^2 + p \\ \rho uv \\ \rho uw \\ \rho uH \end{bmatrix} ; \; \Phi_y = \begin{bmatrix} \rho v \\ \rho vu \\ \rho v^2 + p \\ \rho vw \\ \rho vH \end{bmatrix} ; \; \Phi_z = \begin{bmatrix} \rho w \\ \rho wu \\ \rho wv \\ \rho w^2 + p \\ \rho wH \end{bmatrix} \tag{3.3}$$

Considering a control volume Ω, the conservative equations 3.1 can be written in the integral form:

$$\frac{d}{dt}\int_{\Omega} U \, d\mathcal{V} + \int_{\partial\Omega} \Phi \mathbf{n}_e \, d\mathcal{A} = \int_{\Omega} Q \, d\mathcal{V} \tag{3.4}$$

where $\mathbf{n}_e$ is the exterior normal vector at the boundary surface $\partial\Omega$ of the control volume.

Defining the Jacobian matrix:

$$\mathbf{A} = \frac{\partial \Phi}{\partial U} \tag{3.5}$$

the Euler equations can be written in the quasi-linear differential form:

$$\frac{\partial U}{\partial t} + \mathbf{A}\nabla U = Q \tag{3.6}$$

where the Jacobian of the system is:

$$A_x = \begin{bmatrix} 0 & 1 & 0 & 0 & 0 \\ -u^2 + \frac{\gamma-1}{2}\mathbf{u}^2 & (3-\gamma)u & -(\gamma-1)v & -(\gamma-1)w & \gamma-1 \\ -uv & v & u & 0 & 0 \\ -uw & w & 0 & u & 0 \\ -u[\gamma E - (\gamma-1)\mathbf{u}^2] & \gamma E - \frac{\gamma-1}{2}(\mathbf{u}^2 + 2u^2) & -(\gamma-1)uv & -(\gamma-1)uw & \gamma u \end{bmatrix} \tag{3.7}$$

$$A_y = \begin{bmatrix} 0 & 0 & 1 & 0 & 0 \\ -uv & v & u & 0 & 0 \\ -v^2 + \frac{\gamma-1}{2}\mathbf{u}^2 & -(\gamma-1)u & (3-\gamma)v & -(\gamma-1)w & \gamma-1 \\ -vw & 0 & w & v & 0 \\ -v[\gamma E - (\gamma-1)\mathbf{u}^2] & -(\gamma-1)uv & \gamma E - \frac{\gamma-1}{2}(\mathbf{u}^2 + v^2) & -(\gamma-1)wv & \gamma v \end{bmatrix} \tag{3.8}$$

$$A_z = \begin{bmatrix} 0 & 0 & 1 & 0 & 0 \\ -uw & w & 0 & u & 0 \\ -vw & 0 & w & v & 0 \\ -w^2 + \frac{\gamma-1}{2}\mathbf{u}^2 & -(\gamma-1)u & -(\gamma-1)v & (3-\gamma)w & \gamma-1 \\ -w[\gamma E - (\gamma-1)\mathbf{u}^2] & -(\gamma-1)uw & -(\gamma-1)vw & \gamma E - \frac{\gamma-1}{2}(\mathbf{u}^2 + w^2) & \gamma w \end{bmatrix} \tag{3.9}$$

where $\mathbf{u}^2 = u^2 + v^2 + w^2$ is the magnitude of the velocity. Note that:

$$\Phi_x = A_y U;\ \Phi_y = A_y U;\ \Phi_z = A_z U \tag{3.10}$$

which represents the homogeneity property of the Euler equations.

3.1.2 The primitive variable formulation

Defining the primitive variables V:

$$V = \begin{bmatrix} \rho \\ u \\ v \\ w \\ p \end{bmatrix} \tag{3.11}$$

the Euler system of equations can be written in the non-conservative form:

$$\frac{\partial V}{\partial t} + \mathbf{B}\nabla V = 0 \tag{3.12}$$

where the vector matrix $\mathbf{B} = (B_x, B_y, B_z)$ has the form:

$$B_x = \begin{bmatrix} u & \rho & 0 & 0 & 0 \\ 0 & u & 0 & 0 & \frac{1}{\rho} \\ 0 & 0 & u & 0 & 0 \\ 0 & 0 & 0 & u & 0 \\ 0 & \rho a^2 & 0 & 0 & u \end{bmatrix} ; \; B_y = \begin{bmatrix} v & 0 & \rho & 0 & 0 \\ 0 & v & 0 & 0 & 0 \\ 0 & 0 & v & 0 & \frac{1}{\rho} \\ 0 & 0 & 0 & v & 0 \\ 0 & 0 & \rho a^2 & 0 & v \end{bmatrix} ; \; B_y = \begin{bmatrix} w & 0 & 0 & \rho & 0 \\ 0 & w & 0 & 0 & 0 \\ 0 & 0 & w & 0 & 0 \\ 0 & 0 & 0 & w & \frac{1}{\rho} \\ 0 & 0 & 0 & \rho a^2 & w \end{bmatrix} \tag{3.13}$$

As mentioned in the previous chapter (section 2.4), the last equation in the system 3.12 is valid only in the case of an isentropic flow.

3.1.3 The characteristic variable formulation

In the absence of external the forces ($g = 0$), the Euler equations for the one-dimensional case ($v = w = 0$, $\partial/\partial y = \partial/\partial z = 0$) can be written in differential conservative form:

$$\frac{\partial U}{\partial t} + \frac{\partial \Phi_x}{\partial x} = 0 \tag{3.14}$$

where the conservative variables are:

$$U = \begin{bmatrix} \rho \\ \rho u \\ \rho E \end{bmatrix} \tag{3.15}$$

and the fluxes in the x-direction are:

$$\Phi_x = \begin{bmatrix} \rho u \\ \rho u^2 + p \\ \rho u H \end{bmatrix} \tag{3.16}$$

The quasi-linear form of the equation 3.14 is in this case:

$$\frac{\partial U}{\partial t} + A_x \frac{\partial U}{\partial x} = Q \tag{3.17}$$

where the Jacobian matrix of the system is:

$$A_x = \frac{d\Phi_x}{dU} = \begin{bmatrix} 0 & 1 & 0 \\ \frac{1}{2}(3-\gamma)u^2 & (3-\gamma)u & \gamma - 1 \\ -u[\gamma E - (\gamma-1)u^2] & \gamma E - \frac{3}{2}(\gamma-1)u^2 & \gamma u \end{bmatrix} \tag{3.18}$$

The eigenvalues of the Jacobian A_x are:

$$\lambda_1 = u - a;\ \lambda_2 = u;\ \lambda_3 = u + a \tag{3.19}$$

where $a = (\gamma p/\rho)^{1/2}$ is the local velocity of sound. The corresponding eigenvectors are:

$$P^{[1]} = \begin{bmatrix} 1 \\ u - a \\ H - ua \end{bmatrix};\ P^{[2]} = \begin{bmatrix} 1 \\ u \\ \frac{u^2}{2} \end{bmatrix};\ P^{[3]} = \begin{bmatrix} 1 \\ u + a \\ H + ua \end{bmatrix} \tag{3.20}$$

and the Jacobian matrix is diagonalizable:

$$A_x = P \Lambda P^{-1} \tag{3.21}$$

where:

$$\Lambda = \begin{bmatrix} \lambda_1 & 0 & 0 \\ 0 & \lambda_2 & 0 \\ 0 & 0 & \lambda_3 \end{bmatrix} \tag{3.22}$$

$$P = [P^{[1]}|P^{[2]}|P^{[3]}] = \begin{bmatrix} 1 & 1 & 1 \\ u-a & u & u+a \\ H-ua & \frac{u^2}{2} & H+ua \end{bmatrix} \tag{3.23}$$

The matrix of the one-dimensional Euler equations in primitive-variable formulation is:

$$B_x = \begin{bmatrix} u & \rho & 0 \\ 0 & u & \frac{1}{\rho} \\ 0 & \rho a^2 & u \end{bmatrix} \tag{3.24}$$

and has the same eigenvalues $\lambda_{1,2,3}$ given by 3.19 and the eigenvectors:

$$Q^{[1]} = \begin{bmatrix} 1 \\ -\frac{a}{\rho} \\ a^2 \end{bmatrix};\ Q^{[2]} = \begin{bmatrix} 1 \\ 0 \\ 0 \end{bmatrix};\ Q^{[3]} = \begin{bmatrix} 1 \\ \frac{a}{\rho} \\ a^2 \end{bmatrix} \tag{3.25}$$

Thus, the matrix B_x is also diagonalizable:

$$B_x = Q\Lambda Q^{-1} \tag{3.26}$$

where Q is the matrix containing the eigenvectors $Q^{[1]}, Q^{[2]}, Q^{[3]}$:

$$Q = [Q^{[1]}|Q^{[2]}|Q^{[3]}] = \begin{bmatrix} 1 & 1 & 1 \\ -\frac{a}{\rho} & 0 & \frac{a}{\rho} \\ a^2 & 0 & a^2 \end{bmatrix} \tag{3.27}$$

With the final note that the eigenvalues of the Jacobian matrices A_x and B_x are real and distinct and that the eigenvectors are linearly independent, it is concluded that the differential system of equations is strictly hyperbolic and homogeneous. The system of equations can be linearised around a given state U_0 and takes the

canonical form:

$$\frac{\partial \hat{V}}{\partial t} + \Lambda(U_0)\frac{\partial \hat{V}}{\partial x} = 0 \tag{3.28}$$

where $\hat{V} = Q^{-1}V$ represents the characteristic variables. The hyperbolic system of equations 3.28 shows that each characteristic variable $\hat{V}_i$ is constant along the corresponding characteristic curve $dx/dt = \lambda_i$. When the Riemann problem is applied to the Euler equations, the two extreme eigenvalues λ_1 and λ_3 correspond to a shock or rarefication wave in the solution, while λ_2 is related to the presence of the contact discontinuity.

The necessary and sufficient condition for the hyperbolic character of the three-dimensional system of equations 3.12 is that the projection of the vector $\mathbf{B}$ on any spatial direction is diagonalizable. The demonstration is based on the rotational invariance of the Euler equations (Billet and Toro (1998), Toro (1999))

Considering an arbitrary spatial direction defined by the unit vector $\mathbf{n} = (n_x, n_y, n_z)$, the Jacobian of the system of equations 3.12 takes the form:

$$\mathbf{Bn} = Q^{-1}\Lambda Q \tag{3.29}$$

where the diagonal matrix contains the eigenvalues of the system:

$$\lambda_1 = \mathbf{un} - a;\ \lambda_2 = \lambda_3 = \lambda_4 = \mathbf{un};\ \lambda_5 = \mathbf{un} + a \tag{3.30}$$

and the matrix Q contains the corresponding eigenvectors:

$$Q = \begin{bmatrix} \frac{\rho}{2a} & n_x & n_y & n_z & \frac{\rho}{2a} \\ -\frac{n_x}{2} & 0 & -n_z & n_y & \frac{n_x}{2} \\ -\frac{n_y}{2} & n_z & 0 & -n_x & \frac{n_y}{2} \\ -\frac{n_z}{2} & -n_y & n_x & 0 & \frac{n_z}{2} \\ \frac{\rho}{2a} & 0 & 0 & 0 & \frac{\rho}{2a} \end{bmatrix} \tag{3.31}$$

However, when numerical methods are sought for solving the hyperbolic Euler equations, it is useful to consider the split equations on the three spatial directions. For example, the x-split Euler equations are represented by the equation 3.14 but

with the conservative variables U and the flux Φ_x corresponding to the three dimensional problem. In this case the eigenvalues of the system are $\lambda_1 = u - a$, $\lambda_2 = \lambda_3 = \lambda_4 = u$, $\lambda_5 = u + a$. When the Riemann problem is applied to the split-Euler equations, the extreme values λ_1 and λ_5 are again associated with the presence of shock or rarefication waves, and the multiple eigenvalue $\lambda_2 = \lambda_3 = \lambda_4$ is associated with a contact discontinuity across which only ρ, v and w can be discontinuous. Thus, the solution of the split Riemann problem is represented by the solution (ρ, u, p) for the one-dimensional problem and the variables v and w which are passively transported with the wave speed $\lambda_2 = \lambda_3 = \lambda_4$.

3.2 The finite volume method

The finite method-type methods are based on the integral form of the conservation equations (equation 3.4 for the case of the Euler model). They are based on the decomposition of the computational domain Ω into a number N_{FV} of discrete elements $\Omega_i,\ i = 1, ..N_{\text{FV}}$ called finite volumes. In the general case of three-dimensional flows, the finite volumes are polyhedral, each of them being bordered by $N_{\text{S}i}$ plane surfaces. To each of the finite volumes, an average state of the flow is assigned, defined by the volume-averaged conservative variables $\bar{U}_i$:

$$\bar{U}_i = \frac{1}{\mathcal{V}_i} \int_{\Omega_i} U \, d\mathcal{V},\ i = 1, ..N_{\text{FV}} \tag{3.32}$$

where $\mathcal{V}_i$ is the volume of the Ω_i.The integral conservation equation 3.4 applied to each of the finite volume takes the form:

$$\frac{d\bar{U}_i(t)}{dt} = Y(U_i(t)),\ i = 1, ..N_{\text{FV}} \tag{3.33}$$

where the right hand side of the system of equations is:

$$Y(U_i(t)) = \frac{1}{\mathcal{V}_i} \left[-\int_{\partial\Omega_i} \Phi(U)\mathbf{n}_{\text{e}} \, d\mathcal{A} + \int_{\Omega_i} Q(U) \, d\mathcal{V} \right],\ i = 1, ..N_{\text{FV}} \tag{3.34}$$

The total flux through the boundary of the finite volume Ω_i can be expressed as the sum of the average fluxes through the corresponding plane faces:

$$\int_{\partial\Omega_i} \Phi(U)\mathbf{n}_\mathrm{e}\, d\mathcal{A} = \sum_{j=1}^{N_{\mathrm{S}i}} \mathcal{A}_{i,j}\bar{\Phi}_{i,j}\mathbf{n}_{i,j},\ i = 1,..N_{\mathrm{FV}} \tag{3.35}$$

where $\mathcal{A}_{i,j}$ and $\mathbf{n}_{i,j}$ are the areas and the unit normal vectors corresponding the faces of each finite volume. The average fluxes $\bar{\Phi}_{i,j}$ are estimated from the average values of the conservative variables U corresponding to the neighboring finite volumes, as it will be described in the next sections.
In the case of the Euler model, the source term in the right hand side of the equation 3.33 is given by the external forces $\mathbf{g}$ and it is expressed as:

$$\int_{\Omega_i} Q(U)\, d\mathcal{V} = \mathcal{V}_i Q(\bar{U}_i),\ i = 1,..N_{\mathrm{FV}} \tag{3.36}$$

Once the source terms and the fluxes are computed from the cell-averaged state of the flow, the ordinary differential equation 3.33 can be solved using an explicit scheme scheme such as the Runge-Kutta type schemes presented in the last section of this chapter. Note that in the case of the Navier-Stokes or some turbulence models, the right hand side term $Y(U(t))$ contains additional terms, such as viscous stresses, diffusive fluxes, and turbulence sources which are also estimated from the volume averaged variables $\bar{U}$.

3.3 The Godunov method for the Euler equations

The Godunov method (Godunov (1959)) is a numerical scheme designed to solve the Euler equations in integral conservative form 3.4, based on a finite volume approach. The conservative variables are considered to be constant inside each of the finite volume and the estimation of the fluxes Φ is based on the exact solution of the Riemann problem arising at the interfaces between cells. Considering the one-dimensional case of the Euler equations, the conservative equation 3.33 takes the

form:

$$\frac{d\bar{U}_i}{dt} = \frac{1}{x_{i+1/2} - x_{i-1/2}} \left(\Phi_{i+1/2} - \Phi_{i-1/2} \right) \tag{3.37}$$

where $\bar{U}$ represents the averaged conservative variable on the finite volume $\Omega_i = [x_{i-1/2}, x_{i+1/2}]$:

$$\bar{U}_i(t) = \frac{1}{x_{i+1/2} - x_{i-1/2}} \int_{x_{i-1/2}}^{x_{i+1/2}} U(x,t)\, dx,\ i = 1, ..N_{\text{FV}} \tag{3.38}$$

and $\Phi_{i+1/2}, \Phi_{i-1/2}$ are the fluxes through the two interfaces:

$$\Phi_{i-1/2} = \Phi(U_{i-1/2}),\ \Phi_{i+1/2} = \Phi(U_{i+1/2}) \tag{3.39}$$

The conservative variables $U_{i-1/2}$ and $U_{i+1/2}$ represent the solution of the Riemann problem at the two interfaces:

$$\frac{\partial U}{\partial t} + \frac{\partial \Phi(U)}{\partial x} = 0,\ U(x,0) = \begin{cases} U_{\text{L}} & \text{if } x < x_{i\pm1/2} \\ U_{\text{R}} & \text{if } x > x_{i\pm1/2} \end{cases} \tag{3.40}$$

with $U_{\text{L}} = \bar{U}_{i-1},\ U_{\text{R}} = \bar{U}_i$ at the left interface and $U_{\text{L}} = \bar{U}_{i1},\ U_{\text{R}} = \bar{U}_{i+1}$ at the right interface. Because the states at the left and right sides of the interfaces are equal to the averaged states on the adjacent cells, the original Godunov method is of first order accurate in space. Higher orders of accuracy can be obtained by using different interpolation procedures for the estimation of the conservative variables U_{L} and U_{R}, such as MUSCL (Van Leer (1977)) or WENO (Balsara and Shu (2000)) methods.

3.4 The HLL and HLLC solvers

The Godunov method presented in the previous section requires the exact solution of the Riemann problem for the Euler equations at the cell faces. Due to the complexity of the wave structure of the solution, there are no direct analytical methods for solving the Riemann problem and some iterative procedures are necessary. Therefore the computation of the Godunov fluxes requires important

computational effort. An alternative solution is to use approximative methods for estimating the fluxes. Among the most well-known approximative solvers are the Roe (Roe (1981)), Osher (Osher and Solomon (1982)), HLL (Harten et al. (1983)) and HLLC (Toro (1999)) schemes. The last two methods have been implemented for the present numerical study.

3.4.1 The HLL solver

The HLL solver proposed by Harten et al. (1983) is based on the assumption of a two-waves structure of solution of the Riemann problem. Considering S_{L} and S_{R} the highest and the lowest wave speeds at the interface, the solution of the Riemann problem 3.40 is given by three constant states:

$$U(x,t) = \begin{cases} U_{\mathrm{L}} & \text{if } x < S_{\mathrm{L}}t \\ U_{*} & \text{if } S_{\mathrm{L}}t \leq x \leq S_{\mathrm{R}}t \\ U_{\mathrm{R}} & \text{if } x > S_{\mathrm{R}}t \end{cases} \tag{3.41}$$

where the value of the conservative variable in the region between the two waves (the star region) is considered to be the volume-average of U on the interval $[S_{\mathrm{L}}t, S_{\mathrm{R}}t]$:

$$U_{*} = \frac{1}{(S_{\mathrm{R}} - S_{\mathrm{L}})t} \int_{S_{\mathrm{L}}t}^{S_{\mathrm{R}}t} U(x,t)\, dx \tag{3.42}$$

From the Euler equations in integral conservative form it is found:

$$U_{*} = \frac{S_{\mathrm{R}}U_{\mathrm{R}} - S_{\mathrm{L}}U_{\mathrm{L}} - (\Phi_{\mathrm{R}} - \Phi_{\mathrm{L}})}{S_{\mathrm{R}} - S_{\mathrm{L}}} \tag{3.43}$$

where $\Phi_{\mathrm{L}} = \Phi(U_{\mathrm{L}})$ and $\Phi_{\mathrm{R}} = \Phi(U_{\mathrm{R}})$. The corresponding flux can now be written:

$$\Phi_{i\pm1/2} = \begin{cases} \Phi_{\mathrm{L}} & \text{if } 0 < S_{\mathrm{L}} \\ \Phi_{*} & \text{if } S_{\mathrm{L}} \leq 0 \leq S_{\mathrm{R}} \\ \Phi_{\mathrm{R}} & \text{if } 0 > S_{\mathrm{R}} \end{cases} \tag{3.44}$$

where the quantity Φ_* is obtained by applying the integral conservation equations on the domain $[S_{\mathrm{L}}t, 0]$ and considering $U = U_*$:

$$\Phi_* = \frac{S_{\mathrm{R}}\Phi_{\mathrm{L}} - S_{\mathrm{L}}\Phi_{\mathrm{R}} + S_{\mathrm{L}}S_{\mathrm{R}}(U_{\mathrm{R}} - U_{\mathrm{L}})}{S_{\mathrm{R}} - S_{\mathrm{L}}} \tag{3.45}$$

The wave speeds S_{L} and S_{R} can be estimated as function of the primitive variables at the faces (Davis (1988)):

$$S_{\mathrm{L}} = \min(\lambda_{1\mathrm{L}}, \lambda_{1\mathrm{R}}),\ S_{\mathrm{R}} = \max(\lambda_{3\mathrm{L}}, \lambda_{3\mathrm{R}}) \tag{3.46}$$

where $\lambda_{1\mathrm{L}}, \lambda_{3\mathrm{L}}, \lambda_{1\mathrm{R}}, \lambda_{3\mathrm{R}}$ are the minimum and maximum eigenvalues of the Euler system of equations evaluated at the left and right sides of the interface according to the equation 3.19:

$$\lambda_{1\mathrm{L}} = u_{\mathrm{L}} - a_{\mathrm{L}},\ \lambda_{3\mathrm{L}} = u_{\mathrm{L}} + a_{\mathrm{L}},\ \lambda_{1\mathrm{R}} = u_{\mathrm{R}} - a_{\mathrm{R}},\ \lambda_{3\mathrm{R}} = u_{\mathrm{R}} + a_{\mathrm{R}} \tag{3.47}$$

The main draw-back of the HLL solver is the absence of wave speeds related to the second eigenvalue of the one-dimensional conservation equations. As a result, this method cannot reproduce correctly contact waves and interfaces between different phases when the method is applied for solving the conservation laws of multi-component flows.

3.4.2 The HLLC solver

The HLLC solver represents an improved version of the HLL solver proposed by Toro (1999), in which a new wave speed corresponding to the contact wave is considered. Thus, the wave structure of the solution is defined by three waves separating four constant states:

$$U(x,t) = \begin{cases} U_{\mathrm{L}} & \text{if } x < S_{\mathrm{L}}t \\ U_{*\mathrm{L}} & \text{if } S_{\mathrm{L}}t \leq x \leq S_*t \\ U_{*\mathrm{R}} & \text{if } S_* \leq x \leq S_{\mathrm{R}}t \\ U_{\mathrm{R}} & \text{if } x > S_{\mathrm{R}}t \end{cases} \tag{3.48}$$

where S_* is the contact wave speed. The corresponding flux can be written:

$$\Phi_{i\pm1/2} = \begin{cases} \Phi_{\mathrm{L}} & \text{if } 0 < S_{\mathrm{L}} \\ \Phi_{*\mathrm{L}} & \text{if } S_{\mathrm{L}} \leq 0 \leq S_{*\mathrm{L}} \\ \Phi_{*\mathrm{R}} & \text{if } S_{*\mathrm{L}} \leq 0 \leq S_{*\mathrm{R}} \\ \Phi_{\mathrm{R}} & \text{if } 0 > S_{\mathrm{R}} \end{cases} \tag{3.49}$$

where $\Phi_{*\mathrm{R}}, \Phi_{*\mathrm{L}}$ are the fluxes corresponding to the star region. Integrating the Euler equations over appropriate control volumes the following relations are obtained:

$$\begin{aligned} \Phi_{*\mathrm{L}} - \Phi_{\mathrm{L}} &= S_{\mathrm{L}}(U_{*\mathrm{L}} - U_{\mathrm{L}}) \\ \Phi_{*\mathrm{R}} - \Phi_{*\mathrm{L}} &= S_{*}(U_{*\mathrm{R}} - U_{*\mathrm{L}}) \\ \Phi_{\mathrm{R}} - \Phi_{*\mathrm{R}} &= S_{\mathrm{R}}(U_{\mathrm{R}} - U_{*\mathrm{R}}) \end{aligned} \tag{3.50}$$

According to the exact solution of the Riemann problem applied to the Euler equations, only the density and the tangential velocity can be discontinuous across a contact wave and the following relations are true:

$$\begin{aligned} p_{*\mathrm{L}} &= p_{*\mathrm{R}} = p_{*} \\ u_{*\mathrm{L}} &= u_{*\mathrm{R}} = S_{*} \end{aligned} \tag{3.51}$$

The contact wave speed S_* pressure corresponding to the star region p_* are found by combining the equations 3.50 and 3.51:

$$p_* = p_{\mathrm{L}} + \rho_{\mathrm{L}}(S_{\mathrm{L}} - u_{\mathrm{L}})(S_* - u_{\mathrm{L}}) = p_{\mathrm{R}} + \rho_{\mathrm{R}}(S_{\mathrm{R}} - u_{\mathrm{R}})(S_* - u_{\mathrm{R}}) \tag{3.52}$$

$$S_* = \frac{p_{\mathrm{R}} - p_{\mathrm{L}} + \rho_{\mathrm{L}} u_{\mathrm{L}}(S_{\mathrm{L}} - u_{\mathrm{L}}) - \rho_{\mathrm{R}} u_{\mathrm{R}}(S_{\mathrm{R}} - u_{\mathrm{R}})}{\rho_{\mathrm{L}}(S_{\mathrm{L}} - u_{\mathrm{L}}) - \rho_{\mathrm{R}}(S_{\mathrm{R}} - u_{\mathrm{R}})} \tag{3.53}$$

and the conservative variables in the star region are found from the equations 3.50 - 3.52:

$$U_{*\mathrm{L}} = \rho_{\mathrm{L}} \frac{S_{\mathrm{L}} - u_{\mathrm{L}}}{S_{\mathrm{L}} - S_*} \begin{bmatrix} 1 \\ S_* \\ \hat{H}_{*\mathrm{L}} \end{bmatrix}, \; U_{*\mathrm{R}} = \rho_{\mathrm{R}} \frac{S_{\mathrm{R}} - u_{\mathrm{R}}}{S_{\mathrm{R}} - S_*} \begin{bmatrix} 1 \\ S_* \\ \hat{H}_{*\mathrm{R}} \end{bmatrix} \tag{3.54}$$

where:

$$\begin{aligned}\hat{H}_{*\mathrm{L}} &= E_{\mathrm{L}} + (S_* - u_{\mathrm{L}})\left(S_* + \frac{p_{\mathrm{L}}}{\rho_{\mathrm{L}}(S_* - u_{\mathrm{L}})}\right)\\ \hat{H}_{*\mathrm{R}} &= E_{\mathrm{R}} + (S_* - u_{\mathrm{R}})\left(S_* + \frac{p_{\mathrm{R}}}{\rho_{\mathrm{R}}(S_* - u_{\mathrm{R}})}\right)\end{aligned} \tag{3.55}$$

The equations 3.50, 3.53, 3.54 and 3.55 allow the computation of the fluxes $\Phi_{*\mathrm{L}}$ and $\Phi_{*\mathrm{R}}$ in the star region and thus the approximate HLLC solution is complete.

3.5 MUSCL reconstruction schemes

As already mentioned, higher orders of spatial accuracy for the finite volume methods can be achieved by reconstructing the values of the conservative (or primitive) variables at the faces of the finite volumes as functions of the volume-averaged values assigned to the centres of the finite volumes. The most used methods are the Monotone Upstream-centred Schemes for Conservation Laws (MUSCL) family of methods.

The simplest MUSCL scheme is the MinMod extrapolation introduced by Van Leer. Considering the one-dimensional case, the MinMod scheme approximates the conservative variable U at the right interface of the finite volume $\Omega_i = [x_{i-1/2}, x_{i+1/2}]$ as:

$$U_{\mathrm{L}} = U_i + \left.\frac{\partial U}{\partial x}\right|_i^{\mathrm{MinMod}} (x_{i+1/2} - x_i) \tag{3.56}$$

$$U_{\mathrm{R}} = U_{i+1} + \left.\frac{\partial U}{\partial x}\right|_{i+1}^{\mathrm{MinMod}} (x_{i+1/2} - x_{i+1}) \tag{3.57}$$

where the MinMod gradients are defined as:

$$\left.\frac{\partial U}{\partial x}\right|_i^{\mathrm{MinMod}} = \min\left(\left|\frac{U_{i+1} - U_i}{x_{i+1} - x_i}\right|, \left|\frac{U_i - U_{i-1}}{x_i - x_{i-1}}\right|\right) \mathrm{sign}(U_{i+1} - U_{i-1}) \tag{3.58}$$

$$\left.\frac{\partial U}{\partial x}\right|_{i+1}^{\mathrm{MinMod}} = \min\left(\left|\frac{U_{i+2} - U_{i+1}}{x_{i+2} - x_{i+1}}\right|, \left|\frac{U_{i+1} - U_i}{x_{i+1} - x_i}\right|\right) \mathrm{sign}(U_{i+2} - U_i) \tag{3.59}$$

The values U_{L} and U_{R} at the left interface are extrapolated in a similar way, but starting from the values of U in the centres of the finite volumes Ω_{i-1} and Ω_i. The symmetric version of the MinMod scheme of Roe (1986) cancels the MinMod gra-

MUSCL scheme	Accuracy order	β	$l(r)$
Van Leer (1977) (MinMod)	2	-1	$\min(1, r)$
Roe (1986) (MinMod-symmetric)	2	-1	$\max(0, \min(1, r))$
Van Leer (1977)	2	-1	$2r/(1+r)$
G.Van Albada et al. (1982)	2	-1	$r(1+r)/(1+r^2)$
Roe (1986) (SuperBee)	2	-1	$\max(0, \min(1, 2r), \min(2, r))$
Zoltak and Drikakis (1998)	3	$1/3$	$1 - \left(1 + \frac{4r}{1+r^2}\right)\left(1 - \frac{4r}{1+r^2}\right)^2$

Table 3.1: MUSCL schemes parameters

dient if the variable U is not monotonic across the three finite volumes considered. The MinMod scheme is second order accurate in space. Improved MUSCL schemes of the same or higher orders of accuracy have been developed by different authors, such as Van Leer (1977), G.Van Albada et al. (1982), Zoltak and Drikakis (1998), Roe (1986). They can be described by the following generic expressions for the values U_{L} and U_{R} at the right interface of the finite volume Ω_i:

$$U_{\mathrm{L}} = U_i + \frac{1-\beta}{4} l(r_{\mathrm{L}})(U_i - U_{i-1}) + \frac{1+\beta}{4} l\left(\frac{1}{r_{\mathrm{L}}}\right)(U_{i+1} - Ui) \tag{3.60}$$

$$U_{\mathrm{R}} = U_i - \frac{1-\beta}{4} l(r_{\mathrm{R}})(U_i - U_{i-1}) - \frac{1+\beta}{4} l\left(\frac{1}{r_{\mathrm{R}}}\right)(U_{i+1} - Ui) \tag{3.61}$$

where:

$$r_{\mathrm{L}} = \frac{U_{i+1} - U_i}{U_i - U_{i-1}},\ r_{\mathrm{R}} = \frac{U_{i+1} - U_i}{U_{i+2} - U_{i+1}} \tag{3.62}$$

and the constant β and the form of the function l are given in the table 3.5

3.6 Runge-Kutta schemes for ordinary differential equations

Considering that all the sources and fluxes are known, the system of transport equations is reduced to the simple form:

$$\frac{d\bar{U}_i(t)}{dt} = Y(U_i(t)),\ i = 1, ..N_{\mathrm{FV}} \tag{3.63}$$

for each of the finite volume Ω_i, as discussed in 3.2. This is an ordinary differential equation (first order) with one initial condition of the form:

$$U_i(t=0) = U_{0,i},\ i = 1, ..N_{\text{FV}} \tag{3.64}$$

and can be easily solved with some explicit integration methods. The simplest explicit integration scheme is the Euler scheme, of first order of accuracy, described by the time-advancing procedure:

$$U_i^{[N+1]} = U_i^{[N]} + \Delta t^{[N+1]} Y_i^{[N]},\ i = 1, ..N_{\text{FV}} \tag{3.65}$$

where the superscript $[N]$ represents the time step index, $\Delta t^{[N+1]} = t^{[N+1]} - t^{[N]}$ is the time step size, and $U_i^{[N]} = U_i(t^{[N]}), Y_i^{[N]} = Y(U_i(t^{[N]}))$.
For higher orders of accuracy, the most used methods are the Runge-Kutta schemes, after being introduced in the framework of the finite volume methods by Jameson (1983). For an arbitrary order of accuracy N_{RK}, the time advancing procedure is given by the following algorithm (the subscript i representing the finite volume is omitted):

$$\begin{aligned}
&U^{*[0]} = U^{[N]} \\
&\\
&U^{*[1]} = U^{*[0]} + \tfrac{1}{N_{\text{RK}}-1+1}\Delta t Y(U^{*[0]}) \\
&U^{*[2]} = U^{*[0]} + \tfrac{1}{N_{\text{RK}}-2+1}\Delta t Y(U^{*[1]}) \\
&\dots \\
&U^{*[N_{\text{RK}}]} = U^{*[0]} + \tfrac{1}{N_{\text{RK}}-N_{\text{RK}}+1}\Delta t Y(U^{*[N_{\text{RK}}-1]}) \\
&\\
&U^{[N+1]} = U^{*[N_{\text{RK}}]}
\end{aligned} \tag{3.66}$$

Thus, the Runge-Kutta methods presented above requires an iterative procedure at each time step advancement, the number of necessary iterations is equal to the accuracy of the scheme. Other explicit time-integration schemes have been derived starting from the Runge-Kutta method, such as the TVD enforcing scheme of Gottlieb and Shu. (1998) and the extended stability schemes developed by Spiteri and Ruuth (2002).

3.7 Concluding remarks

The transport equations of the $K - L$ and $K - \epsilon$ models presented in the previous chapter will be solved using a finite volume numerical framework. A Runge-Kutta type explicit method is used for time integration. The HLL and HLLC approximate Riemann solvers are used for the convective terms, together with MUSCL reconstruction schemes. It is considered that the additional variables F, K, L and ϵ do not change the structure of the solution for the Riemann problem at the cell interfaces and they will be passively advected. The derivatives present in the additional turbulence terms, such as diffusions and sources, are discretized with the central difference scheme. For generality, the spatial discretization methods are implemented in curvilinear coordinates, as shown in Drikakis and Rider (2005).

Chapter 4

Results

The performance of the $K-L$ and $K-\epsilon$ turbulence models is tested for three test cases involving turbulent mixing by the Rayleigh-Taylor and Richtmyer-Meshkov instabilities. The first test case represents the classical RTI problem, with a heavy fluid being accelerated by the gravity against a lighter fluid. At late times, a self similar state should be obtained, with the instability growth rate of the form $\eta \sim \alpha t^2$, as mentioned in section 1.1. The second test case represents the basic Richtmyer-Meshkov instability, occurring when a plane interface between two fluids is impulsively accelerated by a shock wave. Again the turbulence models should give a self similar evolution of the perturbation at late times, with the growth rate of the form $\eta \sim t^{\theta}$, as discussed in 1.2. The third test case is the double-planar RMI problem, involving a more complicated flow development, with multiple reflections of the shocks from the walls and from the two planar interfaces. The amplification of the perturbation is produced in this case not only by the shock-interface interaction, but also by the gradual acceleration of the fluid, where the pressure gradient opposes the density gradient. Therefore, this last problem represents an important test of the capabilities of the two models of accurately simulating the turbulent mixing by both Rayleigh-Taylor and Richtmyer-Meshkov instabilities simultaneously. The results produced by the turbulence models are compared with high resolution numerical results of Youngs (2010), Thornber et al. (2010), Hahn et al. (2010) obtained with the CFD codes TURMOIL and CNS3D. The comparisons are focused

on the growth rate of the perturbation, the spatial distribution of the fluids and of the turbulence kinetic energy, but also on some integral quantities such as the total mixing, the total turbulence kinetic energy and the integral length of the mixing zone. These quantities will be defined later. The majority of the turbulence models simulations have been conducted using the third order Runge-Kutta scheme for time integration, and the HLLC solver and the third order MUSCL reconstruction scheme for spatial discretization. However, the influence of the spatial discretization method will investigated for each test case. Details regarding the numerical methods employed in the TURMOIL and CNS3D codes can be found in Youngs (1994), Thornber (2007), Thornber et al. (2010) and Hahn et al. (2010).

4.1 The Rayleigh-Taylor instability

The configuration of the Rayleigh-Taylor problems investigated in the present work is described in figure 4.1 and it is similar to the test case in Dimonte et al. (2004). The computational domain is an orthogonal hexahedrical box with the dimensions $\mathcal{L}_x \times \mathcal{L}_y \times \mathcal{L}_z = 20cm \times 10cm \times 10cm$. The gravitational acceleration g acts along x - axis and the interface between the heavy and the light fluid is in the plane $x = X_{\mathrm{I}}$. At the initial time ($t = 0$) the two fluids are to be in a adiabatic hydrostatic equilibrium, i.e. $u = v = w = 0$ and $p/\rho^{\gamma} = constant$, with the adiabatic exponent $\gamma = 5/3$ for both fluids. In this case, the initial pressure and density profiles are obtained by integrating the Euler equations:

$$p_0(x,y,z) = \begin{cases} p_{0\mathrm{I}} \left[1 + \dfrac{\gamma - 1}{\gamma} \dfrac{\rho_{0\mathrm{H}}}{p_{0\mathrm{I}}} g(x - X_{\mathrm{I}}) \right]^{\frac{\gamma}{\gamma - 1}} & \text{if } x < X_{\mathrm{I}} \\ \\ p_{0\mathrm{I}} \left[1 + \dfrac{\gamma - 1}{\gamma} \dfrac{\rho_{0\mathrm{L}}}{p_{0\mathrm{I}}} g(x - X_{\mathrm{I}}) \right]^{\frac{\gamma}{\gamma - 1}} & \text{if } x \geq X_{\mathrm{I}} \end{cases} \tag{4.1}$$

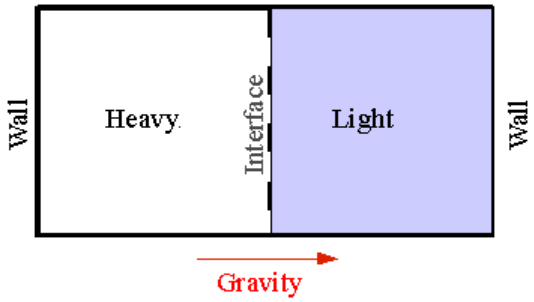

Figure 4.1: Configuration of the RTI test cases

Test case number	Initial density of the heavy fluid $\rho_{0\mathrm{H}}[g/cm^3]$	Initial density of the light fluid $\rho_{0\mathrm{L}}[g/cm^3]$	Initial Atwood number A_0	Gravitational acceleration $g[cm/s^2]$
1	1.5	1.0	0.2	5.0
2	3.0	1.0	0.5	2.0
3	7.0	1.0	0.75	1.333
4	20.0	1.0	0.905	0.105

Table 4.1: RTI test cases.

$$\rho_0(x,y,z) = \begin{cases} \rho_{0\mathrm{H}}\left[1+\dfrac{\gamma-1}{\gamma}\dfrac{\rho_{0\mathrm{H}}}{p_{0\mathrm{I}}}g(x-X_{\mathrm{I}})\right]^{\frac{1}{\gamma-1}} & \text{if } x < X_{\mathrm{I}} \\ \rho_{0\mathrm{L}}\left[1+\dfrac{\gamma-1}{\gamma}\dfrac{\rho_{0\mathrm{L}}}{p_{0\mathrm{I}}}g(x-X_{\mathrm{I}})\right]^{\frac{1}{\gamma-1}} & \text{if } x \geq X_{\mathrm{I}} \end{cases} \tag{4.2}$$

where $p_{0\mathrm{I}} = 50Pa$ is the initial pressure at the interface, and $\rho_{0\mathrm{H}}$ and $\rho_{0\mathrm{L}}$ are the initial densities of the heavy and light fluids at the interface. Three sets of values for the initial densities are considered, as presented in Table 4.1. The shape of the initial density and pressure profiles is presented in the figure 4.2.

4.1.1 Computational details

The three-dimensional ILES results (Youngs (2010)) were conducted on a grid of size $\Delta x = \mathcal{L}_x/N_{\mathrm{FV}x}$; $\Delta y = \mathcal{L}_y/N_{\mathrm{FV}y}$; $\Delta z = \mathcal{L}_z/N_{\mathrm{FV}z}$ where the numbers of finite

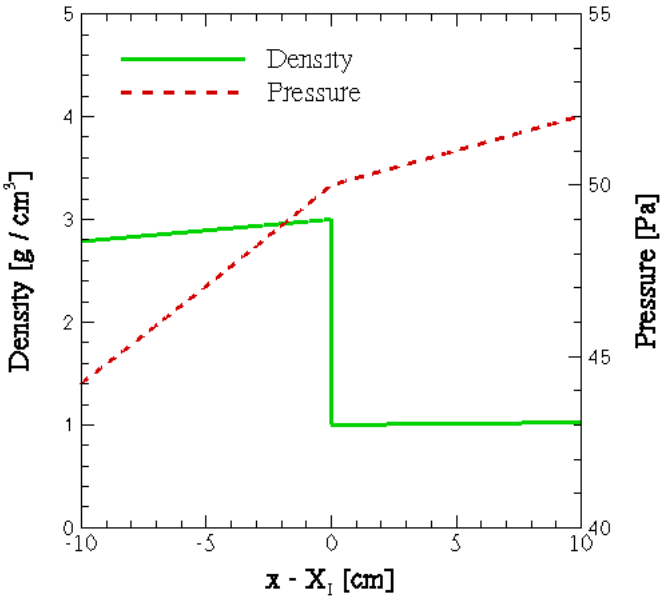

Figure 4.2: Initial conditions for the RTI test case 2

volumes on the three spatial directions are given in Table 4.2. The initial interface perturbation (at $t = 0$) is described by the power spectrum:

$$d_s = \int_{\kappa_{min}}^{\kappa_{max}} \kappa^{-}3 d\kappa \tag{4.3}$$

where d_s is the standard deviation and κ is the wave number. The values of d_s and the resulting growth rates are given in Table 4.2.

The mean flow is considered to be one-dimensional (i.e. $\partial/\partial y = \partial/\partial z = 0$) and the statistical and Favre averages of a quantity ϕ are defined as:

$$\bar{\phi} = \frac{1}{\mathcal{L}_y \mathcal{L}_z} \iint_{\mathcal{L}_y \mathcal{L}_z} \phi \, dydz \tag{4.4}$$

$$\tilde{\phi} = \frac{1}{\mathcal{L}_y \mathcal{L}_z \bar{\rho}} \iint_{\mathcal{L}_y \mathcal{L}_z} \rho\phi \, dydz \tag{4.5}$$

Therefore, the present simulations employing the $K-L$ and $K-\epsilon$ models were conducted on a one-dimensional grid of size $\Delta x = \mathcal{L}_x/N_{\mathrm{FV}x} = 20cm/1600 = 0.0125cm$. The resolution of the grid was chosen after conducting grid convergence tests (see Appendix C). Inviscid wall boundary conditions are imposed at the both ends of the computational domain. The implementation of the boundary conditions is described in Appendix A.

The turbulence models require the initial profiles for the turbulence kinetic energy, eddy size and dissipation rate. A possible approach is to initialize the turbulence model at $t = 0$, i.e. when the two fluids are separated by a sharp interface. The three turbulence quantities can be considered to be zero everywhere in the computational domain except the finite volumes adjacent to the interface. Here, the initial turbulence kinetic energy could be estimated as:

$$K_0 \sim A_0 g \eta_0 \tag{4.6}$$

where η_0 is the initial amplitude of the perturbation. The initial value of the eddy size L_0 must be proportional to the initial perturbation amplitude. Taking the initial eddy size in the vicinity of the interface of the form:

$$L_0 \sim \frac{{\eta_0}^2}{\Delta x} \tag{4.7}$$

the influence of the grid size on the initial conditions is reduced, as L_0 decreases with the width of the zone centred on the interface where the turbulence quantities are non-zero. From dimensional considerations, the initial value for the TKE dissipation can be taken:

$$\epsilon_0 \sim \frac{{K_0}^{3/2}}{L_0} \tag{4.8}$$

The above procedure has the following shortcomings: (i) it is grid dependent; (ii) the proportionality constants in equations 4.6 and 4.6 are not known. A different procedure is proposed and used in the present study. The turbulence quantities are initialized at $t_1 > 0$. If t_1 is sufficiently small, the perturbation amplitude $\eta(t_1) = \eta_1$ can be estimated by the equation 1.4 and the volume fractions of the two fluids

($f_{\mathrm{H,L}}$) inside the mixing zone ($-\eta_1 < x - X_{\mathrm{I}} < \eta_1$) can be approximated as linear functions of x:

$$\begin{aligned} f_{\mathrm{H}}(x,t_1) &= 0.5\left[1-(x-X_{\mathrm{i}})\right]/\eta_1 \\ f_{\mathrm{L}}(x,t_1) &= 0.5\left[1+(x-X_{\mathrm{i}})\right]/\eta_1 \end{aligned} \tag{4.9}$$

The density variation in the mixing zone can be also considered linear:

$$\begin{aligned} \rho_{\mathrm{H}}(x,t_1) &= 0.5\rho_{0\mathrm{H}}\left[1-(x-X_{\mathrm{i}})\right]/\eta_1 \\ \rho_{\mathrm{L}}(x,t_1) &= 0.5\rho_{0\mathrm{L}}\left[1+(x-X_{\mathrm{i}})\right]/\eta_1 \end{aligned} \tag{4.10}$$

and the mixture density is:

$$\rho(x,t_1) = \rho_{\mathrm{H}}(x,t_1) + \rho_{\mathrm{L}}(x,t_1) \tag{4.11}$$

The velocities of the two fluids $u_{\mathrm{H,L}}$ can be estimated as:

$$\begin{aligned} u_{\mathrm{H}}(x,t_1) &= f_{\mathrm{L}}(x,t_1)d\eta/dt \\ u_{\mathrm{L}}(x,t_1) &= -f_{\mathrm{H}}(x,t_1)d\eta/dt \end{aligned} \tag{4.12}$$

and the mixture velocity is the mass average of u_{H} and u_{L}:

$$u(x,t_1) = F_{\mathrm{H}}(x,t_1)u_{\mathrm{H}}(x,t_1) + F_{\mathrm{L}}(x,t_1)u_{\mathrm{L}}(x,t_1) \tag{4.13}$$

where $F_{\mathrm{H,L}}$ are the mass fractions of the two fluids. Provided that t_1 is small enough, the momentum equation can be simplified by neglecting the inertial and convective terms:

$$\frac{dp}{dx} = \rho g \tag{4.14}$$

and the pressure distribution in the mixing zone at $t = t_1$ is found by integrating the above equation:

$$p(x,t_1) = p_0 + g\left[\frac{1}{2}(\rho_{\mathrm{H}}+\rho_{\mathrm{L}})(x-X_{\mathrm{I}}) + \frac{1}{4\eta_1}(\rho_{\mathrm{H}}-\rho_{\mathrm{L}})(x-X_{\mathrm{I}})^2\right] \tag{4.15}$$

The turbulence kinetic energy should be maximum in the centre of the mixing zone (i.e. where $f_{\mathrm{H}} = f_{\mathrm{L}} = 0.5$). Therefore a good approximation of the TKE profile is

the parabolic function:

$$K(x,t_1) = 4K_{1max} f_{\mathrm{H}}(x,t_1) f_{\mathrm{L}}(x,t_1) \tag{4.16}$$

where K_{1max} is the maximum value of the turbulence kinetic energy at $t = t_1$. Its estimation is based on the fact that half of the variation of the total potential energy is transformed into TKE (the other half is dissipated):

$$\mathcal{K}(t_1) = \frac{1}{2}[\mathcal{E}_{\mathrm{p}}(t_1) - \mathcal{E}_{\mathrm{p}}(t_0)] \tag{4.17}$$

where $\mathcal{K}$ is the total turbulence kinetic energy:

$$\mathcal{K} = \int_{\Omega} \rho K d\mathcal{V} \tag{4.18}$$

and $\mathcal{E}_{\mathrm{p}}$ is the total potential energy:

$$\mathcal{E}_{\mathrm{p}} = \int_{\Omega} \rho g x d\mathcal{V} \tag{4.19}$$

After integrating and substituting it is found:

$$K_{1max} = \frac{1}{8} A_0 g \eta_1 \tag{4.20}$$

The eddy size L inside the mixing zone has also a parabolic profile with the maximum value L_{1max} at the centre of the mixing zone:

$$L(x,t_1) = 4L_{1max} f_{\mathrm{H}}(x,t_1) f_{\mathrm{L}}(x,t_1) \tag{4.21}$$

According to Gauthier and Bonnet (2000), the initial value of the dissipation rate is taken:

$$\epsilon(x,t_1) = 0.164 \frac{K(x,t_1)^{3/2}}{L(x,t_1)} \tag{4.22}$$

Finally, for the four test cases, the initialization time is taken $t_1 = 1s$, the initial perturbation amplitude is considered $\eta_0 = s_{\mathrm{d}}$ and the maximum eddy size at $t = t_1$

Test case number	Grid size for ILES simulations $N_{\mathrm{FV}x} \times N_{\mathrm{FV}y} \times N_{\mathrm{FV}z}$	Standard deviation of initial perturbation (ILES) d_{s}	RTI growth rate (ILES) α
1	$1050 \times 1000 \times 1000$	0.0025	0.055
2	$1200 \times 1000 \times 1000$	0.0025	0.054
3	$1350 \times 1000 \times 1000$	0.0025	0.060
4	$1550 \times 1000 \times 1000$	0.0025	0.070

Table 4.2: Details regarding the numerical computations of Youngs (2010).

is $L_{1max} = \eta_1$.

The main coefficients in the $K - L$ and $K - \epsilon$ turbulence models are as given in tables 2.7.4 and 2.8.4 respectively. In addition, the coefficients scaling the turbulent mass diffusion and the dissipation source in the $K - \epsilon$ model are taken respectively $\sigma_\rho = 0.25$ and $C_{\epsilon 0} = 1.05$.

4.1.2 The growth rate of the perturbation

The amplitude of the perturbation is estimated by the positions of the bubbles (x_{B}) and spikes (x_{S}). The turbulence models can offer information regarding only the cross-section average of the quantities, and therefore the bubble and spike positions are defined here as the x-locations where the average volume fraction of the heavy fluid $\tilde{f}$ is 0.01 and 0.99, respectively. At late times, when the flow is self-similar, it is expected $\eta \approx \alpha A_0 g t^2$, as mentioned in Section 1.1. A parameter estimating the overlapping of the two fluids is the integral length of the mixing zone introduced by Andrews and Spalding (1990):

$$\mathcal{W} = \int_{\mathcal{L}_x} \bar{\rho} \tilde{F} \left(1 - \tilde{F}\right) \, dx \tag{4.23}$$

From the LEM experiments of Dimonte and Schneider (2000) it is found $W/\eta \simeq 1/3$ for low Atwood numbers. The evolution of the instability obtained with the $K - L$ and $K - \epsilon$ turbulence models is presented in Figures 4.3-4.4. The plots show the variation in time of the amplitude $\eta_{\mathrm{B,S}}$ and of the integral length of the mixing zone

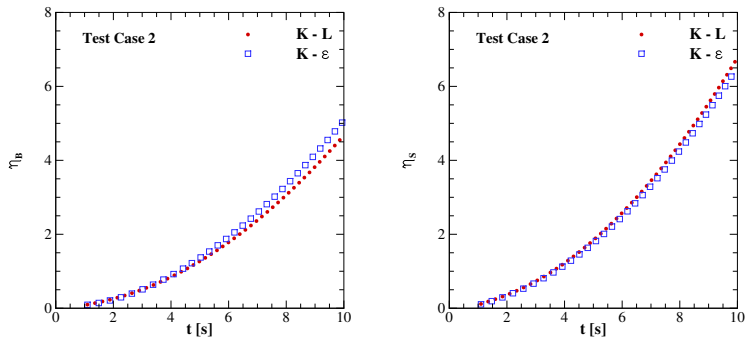

Figure 4.3: The perturbation amplitude $\eta_{B,S}$ for Test Case 2 (left: bubbles; right: spikes).

$\mathcal{W}$. The coefficients $\alpha_{B,Ss}$ are calculated as:

$$\alpha_{B,S} = \frac{1}{A_0 g}\frac{d\eta_{B,S}}{dt} \tag{4.24}$$

where the derivative $d\eta_{B,S}/dt$ is estimated using a second order central difference scheme:

$$\frac{d\eta_{B,S}}{dt} = \frac{\eta_{B,S}(t+\Delta t) - \eta_{B,S}(t-\Delta t)}{2\Delta t} \tag{4.25}$$

with $\Delta t = 10^{-4}s$.

The evolution of $\alpha_{B,S}$ is shown in Figure 4.5 for the Test Case 2. The average values of the late time $\alpha_{B,S}$ are calculated as:

$$\bar{\alpha}_{B,S} = \frac{\sum_i \alpha_{B,S,i}\Delta t}{t_{max} - t_{min}} \tag{4.26}$$

and presented together with the ratio and of the ratio $\mathcal{W}/\eta$ in Table 4.3 for all the test cases, showing reasonable agreement with the computational results of Youngs (2010) and Andrews and Spalding (1990). The averaging of $\alpha_{B,S}$ is taken over the interval $[t_{min}, t_{max}] = [2.0s,\ 10.0s]$. The Appendix B contains the plots of $\alpha_{B,S}$ $vs.$ time for the test cases 1,3, and 4.

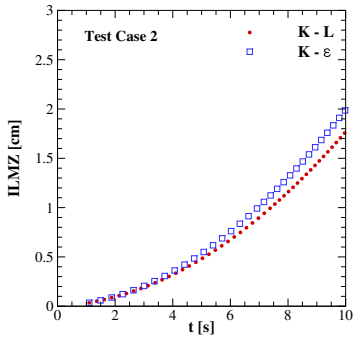

Figure 4.4: The integral length of the mixing zone $\mathcal{W}$ for Test Case 2.

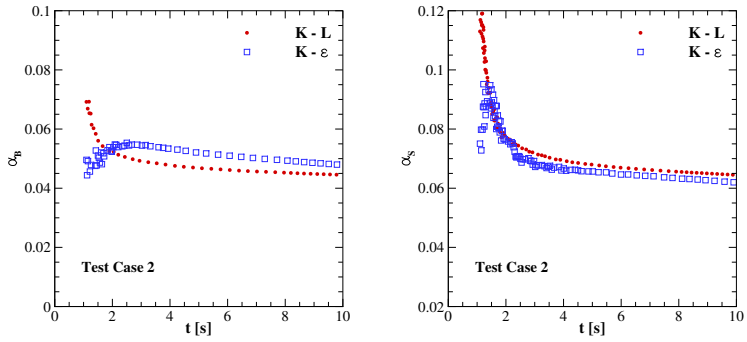

Figure 4.5: The RTI growth rate parameter $\alpha_{B,S}$ for Test Case 2 (left: bubbles; right: spikes).

Test	$\bar{\alpha}_B$		$\bar{\alpha}_S$		$\mathcal{W}/\eta$	
case	$K-L$	$K-\epsilon$	$K-L$	$K-\epsilon$	$K-L$	$K-\epsilon$
1	0.052	0.049	0.071	0.069	0.35	0.34
2	0.053	0.052	0.069	0.068	0.34	0.34
3	0.059	0.058	0.065	0.065	0.34	0.32
4	0.061	0.059	0.080	0.090	0.32	0.30

Table 4.3: Main results regarding the instability growth rate obtained with the $K-L$ and $K-\epsilon$ turbulence models.

4.1.3 Volume fraction and turbulence kinetic energy profiles

The spatial distribution of the two fluids at a given time can be described by the average volume fraction $\tilde{f}$. The profiles of the heavy fluid volume fraction at $t = 2s$ are given in Figure 4.6. The results obtained with the turbulence models are in good agreement with the ILES results of Youngs (2010). The profiles are almost symmetric and linear for the two RTI test cases, as expected for low initial Atwood number configurations. The Figure 4.7 present the distribution on the x-direction of the turbulence kinetic energy. The maximum value of the turbulence kinetic energy is increasing with the initial Atwood number and the peak position is shifted in the acting direction of the gravity. The self similar character of the flow at late times is preserved, as shown in Figure 4.8, representing the volume fraction distributions plotted against the x-coordinate centred in the mixing zone and normalized with respect to $\mathcal{W}$, at four time levels ($t = 2.5;\ 5.0;\ 7.5;\ 10s$). Additional plots presenting the distributions of the density, pressure, velocity and mass fraction for all the test cases are included in Appendix B.

4.1.4 Influence of the numerical schemes

The results regarding the Rayleigh-Taylor instability presented in the previous sections (4.1.2 and 4.1.2) have been obtained using the approximate HLLC solver for the Riemann problem at the cell interfaces and the MinMod reconstruction scheme of Van Leer. The time integration was conducted using the third order Runge-Kutta scheme. The influence of the spatial discretization method on the numerical results is investigated by increasing the accuracy of the MUSCL scheme to the third and

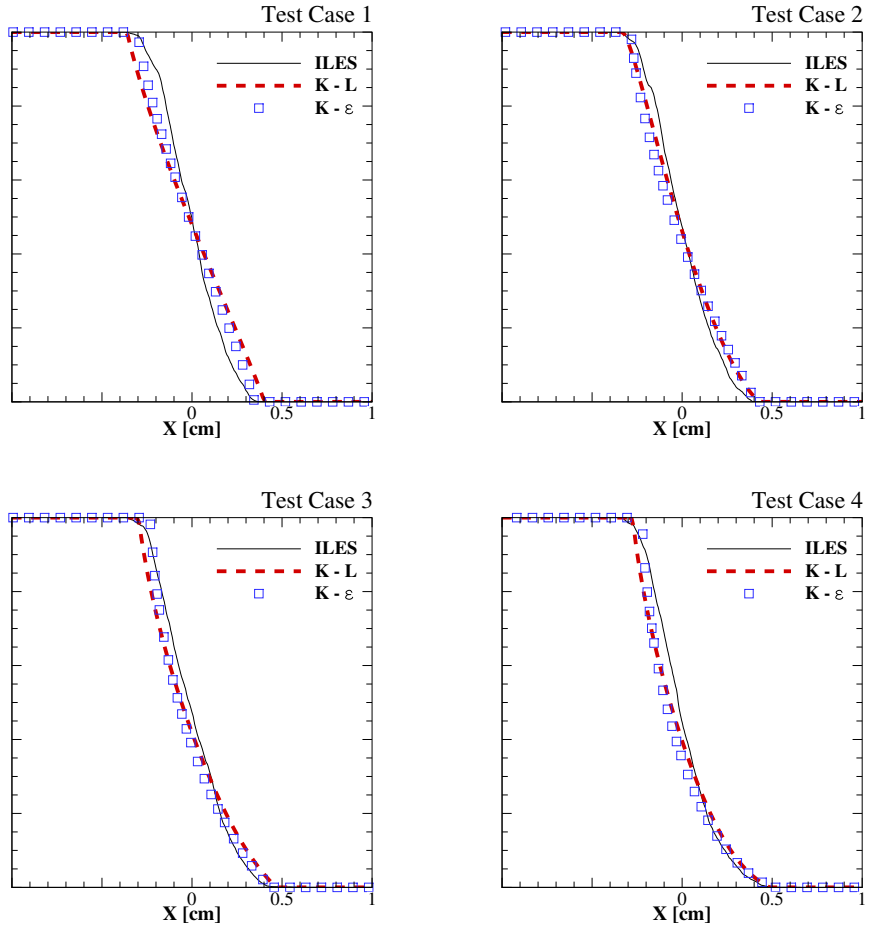

Figure 4.6: Volume fraction profiles for the four RTI test cases, at $t = 2s$. Comparison between the turbulence models and ILES results.

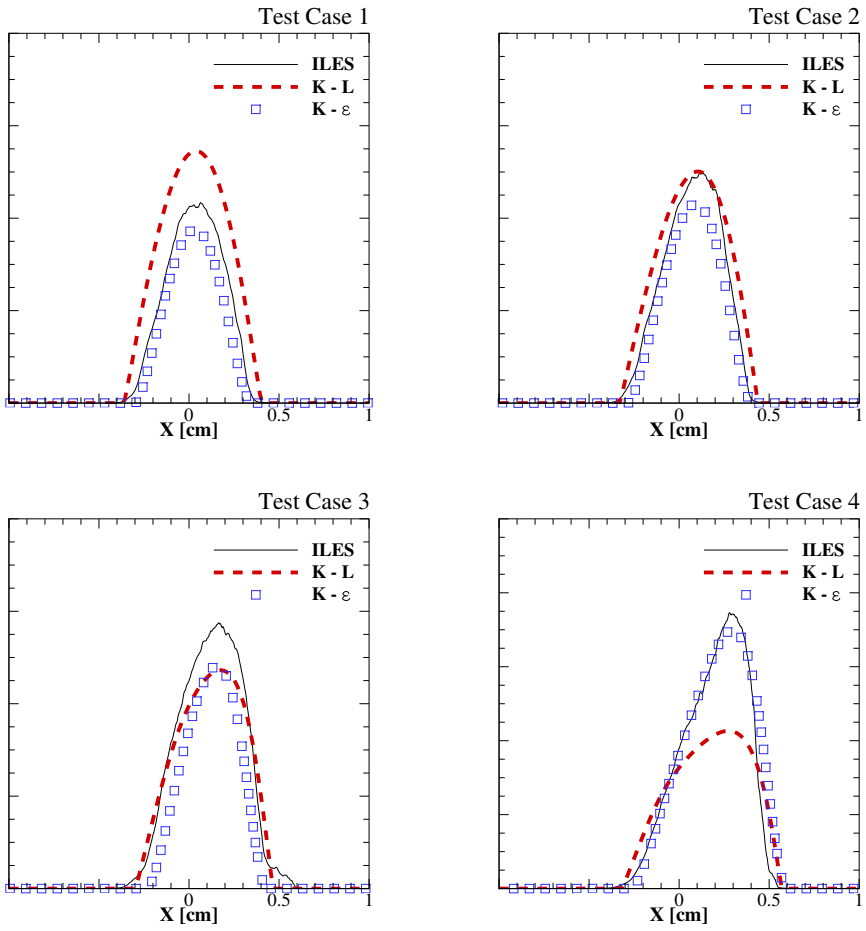

Figure 4.7: Turbulence kinetic energy profiles for the four RTI test cases, at $t = 2s$. Comparison between the turbulence models and ILES results.

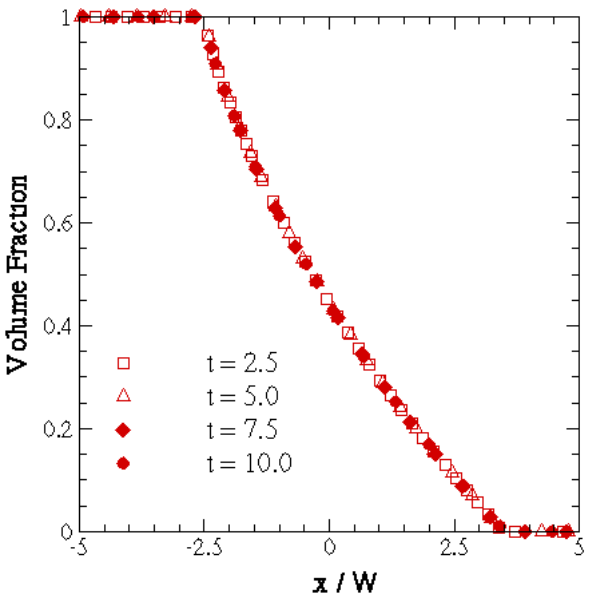

$K - L$

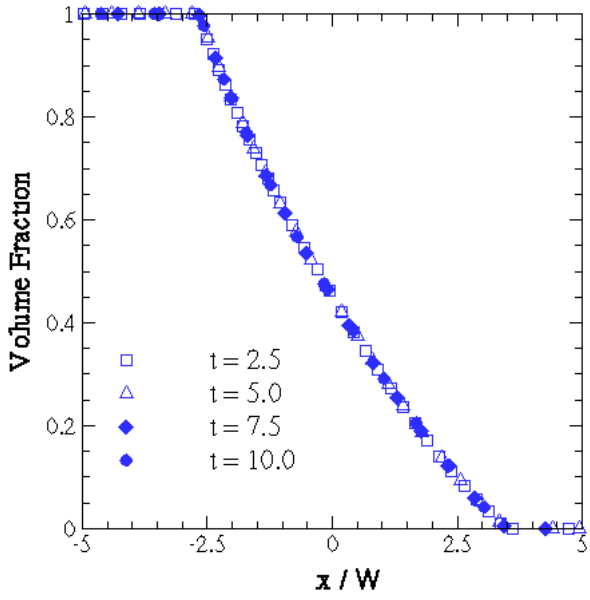

$K - \epsilon$

Figure 4.8: Volume fraction profiles at different time levels (Test case 2). Top: the $K - L$ turbulence model. Bottom: the $K - \epsilon$ turbulence model.

fifth orders (Zoltak and Drikakis (1998) and Kim and Kim (2005), respectively). Both HLL and HLLC solvers are considered. The amplitude of the perturbation η is taken as the control parameter.

Figure 4.9 presents the influence of the spatial discretization scheme on the perturbation growth for the second RTI test case (described in Table 4.1). The curves are overlapping for both $K-L$ and $K-\epsilon$ models. The values of the growth rate parameters $\alpha_{B,S}$ are presented in tables 4.4-4.7 showing no important influence of the numerics for the grid resolution employed.

Numerical	$\bar{\alpha}_B$		$\bar{\alpha}_S$	
scheme	$K-L$	$K-\epsilon$	$K-L$	$K-\epsilon$
HLL-MUSCL-1st	0.051	0.048	0.070	0.068
HLL-MUSCL-2nd	0.052	0.049	0.071	0.069
HLL-MUSCL-5th	0.052	0.049	0.071	0.069
HLLC-MUSCL-1st	0.052	0.049	0.071	0.069
HLLC-MUSCL-2nd	0.052	0.049	0.071	0.069
HLLC-MUSCL-5th	0.052	0.049	0.071	0.069

Table 4.4: The influence of the numerical schemes on the instability growth rate obtained with the $K-L$ and $K-\epsilon$ turbulence models for the Test Case 1.

Numerical	$\bar{\alpha}_B$		$\bar{\alpha}_S$	
scheme	$K-L$	$K-\epsilon$	$K-L$	$K-\epsilon$
HLL-MUSCL-1st	0.052	0.051	0.068	0.067
HLL-MUSCL-2nd	0.053	0.052	0.069	0.068
HLL-MUSCL-5th	0.053	0.052	0.069	0.068
HLLC-MUSCL-1st	0.053	0.052	0.069	0.068
HLLC-MUSCL-2nd	0.053	0.052	0.069	0.068
HLLC-MUSCL-5th	0.053	0.052	0.069	0.068

Table 4.5: The influence of the numerical schemes on the instability growth rate obtained with the $K-L$ and $K-\epsilon$ turbulence models for the Test Case 2.

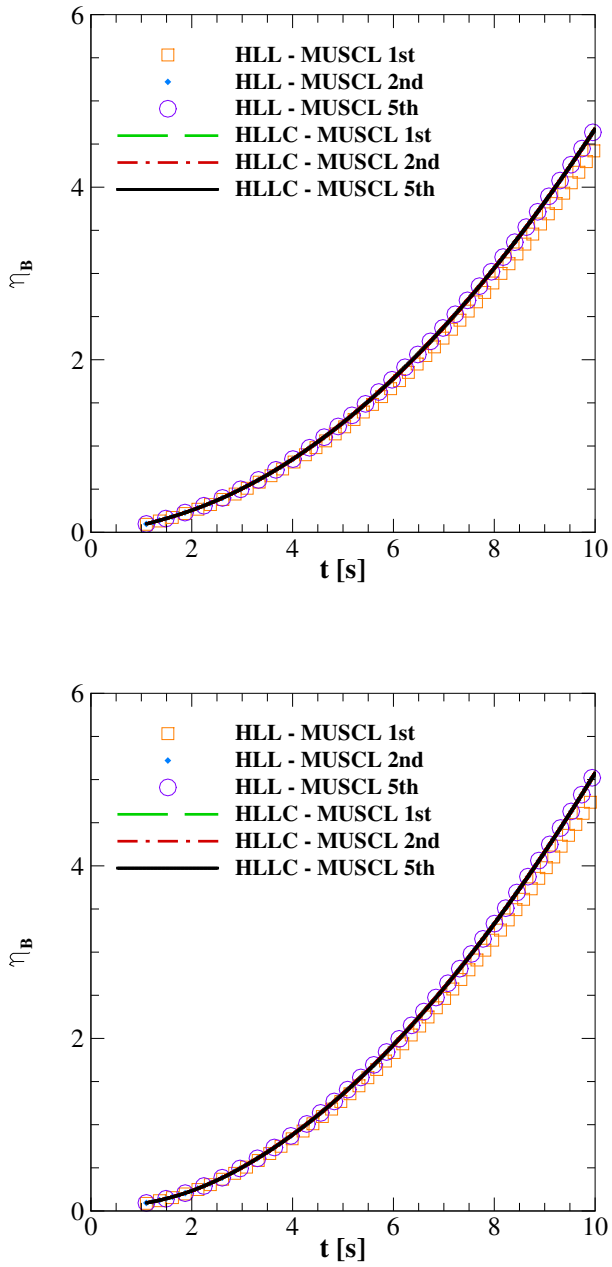

Figure 4.9: Influence of the numerical schemes on the RTI growth rate. Top: the $K - L$ turbulence model. Bottom: the $K - \epsilon$ turbulence model.

Numerical scheme	$\bar{\alpha}_{\mathrm{B}}$		$\bar{\alpha}_{\mathrm{S}}$	
	$K-L$	$K-\epsilon$	$K-L$	$K-\epsilon$
HLL-MUSCL-1st	0.057	0.057	0.064	0.063
HLL-MUSCL-2nd	0.059	0.058	0.065	0.064
HLL-MUSCL-5th	0.059	0.058	0.065	0.065
HLLC-MUSCL-1st	0.059	0.058	0.065	0.065
HLLC-MUSCL-2nd	0.059	0.058	0.065	0.065
HLLC-MUSCL-5th	0.059	0.058	0.065	0.065

Table 4.6: The influence of the numerical schemes on the instability growth rate obtained with the $K-L$ and $K-\epsilon$ turbulence models for the Test Case 3.

Numerical scheme	$\bar{\alpha}_{\mathrm{b}}$		$\bar{\alpha}_{\mathrm{s}}$	
	$K-L$	$K-\epsilon$	$K-L$	$K-\epsilon$
HLL-MUSCL-1st	0.057	0.055	0.075	0.085
HLL-MUSCL-2nd	0.058	0.058	0.077	0.087
HLL-MUSCL-5th	0.060	0.058	0.078	0.088
HLLC-MUSCL-1st	0.060	0.059	0.078	0.085
HLLC-MUSCL-2nd	0.061	0.059	0.078	0.088
HLLC-MUSCL-5th	0.061	0.059	0.080	0.090

Table 4.7: The influence of the numerical schemes on the instability growth rate obtained with the $K-L$ and $K-\epsilon$ turbulence models for the Test Case 4.

4.2 The planar Richtmyer-Meshkov instability

The planar Richtmyer-Meshkov problem investigated in the presented work is described in Figure 4.10. Two different fluids are separated by a planar interface perpendicular to the x-axis. A shock wave is generated in the heavy fluid (at the left side of the interface) and impulsively accelerates the interface and amplifies the initial perturbations, starting the RMI mixing process. The computational domain is a box of dimensions $\mathcal{L}_x \times \mathcal{L}_y \times \mathcal{L}_z = 1000 \times 2\pi \times 2\pi$ and translates on the x-direction together with the accelerated interface.

The initial conditions (density and pressure) are presented in Figure 4.17. In front of the shock, the density of the heavy fluid is $\rho_1 = 3kg/m^3$, the pressure is $p = 10^3 Pa$ and the Mach number is $M = 1.84$. The light fluid has the initial density $\rho_2 = 6.34kg/m^3$ and it is considered to be in isobaric and isothermal equilibrium with the heavy fluid. The resulting initial Atwood number is $A_0 = (\rho_2 - \rho_1)/(\rho_2 + \rho_1) = 0.5$. The specific heat ratio of is $\gamma = 5/3$ for both fluids. The initial positions of the shock wave and interface are $x_{\mathrm{S}} = 3.5m$ and $x_{\mathrm{I}} = 4.0m$ respectively. The RMI problem presented above is similar to the configuration of the numerical study of Thornber et al. (2010).

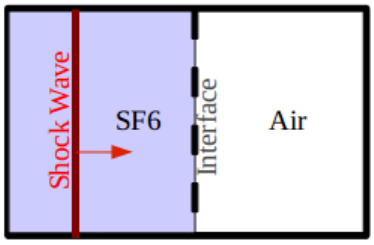

Figure 4.10: Configuration of the planar RMI test case.

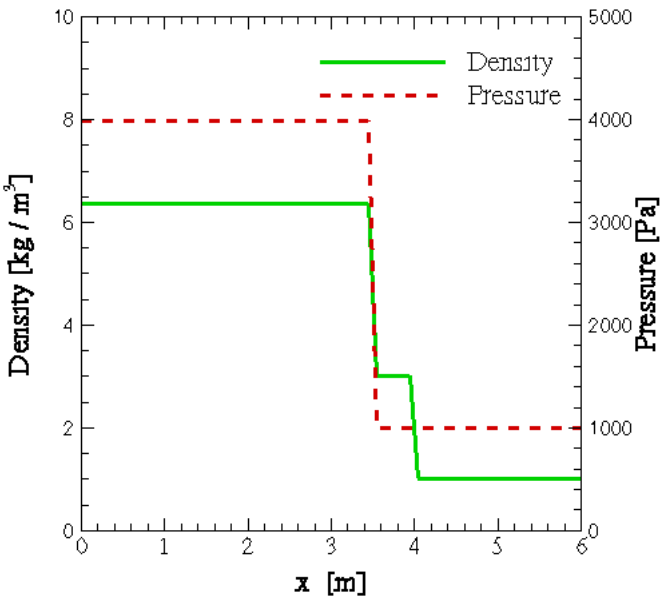

Figure 4.11: Initial conditions for the planar RMI test case.

4.2.1 Computation details

The initial direction of propagation of the planar shock wave is perpendicular to the interface, and therefore the mean flow can be considered one-dimensional. The statistical and Favre averages are defined in the previous section by the equations 4.4 and 4.5. The grid size adopted here in the x direction is $\Delta x = \mathcal{L}_x / N_{\mathrm{FV}x} = 1000m/32000 \simeq 0.03125m$ and it is slightly finer than the grid size used by Thornber et al. (2010). Permeable boundary conditions have been imposed at the both ends of the domain, as described in the Appendix A. The maximum CFL number is $N_{\mathrm{CFL}} = 0.20$.

The initial profiles of the turbulence quantities K, L and ϵ have the same shape as for the RTI simulations presented in the previous section. The estimation of the turbulence kinetic energy at the interface is based on the results of Mikaelian (1985) which estimates the total turbulence kinetic energy $\mathcal{K}$ as:

$$\mathcal{K} \simeq 0.0903 {A_0}^2 \mathcal{E}_{\mathrm{k}} \tag{4.27}$$

where the total kinetic energy of the mean flow $\mathcal{E}_\mathrm{k}$ and the total turbulence kinetic energy $\mathcal{K}$ are defined on a control volume Ω as:

$$\mathcal{E}_\mathrm{k} = \int_\Omega \bar{\rho}\frac{1}{2}\tilde{u}_i\tilde{u}_i \, d\mathcal{V} \tag{4.28}$$

$$\mathcal{K} = \int_\Omega \bar{\rho}K \, d\mathcal{V} \tag{4.29}$$

Applying the relation 4.27 on a control volume containing the interface at a very early time, the initial turbulence kinetic energy can be estimated as:

$$K_0 \simeq 0.0903{A_0}^2\frac{1}{2}\tilde{u}_i\tilde{u}_i \tag{4.30}$$

resulting for the present problem $K_0 = 0.5m^2/s^2$. The initial values for the eddy size and dissipation rate are taken $L_0 = 1.00m$ and $\epsilon_0 = 0.35m^2/s^3$.
The same model coefficients have been used as for the Rayleigh-Taylor problems (section 4.1). In addition, the distinction between gradual and impulsive accelerations is made by setting $\Lambda_\Theta = 0.25$ for both $K - L$ and $K - \epsilon$ turbulence models. The coefficient Λ_Θ was defined in section 2.7.

4.2.2 The evolution of the mixing zone

The extent of the mixing zone is characterized by the positions of the bubble ans spike (x_b and x_s) defined in the same way as for the Rayleigh-Taylor problems and by the integral width of the mixing zone defined in the previous section by equation 4.23. The amplitude of the perturbation is taken again $\eta = 0.5|x_\mathrm{b} - x_\mathrm{s}|$.
The evolution in time of the perturbation is presented in Figure 4.12. The integral width of the mixing zone is in good agreement with the ILES results of Thornber et al. (2010). Considering the perturbation amplitude η and the integral width of the mixing zone $\mathcal{W}$ of the form:

$$\eta = (\Delta U t)^\theta, \quad \mathcal{W} \sim (t - t_0)^{\theta_\mathcal{W}} \tag{4.31}$$

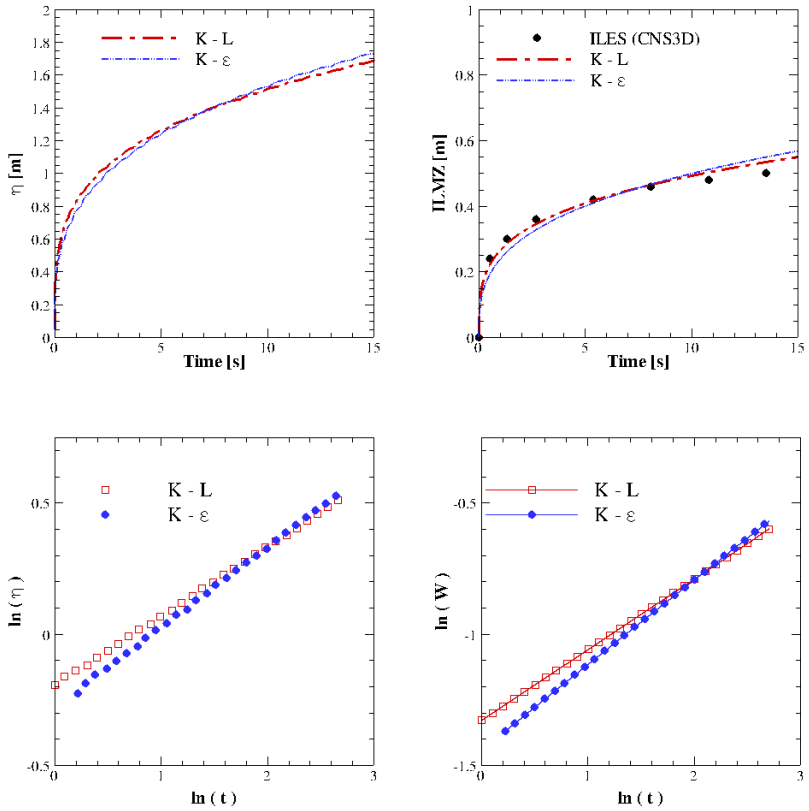

Figure 4.12: The RMI growth rate: the evolution in time of the perturbation amplitude and of the integral length of the mixing zone.

the parameters θ and $\theta_{\mathcal{W}}$ can be estimated by differentiating the above equations:

$$\theta = \frac{d(\ln h)}{d(\ln t)}, \quad \theta_{\mathcal{W}} = \frac{d(\ln \mathcal{W})}{d(\ln t)} \tag{4.32}$$

The derivatives in the equation 4.32 were calculated using a second order central difference scheme and the values of θ were averaged over the interval [1s, 15s]. The dependency of $\ln h$ on $\ln t$ is found almost linear at late times, as shown in Figure 4.12. Thus, the parameters θ and $\theta_{\mathcal{W}}$ are constant, as expected for the self similar regime. The $K-L$ models gives $\theta \simeq \theta_{\mathcal{W}} \simeq 0.26$ and the $K-\epsilon$ models gives $\theta \simeq \theta_{\mathcal{W}} \simeq 0.27$. Both values are slightly larger than $\theta_{\mathcal{W}} \simeq 0.235$ found by Thornber et al. (2010).

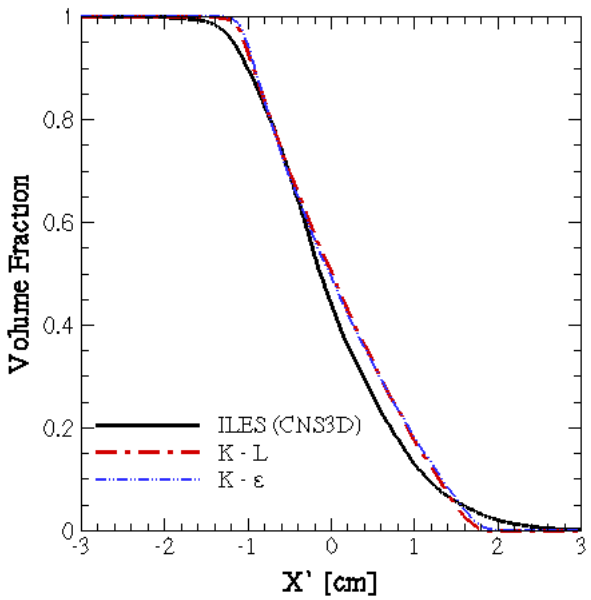

Figure 4.13: Volume fraction profiles at $t = 10$. Comparison with ILES results.

The distribution of the two fluids in the mixing zone is presented in Figure 4.13, where the average volume fraction of the heavy fluid is plotted at $t = 10$ against the coordinate $x' = -x_{\text{MZ}}$, where x_{MZ} represents the coordinate of the centre mixing zone, defined as the x-location where the average volume fraction is $\tilde{f} = 0.5$.. The two turbulence models are in good agreement with each other, but show slightly more diffusion of the volume fraction than found by the ILES computations of Thornber et al. (2010). Figure 4.14 presents the volume fraction profiles at different times ($t = 5.0; 8.0; 10.0; 13.0$), plotted against the normalized coordinate $x'' = (x - x_{\text{MZ}})/\mathcal{W}$. The good collapsing of all the curves proves again that both turbulence models preserve the self similarity of the Richtmyer-Meshkov instability at late times.

4.2.3 Influence of the numerical schemes

In order to investigate the effects of the numerics on the results, the planar RMI problem was numerically resolved using the HLL and HLLC approximate Rie-

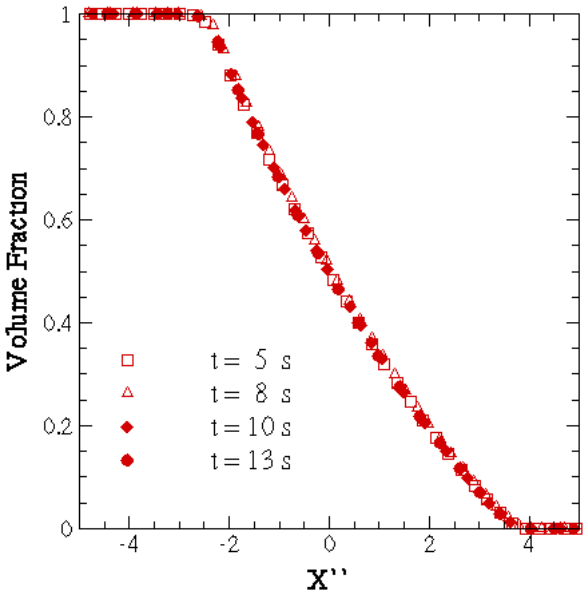

$K - L$

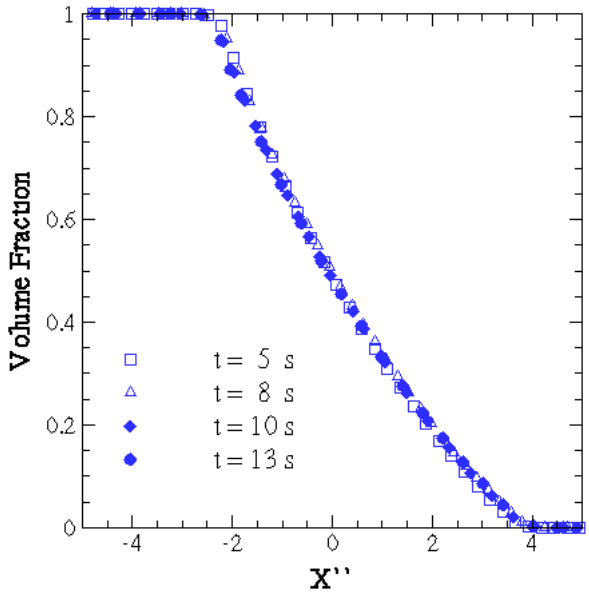

$K - \epsilon$

Figure 4.14: Volume fraction profiles at different time levels.

mann solvers, and MUSCL reconstruction schemes of second, third and fifth orders. The control parameter is again the amplitude of the perturbation η.
Figure 4.15 shows that the HLL solver in combination with the second order MUSCL scheme produces a highly diffusive solution at early times probably as a result of the inaccurate simulation of the shock-interface interaction. The growth rate at late times is increasing with the order of accuracy of the reconstruction scheme, for both HLL and HLLC solvers. In general, the HLL solver exhibits a higher growth rate for both turbulence models. The collapsing of the curves in Figure 4.15 suggests that the HLLC solver combined with a reconstruction scheme of third or higher order of accuracy would be appropriate for solving RMI problems.

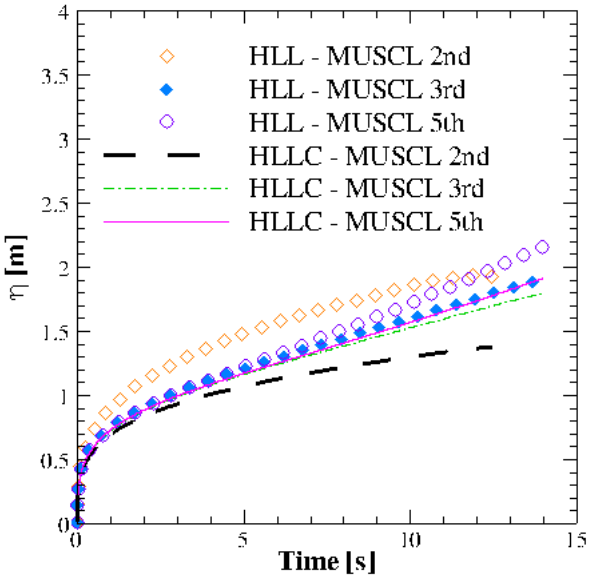

$K - L$

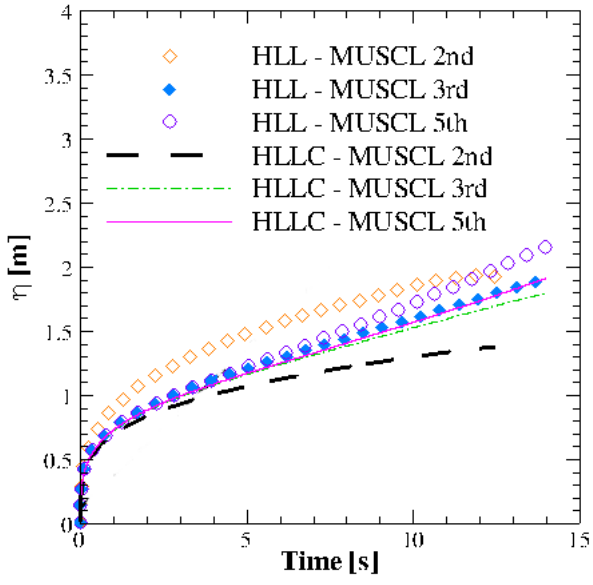

$K - \epsilon$

Figure 4.15: Influence of the numerical schemes on the RMI growth rate. Left: the $K - L$ turbulence model. Right: the $K - \epsilon$ turbulence model.

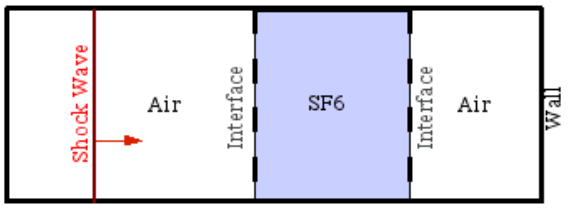

Figure 4.16: Configuration of the double planar RMI test case

4.3 The double planar Richtmyer-Meshkov instability

The configuration of the test case is described in Figure 4.16 and it is similar to the shock-tube experiment of Holder et al. (2003) and the numerical configuration of Hahn et al. (2010). A shock wave generated in air passes through a slice of sulfur hexafluoride (SF_6) delimited by two planar interfaces perpendicular to the direction of propagation. The shock wave impulsively accelerates the interfaces and amplifies their initial perturbations, starting the RMI mixing process. The mixing of the two fluids is further enhanced by the wave reflections produced by the end wall of the shock tube and by the two interfaces.

The initial conditions (density and pressure) are presented in Figure 4.17. In front of the shock, the density of the air is $\rho_1 = 1.18kg/m^3$ and the pressure is $p = 10^5 Pa$. The Mach number in front of the shock wave is $M = 1.26$. The initial density and pressure of SF_6 are $\rho_2 = 6.34kg/m^3$ and $p_2 = p_1 = 10^5 Pa$. The resulting initial Atwood number is $A_0 = (\rho_2 - \rho_1)/(\rho_2 + \rho_1) = 0.686$. The specific heat ratio of is $\gamma_1 = 1.4$ for air and $\gamma_2 = 1.076$ for SF_6. The computational domain has the dimensions $\mathcal{L}_x \times \mathcal{L}_y \times \mathcal{L}_z = 0.4m \times 0.2m \times 0.1m$. The initial positions of the shock, of the two interfaces and of the wall are respectively: $X_S = 0.03m$; $X_{I1} = 0.05m$; $X_{I2} = 0.2m$; $X_W = 0.4m$.

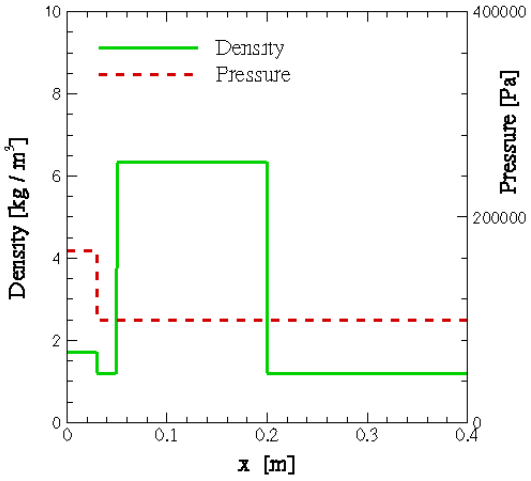

Figure 4.17: Initial conditions for the double planar RMI test case

4.3.1 Computational details

The mean flow is considered to be one-dimensional (i.e. $\tilde{v} = \tilde{w} = 0$ and $\partial/\partial y = \partial/\partial z = 0$) and the statistical and Favre averages are defined by equations 4.4 and 4.5. The one dimensional simulations are performed on $N_{\text{FV}x} = 640$ cells, giving $\Delta x = 0.000625m$, identical to the spatial resolution of Hahn et al. (2010). The maximum CFL number is $N_{\text{CFL}} = 0.20$.

The turbulence models are initialized at $t = 0.126ms$, after the initial shock wave passed through the SF_6 slice. The initial turbulence kinetic energy K_0 is directly computed from the ILES data of Hahn et al. (2010):

$$K_0(x) = \frac{1}{\bar{\rho}} \frac{1}{\mathcal{L}_y \mathcal{L}_z} \int_0^{\mathcal{L}_z} \int_0^{\mathcal{L}_y} \rho \left[(u - \tilde{u})^2 + (v - \tilde{v})^2 + (w - \tilde{w})^2 \right] \, dydz \tag{4.33}$$

The integrals in the equation 4.33 are calculated as:

$$\int_0^{\mathcal{L}_z} \int_0^{\mathcal{L}_y} \phi \, dydz = \sum_{k=1}^{N_{\text{FV}z}} \sum_{j=1}^{N_{\text{FV}y}} (\phi_{j,k} \Delta y \Delta z) \tag{4.34}$$

where j, k represent the indexes of the computational cells in the y and z directions. The initial profiles of the eddy size and dissipation rate follow the initial distribution of the turbulence kinetic energy:

$$L_0(x) = \frac{K_0(x)}{K_{0max}} L_{0max} \tag{4.35}$$

$$\epsilon_0(x) = \frac{K_0(x)}{K_{0max}} \epsilon_{0max} \tag{4.36}$$

where the maximum value of the turbulence kinetic energy K_{0max} is found from the ILES data, the maximum eddy size L_{0max} is equal to the extent of the mixing zone at $t = 0.126ms$ and ϵ_{0max} ensures the initial growth rate predicted by ILES. The resulting values are : $K_{0max} = 2.9m^2/s^2$, $L_{0max} = 0.0075m$ and $\epsilon_{0max} = 0.03m^2/s^3$.

4.3.2 The evolution of the instability

The growth of the Richtmyer-Meshkov instability for the double planar test case is assessed quantitatively by the total turbulence kinetic energy $\mathcal{K}$ defined in section 4.2 (equation 4.27) and by the integral length of the mixing zone, defined in section 4.1 (equation 4.23). An additional integral quantity of interest is the total mixing defined as:

$$\mathcal{M} = \int_{\Omega} \bar{\rho} \tilde{F}_1 \tilde{F}_1 \, d\mathcal{V} \tag{4.37}$$

where $\tilde{F}_1$ and $\tilde{F}_1$ are the mass fractions of the two gases. The amount of mixing is an indicator of the potential for chemical reactions. The evolution in time of the integral quantities $\mathcal{K}$, $\mathcal{W}$ and $\mathcal{M}$ are presented in figures 4.18, 4.19 and 4.20, respectively. The spatial distribution of the two fluids in the computational domain is described in Figure 4.22 by the profiles of the SF_6 profiles at different times ($t = 1.90; 2.22; 2.70; 3.26; 3.82\, ms$). Additional quantitative informations regarding the turbulence kinetic energy are given by the TKE profiles plotted in Figure 4.21 at the same five time levels.

The $K - L$ and $K - \epsilon$ turbulence models are applied after $t = 1.26ms$, when the reflected shock wave is approaching from the end wall to the second interface. The amplification of the turbulence kinetic energy by the re-shock corresponds to the

jump of $\mathcal{K}$ visible in Figure 4.18 at around $t = 1.5ms$. The TKE profiles at $t = 1.90ms$ presented in Figure 4.21 show that the two turbulence models capture accurately the TKE amplification by the reflected shock. However, the TKE dissipation at the left interface (unaffected by the re-shock yet) is overestimated by the $K - \epsilon$ model. The second jump of the total kinetic energy at around $t = 2ms$ corresponds to the interaction of the primary reflected wave with the left interface. The last TKE amplification is produced at around $t = 2.4ms$ by a second reflection from the wall interacting with the right interface. The TKE profiles at $t = 2.22ms$ and $t = 2.70ms$ (Figure 4.21) show that the turbulence models estimate correctly the TKE enhancement produced by these two last shock-interface interactions. The rate of total turbulence kinetic energy dissipation after $t = 2.70ms$ is underestimated by the two turbulence models. The TKE profiles at $t = 3.26ms$ and $t = 3.82ms$ suggest that this is caused by insufficient TKE dissipation at the left interface. The evolution of $\mathcal{K}$ predicted by the $K-L$ model exhibits additional TKE amplifications produced by the interaction of a third reflection with the right and left interfaces at around $t = 3.3ms$ and $t = 3.8ms$ respectively. This interaction is present also in the ILES results, but with a lower intensity. The integral length of the mixing zone $\mathcal{W}$ and the total mixing $\mathcal{M}$ presented in Figures 4.19 and 4.20 are in excellent agreement with the ILES results, as well as the SF_6 volume fraction profiles presented in Figure 4.22. The values of the peaks of the turbulence kinetic energy are presented in Tables 4.8 and 4.9.

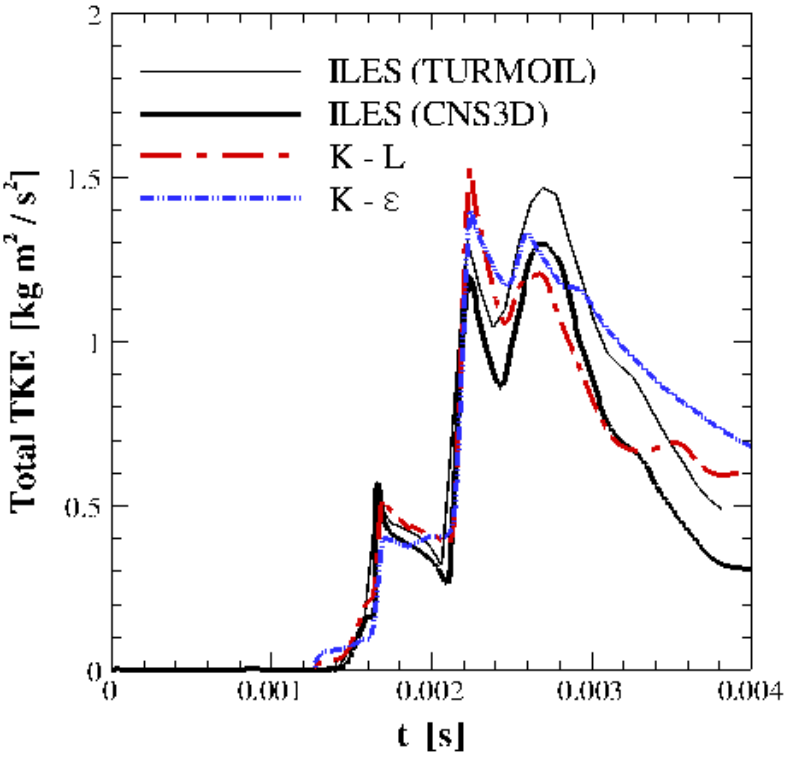

Figure 4.18: The evolution of the total kinetic energy in time.

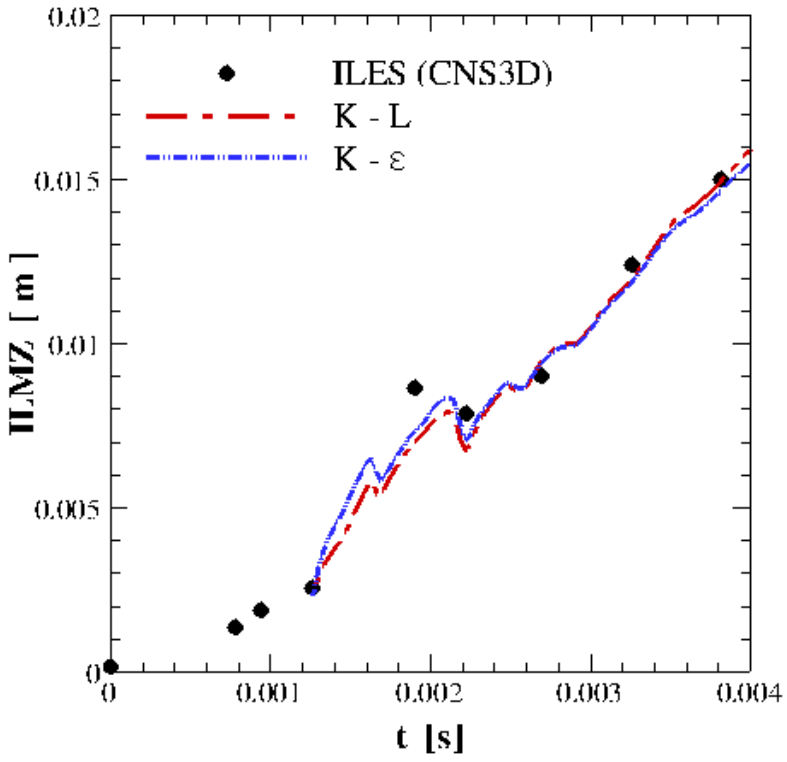

Figure 4.19: The evolution of the integral length of the mixing zone in time.

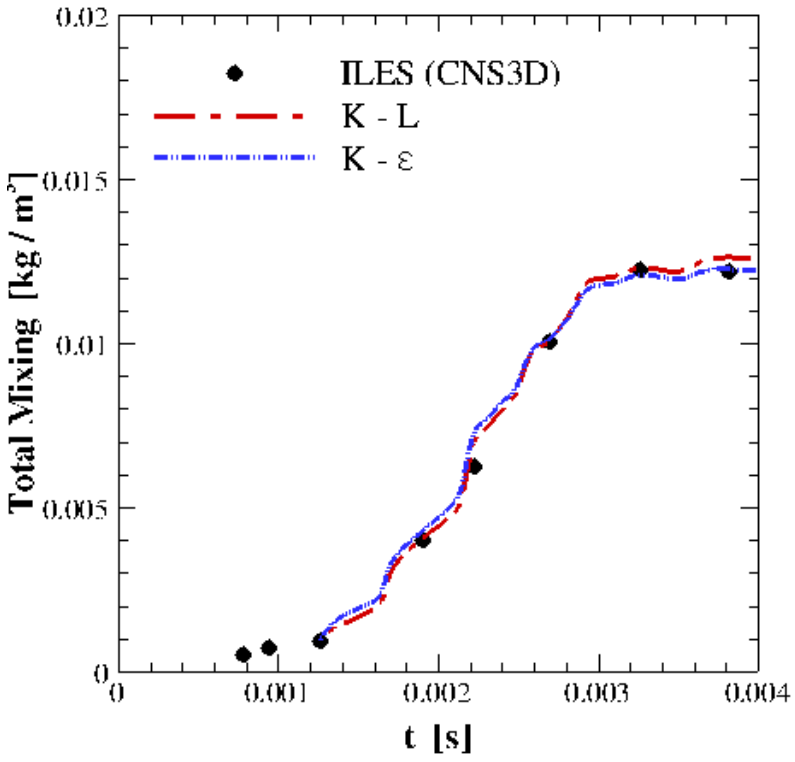

Figure 4.20: The evolution of the total mixing in time.

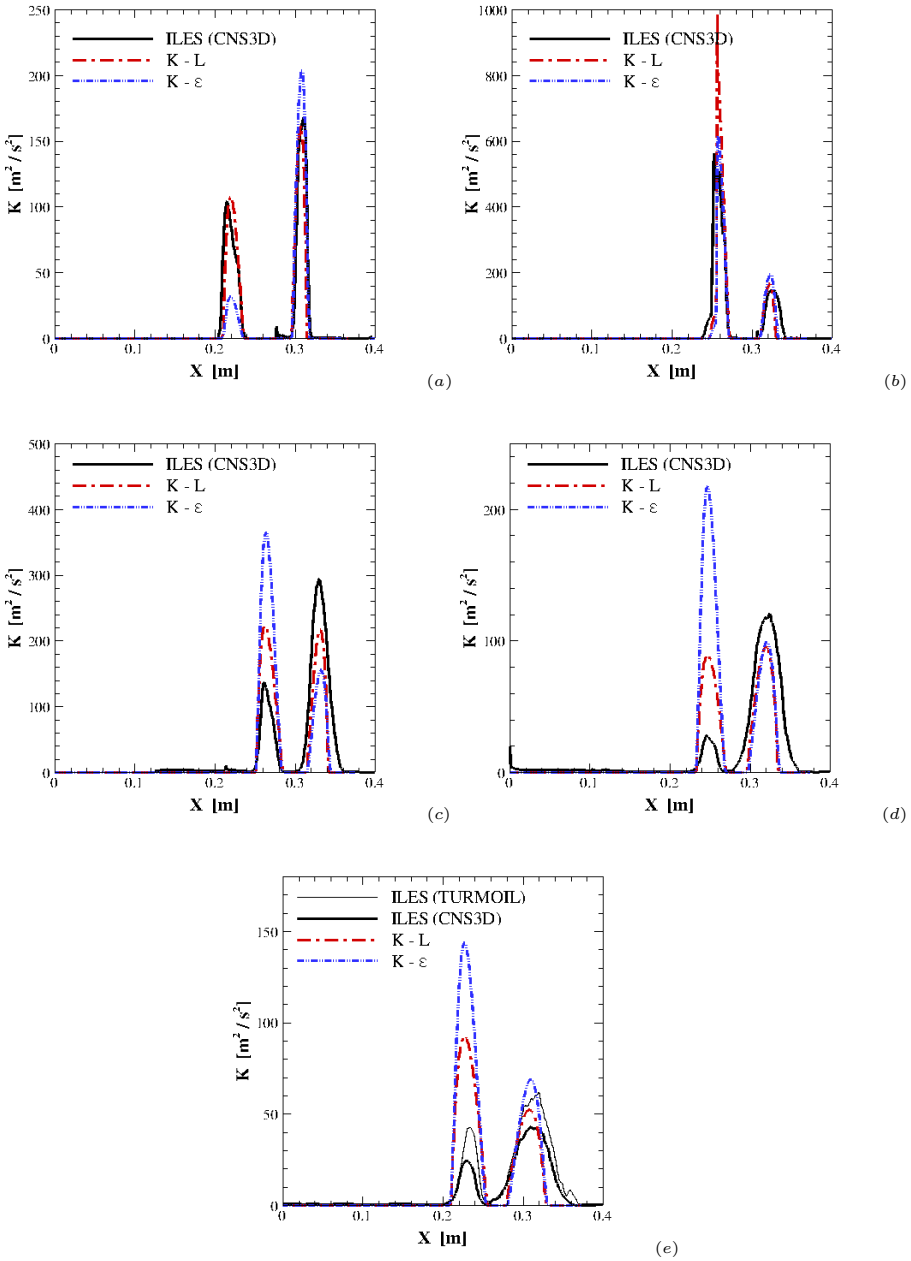

Figure 4.21: Turbulence kinetic energy profiles. (a) $t = 1.90ms$; (b) $t = 2.22ms$; (c) $t = 2.70ms$; (a) $t = 3.26ms$; (a) $t = 3.82ms$.

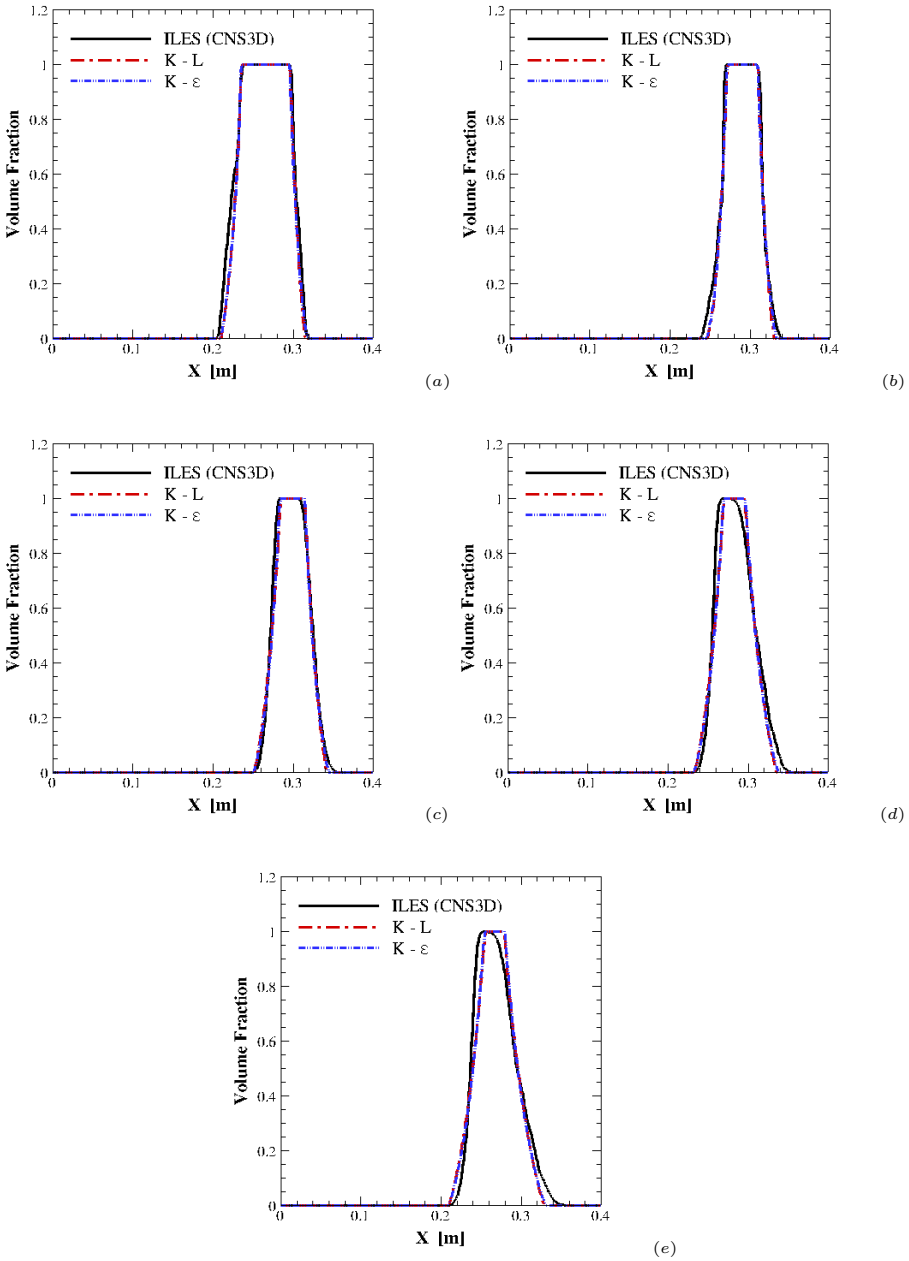

Figure 4.22: Volume fraction profiles. (a) $t = 1.90ms$; (b) $t = 2.22ms$; (c) $t = 2.70ms$; (a) $t = 3.26ms$; (a) $t = 3.82ms$.

Time	TKE $[m^2/s^2]$		
$[ms]$	$K-L$	$K-\epsilon$	ILES
1.90	109.5	031.8	107.6
2.22	969.0	612.3	562.5
2.70	236.1	466.6	140.0
3.26	089.9	219.4	030.3
3.82	094.3	140.5	025.1

Table 4.8: TKE peaks in the left mixing zone

Time	TKE $[m^2/s^2]$		
$[ms]$	$K-L$	$K-\epsilon$	ILES
1.90	175.5	209.1	180.3
2.22	190.1	200.5	155.5
2.70	217.2	256.7	299.8
3.26	097.8	098.9	119.5
3.82	053.2	070.2	044.5

Table 4.9: TKE peaks in the right mixing zone

4.3.3 Influence of some modeling parameters

The double planar RMI test case was used also as test problem for assessing the influence of the choice regarding the estimation of some important quantities in the $K-L$ and $K-\epsilon$ turbulence models, such as the Atwood number, the turbulent stresses and the turbulence kinetic energy source.

As mentioned in section 2.7, a simplified formula was used by Chiravalle (2006) for the calculation of the Atwood number A (equation 2.117). Figure 4.23 presents the effect of using this approach on the development of the instability. It is clear that the simplified approach of Chiravalle (2006) fails to predict the enhancement of the turbulence kinetic energy by the second reflection from the end-wall. As a result, the mixing at late time is also underestimated. It is concluded that the original approach of Dimonte and Tipton (2006) is more suitable when simulating RMI problems involving multiple shocks.

Another issue regarding the $K-L$ model is the absence of the deviatoric part of the

turbulent stress tensor. An alternative to the suppression of the deviatoric terms is the use of some limiters for values of the symmetric part of the tensor, as discussed at the end of section 2.7. Figure 4.24 compares the evolution of the RM instability obtained using the two approaches. It is clear that the limiting procedures proposed in the present work allows the use of the classical Boussinesq formula for the Reynolds stresses for the one-dimensional RMI problems. However, additional investigations should be made regarding two and three-dimensional problems.
Regarding the $K-\epsilon$ turbulence model, the present work employs a modified turbulence source term design to capture the amplification of the turbulence by an impulsive acceleration regardless of the directions of the pressure and density gradients, as described in section 2.8. The influence of the modification of the turbulence source is shown in Figure 4.25. The approach introduced in the present work clearly improves the estimation of the turbulence kinetic energy by shock-interface interaction.

4.3.4 Influence of the numerical methods

The influence of the spatial discretization schemes on the results is investigated considering again the HLL and the HLLC Riemann solvers, together with second, third and fifth order MUSCL schemes. The control parameters chosen for the this case are the total turbulence kinetic energy and the total mixing. The results are presented in Figure 4.26 for the $K-L$ model and in Figure 4.27 for the $K-\epsilon$ model. It is found that in general, the numerics have a more important influence on the $K-\epsilon$. The collapsing of the lines in Figures 4.26 and 4.27 suggests that the HLLC solver is better suitable for solving complex RMI problems, and the reconstruction scheme should be of third order of accuracy, or higher.

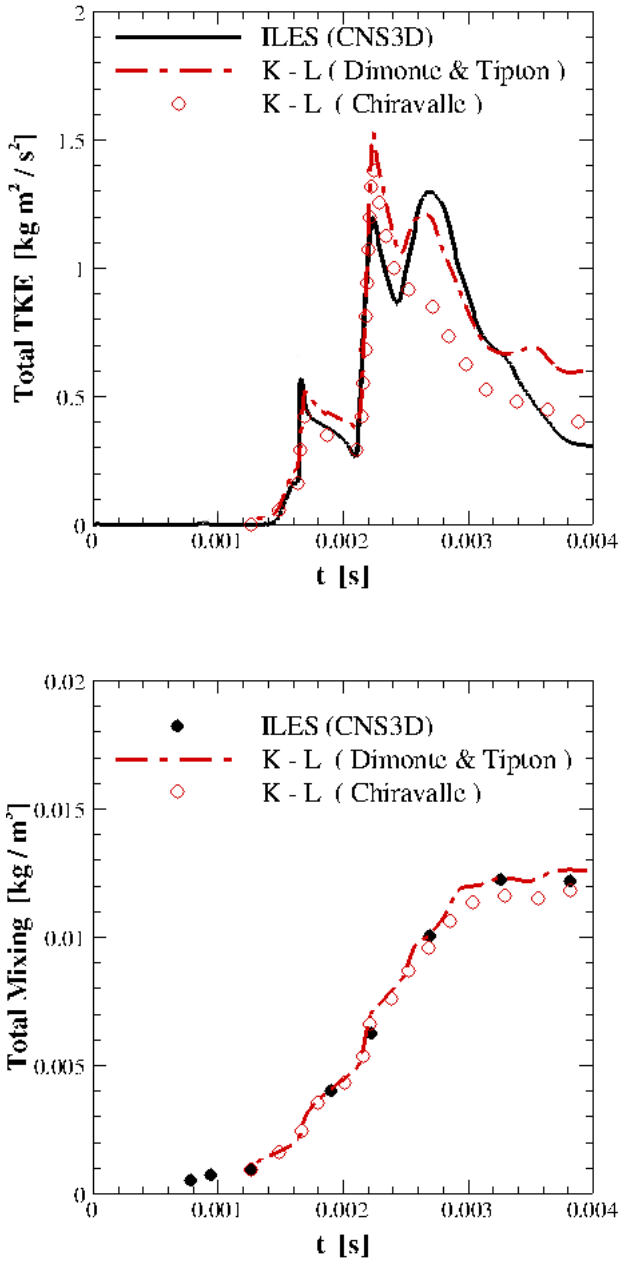

Figure 4.23: Influence of the computing method for the local Atwood number on the $K - L$ model applied to the double planar RMI.

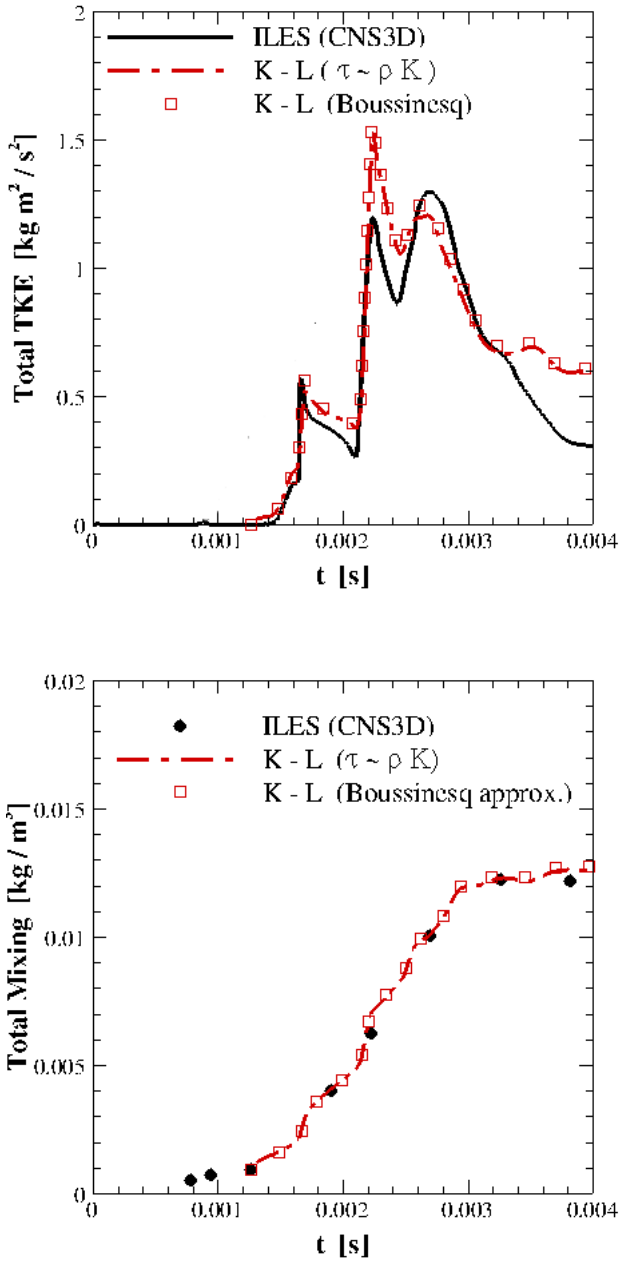

Figure 4.24: Influence of the computing method for the turbulent stress on the $K-L$ model applied to the double planar RMI.

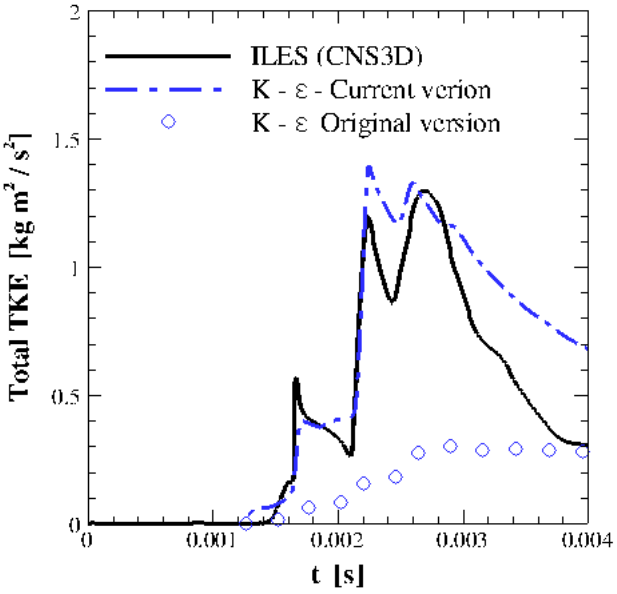

Figure 4.25: Influence of the turbulence kinetic energy source on the $K - \epsilon$ model applied to the double planar RMI.

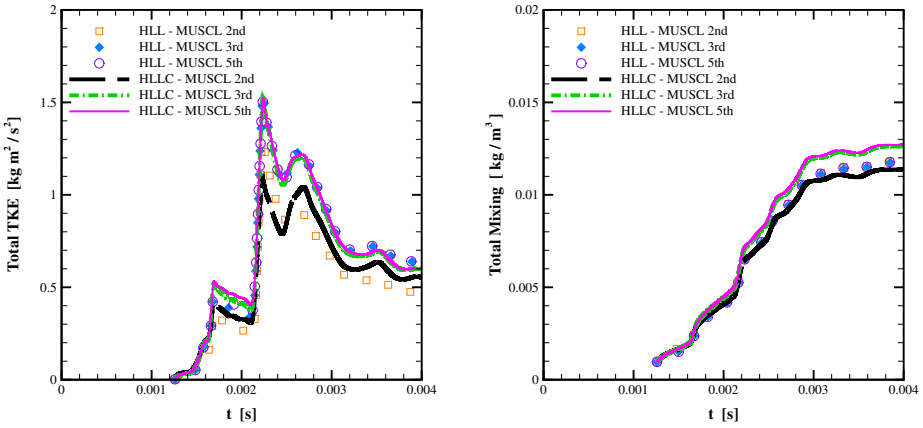

Figure 4.26: Influence of the numerical methods on the $K - L$ model

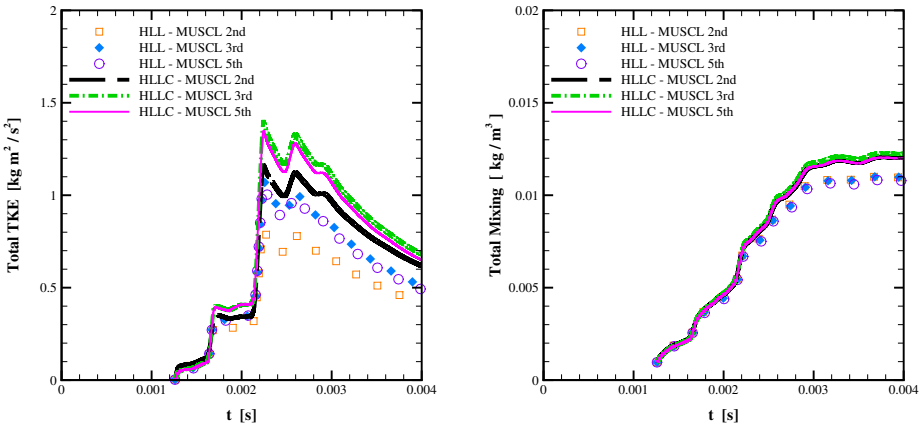

Figure 4.27: Influence of the numerical methods on the $K - L$ model

Chapter 5

Conclusions

In the present work the $K-L$ and $K-\epsilon$ turbulence models have been implemented and tested for three problems involving turbulent mixing induced by the Rayleigh-Taylor and Richtmyer-Meshkov instabilities. The validation of the results is based on the high resolution Implicit Large Eddy Simulations of Youngs (2010), Thornber et al. (2010) and Hahn et al. (2010).

The turbulence kinetic energy sources have been modified in order to reproduce accurately the amplification of the turbulence in the mixing zone. Their formulation depends on the type of the instability. The instability is considered to be RM-like if the ratio of the mean flow and the fluctuation time scales is higher than a threshold Λ_Θ and RT-like otherwise. This criterion is based on the acceleration of the fluid particle and it is not directly dependent on the size of the time step. The turbulence source is set to zero if the instability is found RT-like (produced by a gradual acceleration) if the pressure gradient is not opposing the density gradient. The value $\Lambda_\Theta = 0.25$ was found to give satisfactory results for both $K-L$ and $K-\epsilon$ models. The turbulence source in the $K-L$ model is based on a local Atwood number. In the present work, the simpler version of the Atwood number used by Chiravalle (2006) was implemented in addition to the formulation proposed by Dimonte and Tipton (2006).

A modification regarding the modeling of the turbulent stresses was applied to the $K-L$ model. Instead of neglecting the deviatoric part of the stress tensor, as pro-

posed by the authors of the original model (Dimonte and Tipton (2006)), a limiting procedure was applied to the diagonal of the tensor. The motivation is the fact that the absence of the deviatoric part would not allow the simulation of the mixing induced by the Kelvin-Helmholtz instability. The two procedures were found to give the same results for all the test cases considered.

In the case of the classical Rayleigh-Taylor problem both turbulence models predicted correctly the self similar growth rate, giving the parameters $\alpha_{B,S} = 0.05..0.007$, increasing with the initial Atwood number. The spatial distributions of the fluid concentrations and of the turbulence kinetic energy were found in good agreement with the ILES results.

The two turbulence models were able to simulate correctly the mixing induced by the Richtmyer-Meshkov instability on a planar interface. The growth rate was found $\eta \sim t^{\theta}$, with $\theta \simeq 0.26$, slightly higher than predicted by ILES.
The volume fraction profiles plotted against the normalized coordinate perpendicular to the interface prove that both models preserve the self similar character of the RT and RM mixing at late times.

The two models have been tested for a more complex problem, involving the mixing induced at two planar interfaces by multiple shock reflections and refractions. The interfaces separate fluids with different thermodynamic properties (air and SF_6). Both turbulence models produced satisfactory results regarding the total mixing, the width of the mixing zone and total turbulence kinetic energy. The volume fraction profiles are in good agreement with the ILES data. However, discrepancies regarding the intensity and the distribution of the turbulence kinetic energy have been found, especially at late times. The $K - L$ model was found particularly sensitive to the reflections from the solid wall at late times. The models did not simulate correctly the merging of the mixing zones corresponding to the two interfaces predicted by ILES at very late times. It was also found that the enhancement of the turbulence kinetic energy by the re-shocks is better captured by the $K - L$ model when the original approach for computing the local Atwood number is used.

The influence of the spatial discretization schemes on the results was investigated for the three problems considered. The HLL and HLLC approximate Rie-

mann solvers were used for estimating the convective fluxes through the cell boundaries and MUSCL reconstruction schemes up to the fifth order of accuracy. The results obtained for the classical Rayleigh-Taylor instability are not sensitive to the numerical scheme employed (if grid convergence has been achieved). This can be explained by the fact that the initialization method proposed and used here eliminates the initial density discontinuity at the interface. However, it is concluded that in the general case, when strong gradients are present in the flow field, the HLLC solver is the better choice, and it should be used with a MUSCL reconstruction scheme of third order of accuracy or higher.

Finally, it is concluded that both the $K - L$ and $K - \epsilon$ turbulence models with the modifications mentioned above are capable of successfully simulating the turbulent mixing induced by the Rayleigh-Taylor and Richtmyer-Meshkov instabilities. The two models predict correctly the growth rate of the perturbation, the concentrations of the fluids and integral quantities such as the total mixing and the integral length of the mixing zone. Difficulties occur for the estimation of the turbulence kinetic energy amplification produced by multiple re-shocks.

Regarding the future research, it is considered of high importance finding the appropriate methods of initializing the turbulence quantities K, L and ϵ. The initial value of the eddy size L_0 could be considered proportional to the initial amplitude of the perturbation η_0 and, from dimensional considerations, it is natural to assume $K_0 \sim A_0 \eta_0 g$ for the case of the pure Rayleigh-Taylor instability (section 4.1). Obviously the problem is more difficult in the case of the Richtmyer-Meshkov instability, when the acceleration of the interface is not known *a prori* and the strong pressure gradients are difficult to estimate. Ideally, the initialization procedure should capture also the spectrum of the initial perturbation which can have an important influence on the development of the instability, as found by Thornber et al. (2010).
The accuracy of the models when applied to turbulent mixing problems involving fluids with different thermodynamic properties (such as specific heats and adiabatic exponents) could be improved by ensuring a better coupling of the mass fraction equation. This could be achieved by using an improved Riemann solver (not necessarily HHL or HLLC) which takes into account the dependency of of the adi-

abatic exponent of the mixture on the concentrations of the fluids.
Finally, the turbulence must be tested for problems with o more complex geometry, such as the one dimensional spherical (or cylindrical) Richtmyer-Meshkov instability, and also two and three-dimensional mixing problems.

Appendix A

Implementation of the boundary conditions

Two types of boundary conditions have been used in the present work: i) solid wall and ii) non-reflective boundary conditions. A ghost cell procedure is used for their implementation. The one-dimensional computational domain is extended by two sets of ghost cells, one at the left end and one at the right end of the domain, as shown in Figure A.1. The number of ghost cells N_{G} is equal to the order of accuracy of the reconstruction scheme. The relation between the values of the flow field variables in the centre of the ghost cells and their values in the computational domain depends on the type of the boundary condition imposed. The conservative variables corresponding to left and right ghost cells are noted $U_{\mathrm{GL}} = (\rho, \rho u, \rho\phi)$ and

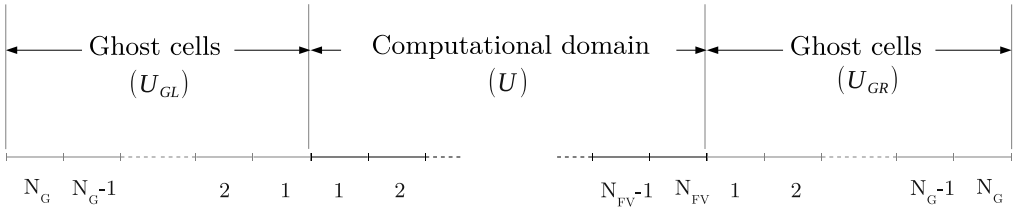

Figure A.1: Computational domain and ghost cells.

$U_{\mathrm{GR}} = (\rho, \rho u, \rho\phi)_{\mathrm{GR}}$ respectively (ϕ is the generic notation for E, F , K, L, ϵ). Their dependency on the conservative variables U in the flow domain is as follows.

1. In the case solid wall boundary conditions, the components of $U_{\mathrm{GL,GR}}$ and U are symmetric, with the exception of the momentum ρu which is antisymmetric:

   Left boundary:

$$\begin{aligned} \rho_{\mathrm{GL}i} &= \rho_i \\ (\rho u)_{\mathrm{GL}i} &= -(\rho u)_i \\ (\rho\phi)_{\mathrm{GL}i} &= -(\rho\phi)_i \\ i &= 1, 2, .., N_{\mathrm{G}} \end{aligned} \tag{A.1}$$

   Right boundary:

$$\begin{aligned} \rho_{\mathrm{GR}i} &= \rho_{N_{\mathrm{FV}}-i+1} \\ (\rho u)_{\mathrm{GR}i} &= -(\rho u)_{N_{\mathrm{FV}}-i+1} \\ (\rho\phi)_{\mathrm{GR}i} &= -(\rho\phi)_{N_{\mathrm{FV}}-i+1} \\ i &= 1, 2, .., N_{\mathrm{G}} \end{aligned} \tag{A.2}$$

2. In the case of permeable boundary conditions a second order extrapolation is used for calculating U_{GL} and U_{GR}:

   Left boundary:

$$\begin{aligned} U_{\mathrm{GL1}} &= 1.5U_1 - 0.5U_2 \\ U_{\mathrm{GL2}} &= 1.5U_{\mathrm{GL1}} - 0.5U_1 \\ U_{\mathrm{GL}i} &= 1.5U_{\mathrm{GL}i-1} - 0.5U_{\mathrm{GL}i-2} \ , \ i = 3, .., N_{\mathrm{G}} \end{aligned} \tag{A.3}$$

   Right boundary:

$$\begin{aligned} U_{\mathrm{GR1}} &= 1.5U_{N_{\mathrm{FV}}} - 0.5U_{N_{\mathrm{FV}}-1} \\ U_{\mathrm{GR2}} &= 1.5U_{\mathrm{GR1}} - 0.5U_{N_{\mathrm{FV}}} \\ U_{\mathrm{GR}i} &= 1.5U_{\mathrm{GR}i-1} - 0.5U_{\mathrm{GR}i-2} \ , \ i = 3, .., N_{\mathrm{G}} \end{aligned} \tag{A.4}$$

Remark: The flow field values at the centre of the ghost cells are updated at each Runge-Kutta iteration.

Appendix B

RTI: Additional plots

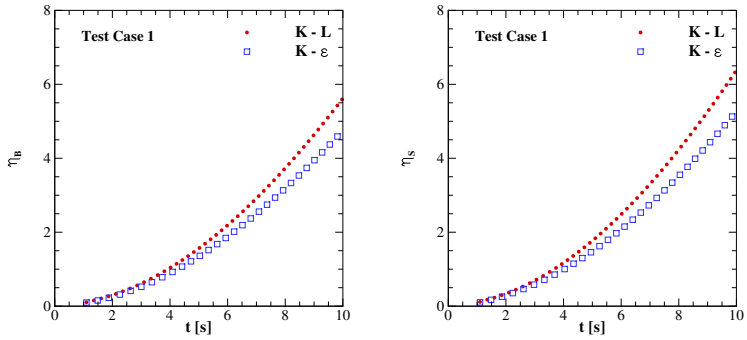

Figure B.1: The perturbation amplitude $\eta_{b,s}$ for Test Case 1 (left: bubbles; right: spikes).

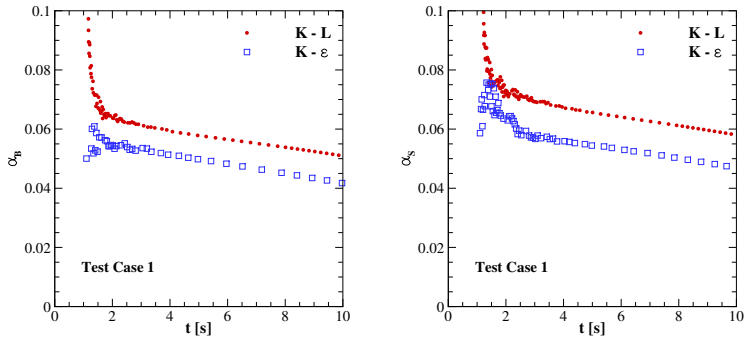

Figure B.2: The RTI growth rate parameter $\alpha_{b,s}$ for Test Case 1 (left: bubbles; right: spikes).

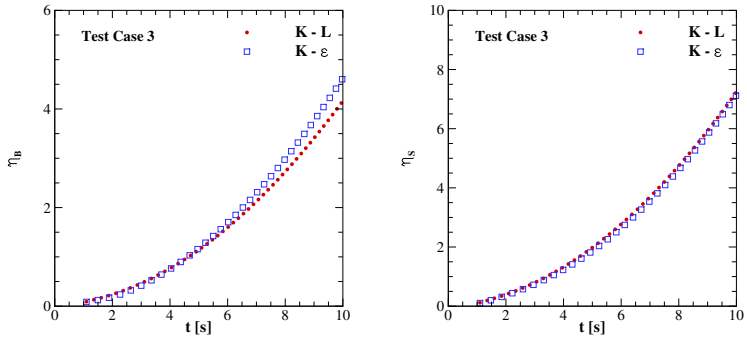

Figure B.3: The perturbation amplitude $\eta_{b,s}$ for Test Case 3 (left: bubbles; right: spikes).

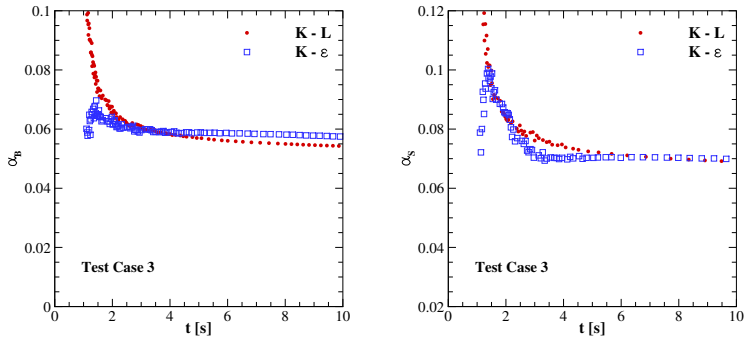

Figure B.4: The RTI growth rate parameter $\alpha_{b,s}$ for Test Case 3 (left: bubbles; right: spikes).

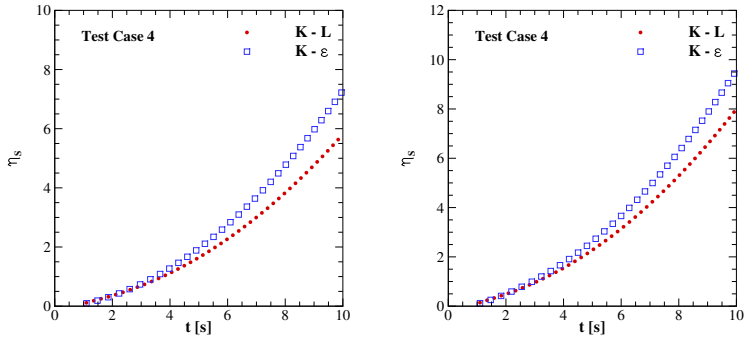

Figure B.5: The perturbation amplitude $\eta_{b,s}$ for Test Case 4 (left: bubbles; right: spikes).

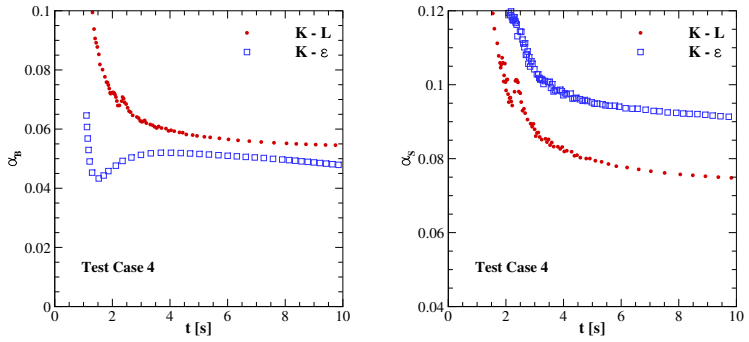

Figure B.6: The RTI growth rate parameter $\alpha_{b,s}$ for Test Case 4 (left: bubbles; right: spikes).

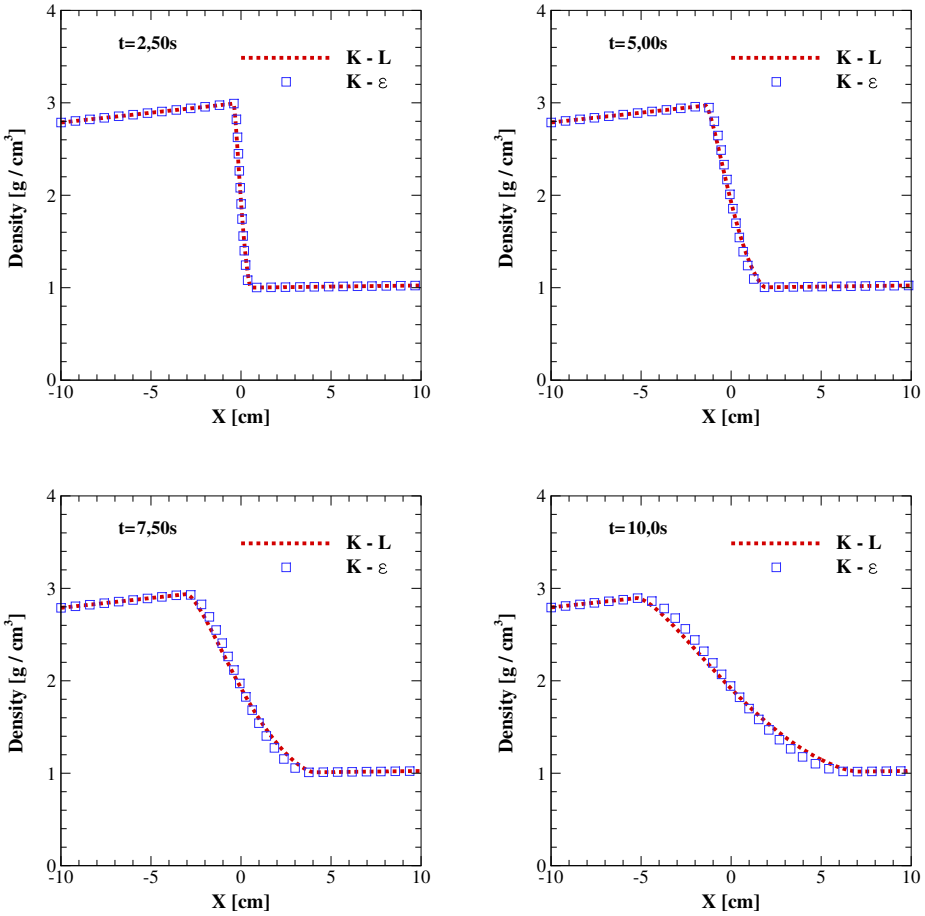

Figure B.7: Density profiles at $t = 2.5s;\ 5.0s;\ 7.5s;\ 10.0s$ (Test Case 2).

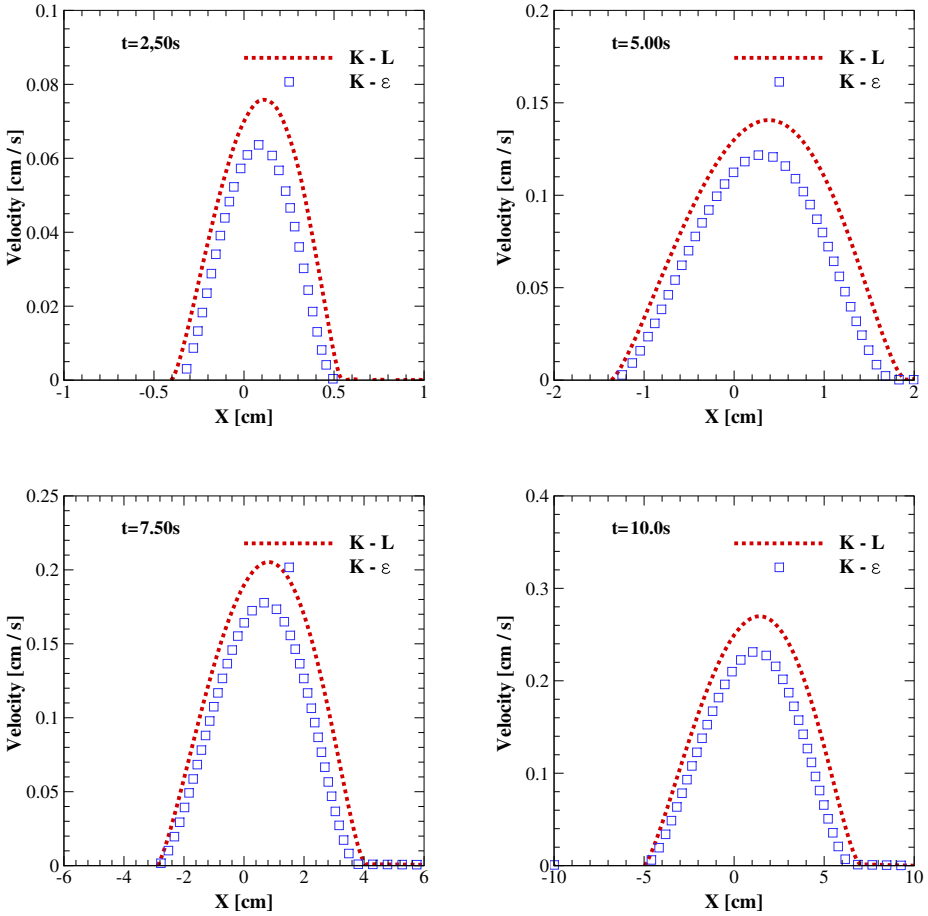

Figure B.8: Velocity profiles at $t = 2.5s;\ 5.0s;\ 7.5s;\ 10.0s$ (Test Case 2).

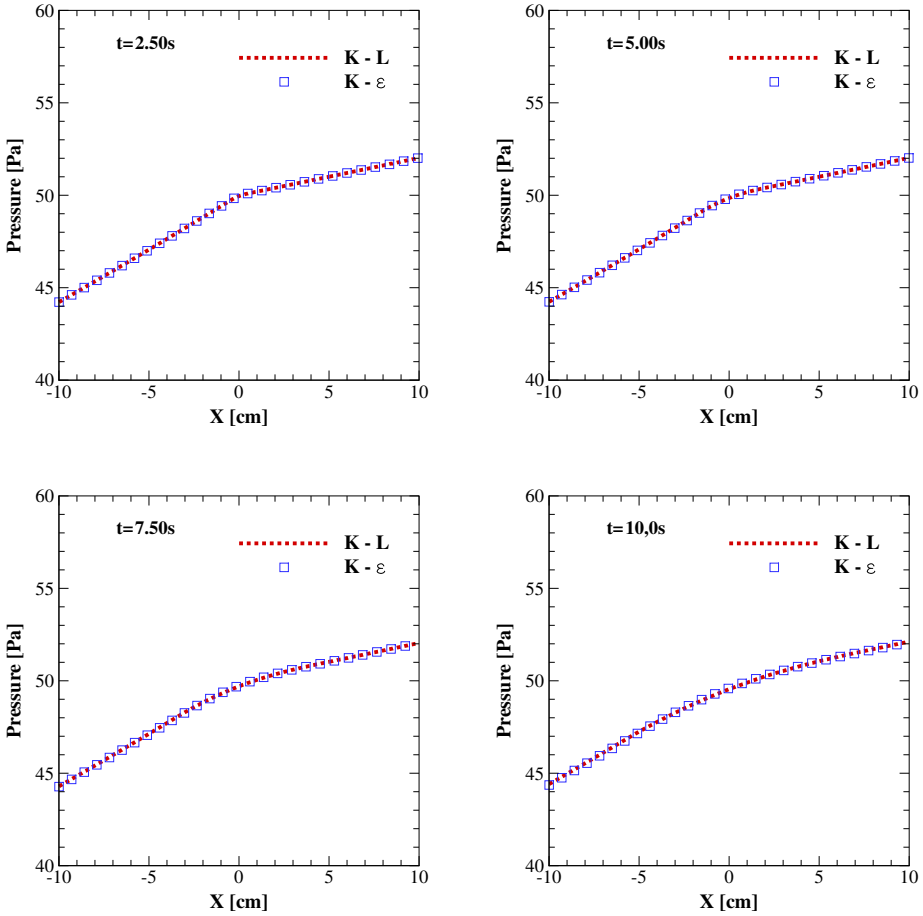

Figure B.9: Pressure profiles at $t = 2.5s;\ 5.0s;\ 7.5s;\ 10.0s$ (Test Case 2).

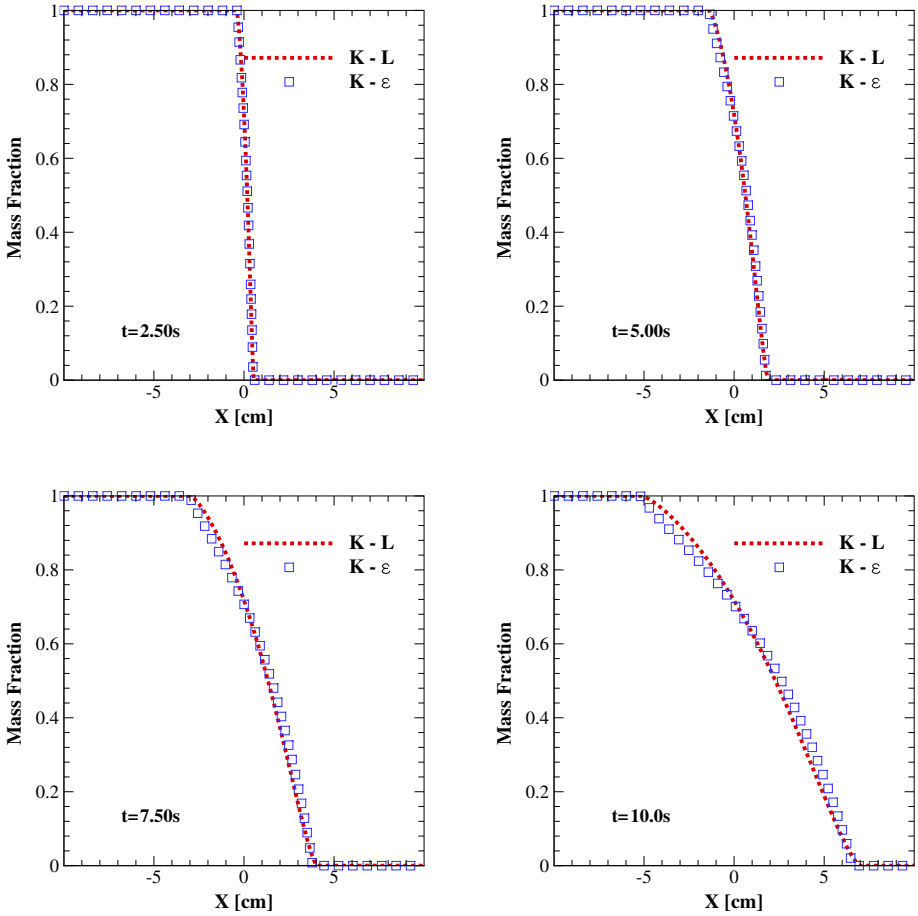

Figure B.10: Mass fraction profiles at $t = 2.5s;\ 5.0s;\ 7.5s;\ 10.0s$ (Test Case 2).

Appendix C

RTI: Grid convergence tests

Four grids have been considered for the grid convergence tests: G1 ($N_{\mathrm{FV}x} = 400$, $\Delta x = 0.05cm$); G2 ($N_{\mathrm{FV}x} = 800$, $\Delta x = 0.025cm$); G3 ($N_{\mathrm{FV}x} = 1600$, $\Delta x = 0.0125cm$). The control parameters are perturbation amplitudes $\eta_{\mathrm{b,s}}$ at $t = 10s$. The test results are presented in the following tables.

Grid	η_{B}		η_{S}	
	$K-L$	$K-\epsilon$	$K-L$	$K-\epsilon$
G1	5.40	4.39	6.20	5.21
G2	5.50	4.50	6.45	5.41
G3	5.53	4.52	6.48	5.45

Table C.1: The influence of the grid resolution on the perturbation amplitude obtained with the $K-L$ and $K-\epsilon$ turbulence models for the Test Case 1

Grid	η_{B}		η_{S}	
	$K-L$	$K-\epsilon$	$K-L$	$K-\epsilon$
G1	4.31	4.50	6.22	6.15
G2	4.50	5.00	6.58	6.42
G3	4.55	5.05	6.70	6.50

Table C.2: The influence of the grid resolution on the perturbation amplitude obtained with the $K-L$ and $K-\epsilon$ turbulence models for the Test Case 2

Grid	η_B		η_S	
	$K-L$	$K-\epsilon$	$K-L$	$K-\epsilon$
G1	4.15	4.05	6.52	6.31
G2	4.50	4.29	6.65	6.96
G3	4.00	4.50	6.98	7.00

Table C.3: The influence of the grid resolution on the perturbation amplitude obtained with the $K-L$ and $K-\epsilon$ turbulence models for the Test Case 3

Grid	η_B		η_S	
	$K-L$	$K-\epsilon$	$K-L$	$K-\epsilon$
G1	5.25	6.55	7.50	9.11
G2	5.70	7.00	7.95	9.46
G3	5.91	7.11	8.00	9.55

Table C.4: The influence of the grid resolution on the perturbation amplitude obtained with the $K-L$ and $K-\epsilon$ turbulence models for the Test Case 4

References

Almgren, A., J. Bell, C. Rendleman, and M. Zingale (2000). Low mach number modeling of type ia supernovae. i hydrodynamics. *Astrophys. J. 637*, 922–936.

Alon, U., J. Hecht, D. Mukamel, and D. Shvarts (1995). Power laws and similarity of Rayleigh-Taylor and Richtmyer-Meshkov mixing fronts at all density ratios. *Phys. Rev. Lett. 72*, 2867–2870.

Amendt, P., J. Colvin, R. Tipton, D. Hinkel, M. Edwards, O. Landen, J.D., Ramshaw, L. Suter, W. Varnum, , and R. Watt (2002). Indirect-drive noncryogenic double-shell ignition targets for the national ignition facility: Design and analysis. *Phys. Plasmas 9*, 2221–2233.

Andrews, M. and D. Spalding (1990). A simple experiment to investigate two dimensional mixing by Rayleigh-Taylor instabilty. *Phys. Fluids A 2*, 922.

Andronov, V. A., S. Bakhrakh, E. Meshkov, V. Nikiforov, A. Pevnitskii, and A. Tolshmyakov (1976). *Sov.Phys.JETP 44*, 424.

Andronov, V. A., S. Bakhrakh, E. Meshkov, V. Nikiforov, A. Pevnitskii, and A. Tolshmyakov (1982). An experimental investigation and numerical modeling of turbulent mixing in one-dimensional flows. *Sov.Phys.Dokl 27*, 393–396.

Arnett, D. (2000). The role of mixing in astrophysics. *App. J. Suppl. 127*, 213–217.

Balsara, D. and C.-W. Shu (2000). Monotonicity preserving weighted essentially non-oscillatory schemes with increasingly high order of accuracy. *J. Comput. Phys. 160*, 405–452.

Besnard, D., F. H. Harlow, R. M. Rauentzahn, and C. Zemach (1992). Turbulence transport equations for variable-density turbulence and their relationship to two-field models. *LA-12303-MS / 017292*.

Billet, S. and E. Toro (1998). Unsplit WAF-type schemes for three dimensional hyperbolic conservation laws. In *Numerical Methods for Wave Propagation*, Toro E.F and Clarke J.F (Editors), Kluwer Academic Publishers.

Charakhch'yan, A. A. (2001). Reshocking at the non-linear stage of Richtmyer-Meshkov instability. *Plasma Phys. Control. Fusion 43*, 1169–1179.

Chen, Y., J. Glimm, D. A. Sharp, and Q. Zhang (1996). A two-phase flow model of the Rayleigh-Taylor mixing zone. *Phys. Fluids 8*, 816.

Chiravalle, V. (2006). The K-L turbulence model for describing buoyancy-driven fluid instabilities. *Laser and Particle Beams 24*, 381–394.

Cook, A. W. (2009). Enthalpy diffusion in multicomponent flows. *Phys. Fluids 21*.

Davis, S. F. (1988). Simplified second-order Godunov-type methods. *SIAM J. Sci. Stat. Comput. 9*, 445–473.

Dimonte, G. (2000). Spanwise homogeneous buoyancy-drag model for Rayleigh-Taylor mixing and experimental evaluation. *Physics of Plasma 7*, 2255.

Dimonte, G., C. E. Frerkinf, and M. Schneider (1955). Richtmyer-meshkov instability in the turbulent regime. *Phys. Rev. Lett. 74*, 4855–4858.

Dimonte, G. and M. Schneider (1996). Turbulent Rayleigh-Taylor instability experiments with variable acceleration. *Phys. Rev. E 54*, 3740.

Dimonte, G. and M. Schneider (2000). Density ratio dependence of Rayleigh-Taylor mixing for sustained and impulsive accelerations. *Phys. Fluids 12*, 304.

Dimonte, G. and R. Tipton (2006). K-L turbulence model for the self-similar growth of the Rayleigh-Taylor and Richtmyer-Meshkov instabilities. *Phys. Fluids 18*, 2009–2015.

Dimonte, G., D. L. Youngs, A. Dimits, S. Weber, M. Marinak, S. W. Wunsch, C. Garasi, A. Robinson, M. Anrews, P. Ramaprabhu, A. Calder, B. Fryxell, J. Biello, L. Dursi, P. MacNeice, K. Olson, P. Ricker, R. Rosner, F. Timmes, H. Tufo, Y.-N. Young, and M. ZIngale (2004). A comparative study of the turbulent Rayleigh-Taylor instability using high-resolution three-dimensional numerical simulations: The Alpha-Group collaboration. *Physics of Fluids 16*(5).

Drikakis, D. and W. Rider (2005). *High-Resolution Methods for Incompressible and Low Speed Flows* (1 ed.). Springer. ISBN: 3-540-22136-0.

Fermi, E. and J. von Neumann (1953). Taylor instability of incompressible liquid. part 2. Taylor instability at the boundary of two incompressible fluids. Technical Report AECU-2959, Los Alamos Scientific Laboratory.

Fraley, G. (1986). Rayleigh-Taylor stability for a normal shockwave-density discontinuity interaction. *Phys. Fluids 29*, 376–386.

Gauthier, S. and M. Bonnet (2000). A $k - \epsilon$ model for turbulent mixing in shock-tube flows induced by rayleigh-taylor instability. *Phys. Fluids A 2*, 1685–1694.

Godunov, S. (1959). A finite difference method for the computation of discontinuous solutions of the equations of fluid dynamics. *Mat. Sb. 47*, 357–393.

Goncharov, V. (2002). Analytical model of nonlinear, single mode, classical Rayleigh-Taylor instability at arbitrary atwood numbers. *Phys. Rev, Lett. 88*, 134502.

Gottlieb, S. and C.-W. Shu. (1998). Total variation diminishing Runge-Kutta schemes. *Math. Comput. 67*, 73âĂŞ85.

G.Van Albada, B. Van Leer, and W. W. Roberts (1982). A comparative study of computational methods in cosmic gas dynamics. *Astron. Astrophysics 108*, 76.

Hahn, M., D. Drikakis, D. Youngs, and J. Williams (2010). Richtmyer-meshkov turbulent mixing arising from an inclined material interface with realistic surface perturbations and reshocked ïňĆow. *Phys. Fluids*. To be published.

Harten, A., P. Lax, and B. van Leer (1983). On up-stream differencing and Godunov-type schemes for hyperbolic conservation laws. *SIAM Review 25*, 35–61.

Holder, D., A. Smith, C. Barton, and D. Youngs (2003). Shock-tube experiments on Richtmyer-Meshkov instability growth using an enlarged double-bump perturbation. *Particle Beams 23*, 411–418.

Holmes, R., G. Dimonte, B. Fryxell, M. Gittings, J. Grove, M. Schneider, D. Sharp, A. Velikovich, R. Weaver, and Q. Zhang (1999). Richtmyer-meshkov instability growth: experiment, simulation and theory. *J. Fluid Mech. 389*, 55–79.

Houas, L. (1985). In *Proceedings of the 15th Interanational Symposium on Shock Waves and Shock Tubes*, Berkeley, California.

Jameson, A. (1983). The evolution of computational methods in aerodynamics. *J. Appl. Math. 50*.

Kim, K. and C. Kim (2005). Accurate, efficient and monotonic numerical methods for multidimensional compressible ïňĆows. part ii. multi-dimensional limiting process. *J. Comput. Phys. 208*, 570–615.

Launder, B., G. Reece, and W. Rodi (1974). Progress in the development of a reynolds-stress turbulent closure. *Journal of Fluid Mechanics 83*(3).

Launder, B. and B. Sharma (1974). Application of the energy dissipation model of turbulence to the calculation of flow near a spinning disc. *Letters in Heat and Mass Transfer 1*(2).

Launder, E. and D. Spalding (1974). Turbulence model. *Comput. Meth. Appl. Mech. Eng. 3*, 264.

Lindl, J., R. McCroy, and E. Campbell (1992). Progress toward ignition and burn propagation in inertial confinement fusion. *Physics Today 45*, 32–40.

Menter, F. (1994). Two-equation eddy-viscosity turbulence models for engineering applications. *AIAA Journal 32*(8).

Meshkov, E. E. (1969). Instability of the interface of two gases accelerated by a shock wave. *Sov. Fluid Dyn. 43*, 101–104.

Meyer, K. A. and P. J. Blewett (1972). Numerical investigation of the stability of a shock accelerated interface between fluids. *Phys. Fluids 15*, 753–759.

Mikaelian, K. O. (1985). Technical Report UCRL-93499, Lawrence Livermore National Laboratory.

Mikaelian, K. O. (1989). Turbulent mixing generated by Rayleigh-Taylor and Richtmyer-Meshkov instabilities. *Phys. D 36*, 343–357.

Mikaelian, K. O. (1993). Growth rate of the Richtmyer-Meshkov instability at shocked interfaces. *Phys. Rev. Lett. 71*, 2903–2906.

Mikaelian, K. O. (1996). Analytic approach to non-linear Rayleigh-Taylor and Richtmyer-Meshkov instabilities. Technical Report UCRL-JC-125113, Lawrence Livermore National Laboratory.

Orlicz, G. (2012). *Incident shock Mach number effects on Richtmyer-Meshkov mixing with simultaneous density and velocity measurements*. Phd thesis, University of New Mexico.

Oron, D., L. Arazi, D. Kartoon, A. Rikanati, U. Alon, and D. Shvarts (2001). Dimensionality dependence of Rayleigh-Taylor and Richtmyer-Meshkov instability late-time scaling laws. *Phys. Plasmas 8*, 2883.

Osher, S. and F. Solomon (1982). Upwind difference schemes for hyperbolic conservation laws. *Math. Comput. 38*, 339–374.

Ramaprabhu, P. and M. Andrews (2004). Experimental investigation of Rayleigh-Taylor mixing at small atwood numbers. *J. Fluid Mech. 502*, 233.

Ramshaw, J. D. (1993). Hydrodynamic theory of multicomponent diffusion and thermal diffusion in multitemperature gas mixtures. *J. Non-Equilib. Thermodyn. 18*, 121–134.

Ramshaw, J. D. (1998). Simple model for linear and nonlinear mixing at unstable fluid interfaces with variable acceleration. *Phys. Rev. E 58*, 5834.

Ramshaw, J. D. (2002). Fluid dynamics and energetics in ideal gas mixtures. *Am. J.Phys. 70*, 508–512.

Rayleigh, L. (1883). Investigation of the character of the equilibrium of an incompressible heavy fluid of variable density. In *Proceedings of the London Mathematical Society*, 14, 171-177.

Read, K. I. (1984). Experimental investigation of turbulent mixing by Rayleigh-Taylor instability. *Phys. D 12*, 45–58.

Richtmyer, R. D. (1960). Taylor instability in shock acceleration of compressible fluids. *Communications on Pure and Applied Mathematics 13*, 297–319.

Roe, P. (1981). Approximate Riemann solvers, parameter vectors and difference schemes. *J. Comput. Phys. 43*, 357–372.

Roe, P. (1986). Characteristic-based schemes for the Euler equations. *Ann. Rev. Fluid Mech. 18*, 337.

Shvarts, D., D. Oron, L., R. Ofer, R. McCroy, and C. Verdon (1995). Nonlinear evolution of multi-mode Rayleigh-Taylor instability in two and three dimensions. *Phys. Plasmas 2*, 2465.

Sinha, K., K. Mahesh, and G. Candler. Modeling shock unsteadiness in shock/turbulence interaction. *Phys. Fluids 15*.

Spalart, P. and S. Allmaras (1992, November). A one-equation turbulence model for aerodynamic flows. *AIAA Paper 92-0439*.

Spiteri, R. and S. Ruuth (2002, November). A class of optimal high-order strong-stability preserving time discretization methods. *SIAM Journal of Scientific Computing 40*(2), 469âĂŞ491.

Taylor, G. (1950). The instability of liquid surfaces when accelerated in a direction perpendicular to their planes. *Proc. R. Soc. London, Ser. A 200*, 192–196.

Thornber, B. (2007). *Implicit Large Eddy Simulation for Unsteady Multi-Component Compressible Turbulent Flows*. Phd thesis, Cranfield University.

Thornber, B. J., D. Drikakis, D. L. Youngs, and J. R. Williams (2010). The influence of initial conditions on turbulent mixing due to Richtmyer-Meshkov instability. *J. Fluid Mech. 654*, 99–139.

Toro, E. F. (1999). *Riemann Solvers and Numerical Methods for Fluid Dynamics – A Practical Introduction* (2 ed.). Springer. ISBN: 3-540-65966-8.

Van Leer, B. (1977). Towards the ultimate conservative difference scheme.iv. a new approach to numerical convection. *J. Comput. Phys. 23*, 276–299.

Vandenboomgaerde, M., C. Mügler, and S. Gauthier (1998). Impulsive model for the Richtmyer-Meshkov instability. *Phys.Rev. E 58*, 1874–1882.

Velikovich, A. L. (1996). Analytic theory of Richtmyer-Meshkov instability for the case of reflected rarefication wave. *Phys.Fluids 8*, 1666–1879.

Wilcox, C. (1993). *Turbulence Modeling for CFD* (1 ed.). DCW Industries, Inc. ISBN: 0-9636051-0-0.

Wilcox, C. (2000). *Turbulence Modeling for CFD* (3 ed.). DCW Industries, Inc. ISBN: 1-928729-08-8.

Yang, J., T. Kubota, and E. Zuboski (1993). Applications of shock-induced mixing to supersonic combustion. *AIAA J. 31*, 854–862.

Yang, Y., Q. Zhang, and D. H. Sharp (1994). Small amplitude theory of Richtmyer-Meshkov instability. *Phys. Fluids 6*, 1856–1873.

Youngs, D. L. (1984). Numerical simulation of turbulent mixing by Rayleigh-Taylor instability. *Phys. D 12*, 32–44.

Youngs, D. L. (1989). Modelling turbulent mixing by Rayleigh-Taylor instability. *Phys. D 37*, 270–287.

Youngs, D. L. (1991). Three-dimensional numerical simulation of turbulent mixing by Rayleigh-Taylor instability. *Phys. Fluids A 3*(5), 1312–1320.

Youngs, D. L. (1994). Numerical simulation of mixing by Rayleigh-Taylor and Richtmyer-Meshkov instabilities. *Laser and Particle Beams 12*(4), 725–750.

Youngs, D. L. (2004). Effect of initial conditions on self-similar mixing. In *IWPCTM* 9.

Youngs, D. L. (2010). Large eddy simulation and 1D/2D engineering models for Rayleigh-Taylor mixing. In *IWPCTM* 12.

Zhang, Q. and S. Sohn (1996). An analytical nonlinear theory of Richtmyer-Meshkov instability. *Phys. Lett. A 212*, 149–155.

Zoltak, J. and D. Drikakis (1998). Hybrid upwind methods for the simmulation of unsteady shock wave diffraction over a cylinder. *Comp. Method. Appl. M. 162*, 165–185.